ABSTRACT

Title of Dissertation: PREPARATION AND CHARACTERIZATION OF TOPOLOGICALLY ORDERED STATE IN NOVEL QUANTUM TECHNOLOGICAL PLATFORMS

Ze-Pei Cian
Doctor of Philosophy, 2022

Dissertation Directed by: Professor Mohammad Hafezi
Department of Physics

With the rapid development of programmable quantum simulators, the quantum states can be controlled with unprecedented precision. Thus, it opens a new opportunity to explore the strongly correlated phase of matter with new quantum technology platforms. In quantum simulators, one can engineer interactions between the microscopic degree of freedom and create exotic phases of matter that presumably are beyond the reach of natural materials. Moreover, quantum states can be directly measured instead of probing physical properties indirectly via optical and electrical responses of material as done in traditional condensed matter. Therefore, it is pressing to develop new approaches to efficiently prepare and characterize desired quantum states in the novel quantum technology platforms.

In this thesis, we discuss the preparation and characterization of the topologically ordered state in nobel quantum technological platforms. First, we show that optically driven monolayer graphene in the quantum Hall regime creates an effective bilayer quantum Hall system. It

provides a flexible platform for engineering quantum Hall phases. We use infinite density matrix renormalization group (iDMRG) techniques combined with exact diagonalization (ED) to show that the system exhibits a non-abelian bilayer Fibonacci phase at filling fraction $\nu = 2/3$. Moreover, at integer filling $\nu = 1$, the system exhibits quantum Hall ferromagnetism. Using Hartree-Fock theory and exact diagonalization, we show that excitations of the quantum Hall ferromagnet are topological textures known as skyrmions.

Then we turn our attention to the characterization of the topological invariants from a ground state wave function of the topological order phase and the implementation in noisy intermediate quantum devices. Using topological field theory and tensor network simulations, we demonstrate how to extract the many-body Chern number (MBCN) given a bulk fractional quantum Hall wave function. We further propose an ancilla-free experimental scheme for measuring the MBCN without requiring any knowledge of the Hamiltonian. Specifically, we use the statistical correlations of randomized measurements to infer the MBCN of a wave function.

Finally, we discuss an unbiased numerical optimization scheme to systematically find the Wilson loop operators given a ground state wave function of a gapped, translationally invariant Hamiltonian on a disk. We then show how these Wilson loop operators can be cut and glued through further optimization to give operators that can create, move, and annihilate anyon excitations. We then use these operators to determine the braiding statistics and topological twists of the anyons, yielding a way to fully characterize topological order from the bulk of a ground state wave function.

PREPARATION AND CHARACTERIZATION OF TOPOLOGICALLY ORDERED STATES IN NOVEL QUANTUM TECHNOLOGICAL PLATFORMS

by

Ze-Pei Cian

Dissertation submitted to the Faculty of the Graduate School of the
University of Maryland, College Park in partial fulfillment
of the requirements for the degree of
Doctor of Philosophy
2022

Advisory Committee:
Professor Mohammad Hafezi, Chair/Advisor
Professor Maissam Barkeshli
Professor Yi-Kai Liu
Professor Norbert Linke
Professor Victor Albert

Acknowledgments

The journey of my Ph.D. study is fulfilling and rewarding. It's my honor to work with so many talented people. I can not imagine finishing this journey without all of your help.

First, I would like to thank my advisor Mohammad Hafezi for his support and guidance in various aspects of my Ph.D. study. I learned a lot from him, not only in physics but also in the way to communicate and brainstorm new ideas. I am always impressed by his enthusiasm and creativity in research. I also appreciate him for giving me the resources and flexibility to collaborate with many scientists and intern in Google Quantum AI.

It is my pleasure to collaborate and discuss with scientists at the Joint Quantum Insitute and other institutes, including Maissam Barkeshli, Liang Jiang, Peter Zoller, Yi-Kai Liu, Victor Albert, Norbert Linke, and Christopher Monroe. I always get insightful comments and learn valuable lessons in discussions with each of you. I also appreciate several fruitful discussions with many graduate students and post-docs in our group: Guanyu Zhu, Tobias Grass, Hossein Dehghani, Wade DeGottardi, Mathias Van Regemortel, Andrey Grankin, Nikko Pomata, Peter Lunts, Yu-An Chen, Alireza Seif, Hwanmum Kim, Chris Flower, Iman Ahmadabadi, Gautam Nambiar, En-Jui Kuo, Yijia Xu.

Moreover, I would like to acknowledge stimulating discussions and collaboration with Andreas Elben, Benoît Vermersch, Su-Kuan Chu, Abolhassan Vaezi, Zhao Liu, Senrui Chen, Sisi Zhou, Daniele De Bernardis, Iacopo Carusotto, Peter Rabl, Eliot Kapit, Daiwei Zhu, Crystal

Noel, Marko Cetina, Yunseong Nam, Ming Li, Qingfeng Wang, and Igor Markov.

In addition, I learn a lot about quantum computation in the industry from working at Google Quantum AI as a student researcher. I am especially indebted to Zhang Jiang for his support and encouragement in my research and career. Moreover, I am privileged to work with many talented scientists at Google. I would like to thank my colleagues for your help and advice, including Jonathan Gross, Dripto Debrpy, Kenny Lee, Benjamin Chiaro and Pedram Roushan.

Finally, I want to thank my parents and wife for their encouragement and support throughout my Ph.D. studies.

Table of Contents

List of Tables

List of Figures

Citation to previously published work

Part of this thesis is based on the published work of the author. Here we list the references that each chapter is based on.

- Chapter 2 :Ze-Pei Cian, Tobias Grass, Abolhassan Vaezi, Zhao Liu, and Mohammad Hafezi. "Engineering quantum Hall phases in a synthetic bilayer graphene system." Physical Review B 102, no. 8 (2020): 085430.

- Chapter 3 : Ze-Pei Cian, Hossein Dehghani, Andreas Elben, Benoît Vermersch, Guanyu Zhu, Maissam Barkeshli, Peter Zoller, and Mohammad Hafezi. "Many-body Chern number from statistical correlations of randomized measurements." Physical Review Letters 126, no. 5 (2021): 050501.

- Chapter 4 : Ze-Pei Cian, Mohammad Hafezi, Maissam Barkeshli. "Extracting Wilson loop operators and fractional statistics from a single ground state on a disk." Manuscript in preparation.

- Appendix A : Hossein Dehghani, Ze-Pei Cian, Mohammad Hafezi, and Maissam Barkeshli. "Extraction of the many-body Chern number from a single wave function." Physical Review B 103, no. 7 (2021): 075102. Harvard

Chapter 1: Introduction

1.1 Topological phases of matter

Topologically ordered phases are gapped quantum phases of matter that cannot be described by the Landau symmetry-breaking paradigm [1, 2]. These states cannot be characterized by local order parameters but rather by long-range entanglement in the ground state wave function and non-local topological invariants such as robust ground state degeneracies on topologically non-trivial spaces. In addition, topological phases can host topologically non-trivial excitations, such as anyons, which can carry fractional quantum numbers and fractional statistics.

In recent years, the interest in engineering topological states of matter in synthetic quantum systems has substantially grown. Examples of such quantum simulators include neutral atoms [3], superconducting qubits [4, 5], photons [6], and more recently Rydberg atoms [7, 8]. With these developments, the benefit of having direct access to the wave function in quantum simulators opens new avenues to investigate and measure the topological properties. In the conventional condensed matter physics the detection of topological properties relies on the application of external probes and linear response framework, and similar schemes have been also proposed for the simulated matter [9, 10, 11, 12, 13]. Moreover, ancilla-based approaches have been proposed that involve a many-body Ramsey interferometry to measure the topological charge [14], and entanglement spectrum [15]. But the fact that the ancilla should be coupled to the entire

system limits the applicability of such schemes. Recently, this question has been theoretically investigated in the context of SPT systems [16, 17, 18, 19, 20, 21], but the problem for topologically-ordered system has been relatively unexplored.

In addition, a fundamental unsolved problem in the study of topologically ordered phases is to understand to what extent the topological invariants characterizing a topological phase of matter are encoded entirely in the ground state wave function, independently of any additional details of the Hamiltonian. In particular, can a complete set of data that fully specifies a topological phase of matter [22, 23, 24, 25, 26] be extracted from a single ground state wave function on a simply connected patch of space?

To date, several invariants of two-dimensional topologically ordered states have been shown to be obtainable from the ground state wave function. In some cases, the ground state, or reduced density matrix, on a disk is sufficient; in other cases, one needs a full set of degenerate ground states on a torus (or infinite cylinder). For example, the total quantum dimension can be measured through the topological entanglement entropy [27, 28]. The modular S and T matrices, which encode details of the fractional statistics of the quasiparticles, can, under certain conditions, be extracted from the full set of ground states on a torus [29, 30, 31] or in the presence of twist defects [32]. In systems with $\mathrm{U}(1)$ symmetry, the many-body Chern number, which determines the fractionally quantized Hall conductance, can be measured by utilizing a SWAP operation between two regions in the bulk of the ground state [33, 34]. In symmetry-protected topological phases (SPTs), which do not have topologically non-trivial quasiparticles, a wide variety of many-body invariants can be obtained from the many-body ground state on a disk or cylinder [19, 20, 21]. The chiral central charge can also be obtained from the reduced density matrix on a disk [35, 36, 37] or, modulo 24, through the momentum polarization of the ground state on a

cylinder [38, 39].

The basic definition of gapped phases of matter suggests that the ground state on a simply connected patch of space should contain enough information to fully characterize the topological phase of matter. More specifically, we say that the ground states of two Hamiltonians H_0 and H_1 are in the same phase if one can find a continuous path in a space of gapped local Hamiltonians H_λ, where $0 \leq \lambda \leq 1$ that connects the two Hamiltonians. With quasi-adiabatic continuation [40], the continuous path can be described by a unitary transformation U, which is generated by a sum of (quasi)-local operators. The unitary transformation can be approximated by a constant depth local quantum circuit. Conversely, a constant depth local quantum circuit allows us to define a continuous path H_λ, since each quantum gate can be expressed by the exponentiation of local interaction terms. Therefore, the question of whether there exists a continuous path that connects the Hamiltonian H_0 and H_1 is equivalent to that of whether one can approximately prepare the ground state of H_1 from the ground state of H_0 with a constant depth quantum circuit [41, 42]. The approximate equivalence between the notion of an adiabatic path in Hamiltonian space and constant depth quantum circuits suggests that the ground state wave function on a disk should contain the complete information characterizing a topological phase of matter.

In this thesis, we investigate the possibility to prepare topologically ordered state in the novel quantum technological platform and propose measurement scheme to probe topological invariants and characterize topological phase of matter from the ground state wave function.

1.2 Many-Body Chern Number

In order to introduce the any-Body Chern Number (MBCN), we first consider a full multiplet of s topologically degenerate ground states on a torus. The wave functions are $\Psi_\alpha(\phi_x, \phi_y)$ defined on a torus geometry, with length L_x and L_y along the x and y directions, respectively. Here $\alpha = 1, \ldots, s$ and we consider abelian quantum Hall states with Hall conductance $\sigma_{xy} = \frac{e^2}{h}\frac{p}{q}$, where p and q are co-prime integers and the parameter $s = q$. In this case, the parameter s is the number of flux quanta that has to be inserted before a topologically trivial excitation is obtained. We note that in general, the parameter s can be different from q when the degenerate ground state subspace is composed of multiple topological sectors.[1].

The twisted boundary conditions are defined as $\hat{t}_j(L_k\hat{k})\Psi(\phi_x, \phi_y) = e^{i\phi_k}\Psi(\phi_x, \phi_y)$, where $k = x, y$ and $\hat{t}_j(\vec{r})$ being the magnetic translation operator of the jth particle along the direction $\vec{r}$. The MBCN of a FQH system is of the form [44]

$$C = \frac{1}{2\pi i}\int_0^{2\pi s} d\phi_x \int_0^{2\pi} d\phi_y \mathcal{F}(\phi_x, \phi_y), \tag{1.1}$$

where $\mathcal{F}(\phi_x, \phi_y) = \langle\partial_{\phi_x}\Psi_\alpha|\partial_{\phi_y}\Psi_\alpha\rangle - \langle\partial_{\phi_y}\Psi_\alpha|\partial_{\phi_x}\Psi_\alpha\rangle$ is the Berry curvature obtained from adiabatically varying the twist angle boundary conditions (ϕ_x,ϕ_y), for a single wave function $|\Psi_\alpha\rangle$.

Alternatively, one can obtain the MBCN, when the wave function is given only as a function of one twist angle. Specifically, let $|\Psi_\alpha(\theta_x)\rangle$ be the ground state wave function in the presence of a flux through the x direction $\oint dx A_x = \theta_x$, and we take the flux in the y direction to be zero,

[1] We define a topological sector to consist of all the degenerate ground states which can be related to each other under the operation of quantized flux insertion in the x and y cycles of a torus [43].

$\oint dy A_y = 0$. We note that for the following argument, one can also consider a cylinder instead of a torus. Following Resta [45], we define the polarization operator as $R_y = \prod_{x,y} e^{i\frac{2\pi y}{\ell_y}\hat{n}(x,y)}$, where the product is taken over the whole system. We then compute

$$\mathcal{T}(\theta_x, s) = \langle \Psi(\theta_x) | R_y^s | \Psi(\theta_x) \rangle. \tag{1.2}$$

Adiabatically changing θ_x is equivalent to applying an electric field E_x, which induces a current in the y direction due to the Hall conductivity, which corresponds to a changing polarization along the $\hat{y}$ direction. The MBCN therefore can be obtained as

$$C = \frac{d}{d\theta_x} \text{arg} \mathcal{T}(\theta_x, s). \tag{1.3}$$

We note that equation above converges to the MBCN in the thermodynamic limit. For systems with finite size, a more robust result can be obtained by averaging over the twist angle: $C = \frac{1}{2\pi} \oint d\theta_x \frac{d}{d\theta_x} \text{arg}\, \mathcal{T}(\theta_x, s)$. The Hall conductivity corresponds to $\sigma_H = \frac{C}{s}\frac{e^2}{h}$.

We note Eq. (1.1) and Eq. (1.2) are equivalent to each other and require toridal and cylindrical geometries, respectively. While there are theoretical proposals to implement such geometries [46, 47], an experimental realization remains challenging.

1.3 Wilson loop operators and anyon data

In this section, we briefly review the basic properties of WLOs and the algebraic theory of anyons. Since our goal is to extract topological invariants from the bulk of the wave function, in this section we consider a two dimensional system on an infinite plane.

The anyon theory consists of a collection of algebraic data that characterize the universal topological properties, namely the fusion and braiding properties, of the anyonic excitations of a many-body system. The precise mathematical framework is that of a unitary modular tensor category (UMTC). For reviews of UMTCs in the context of topological phases of matter, see for example Ref. [22, 48, 49, 50, 51]. For a detailed discussion of how to relate the algebraic data of the UMTC to the microscopic properties of a quantum many-body system, see Ref. [51].

The description that we provide below can be made exact in the context of exactly solvable models, such as the toric code and its generalizations, the quantum double and Levin-Wen models [52, 53]. The effect of perturbations to these exactly solvable models can also be studied systematically, using quasi-adiabatic continuation [40]. For chiral topological phases, such as fractional quantum Hall states or fractional Chern insulators, which have no description in terms of an exactly solvable model, it is expected that the same discussion applies, although it has not been explicitly studied outside of the context of field theory.

1.3.1 Anyons, Wilson line and loop operators

Since the system has a finite correlation length, we can define states with quasiparticle excitations that are localized on the scale of the correlation length. We can then group the quasiparticles into topological equivalence classes: two quasi-particle excitations are equivalent if and only if there is a local operator that can convert one into the other. The different equivalence classes define a finite set of distinct anyon types, sometimes also referred to as superselection sectors or topological charges, $\{I, a, b, c, ...\}$. The set of anyons contains the identity sector I, which corresponds to excitations that can be created by local operators.

Since the anyonic excitations can be localized to within a correlation length of a particular point in space, we can consider a state with anyon type a at position x, and denote it as $|a_x\rangle$. In defining $|a_x\rangle$, we assume that far away from x, on the scale of the correlation length ξ, $|a_x\rangle$ locally looks like the ground state. Furthermore, we assume any other non-trivial topological charges are infinitely far away and do not include them in labeling the state $|a_x\rangle$. Note that since a refers to an equivalence class of excitations, there are many states that can be labeled as $|a_x\rangle$, so our choice is not unique.

By construction, the expectation value of any local observable $O(x')$ satisfies $\langle a_x|O(x')|a_x\rangle = \langle GS|O(x')|GS\rangle$, as long as x and x' are far away from each other, $|x - x'| \gg \xi$, where $|GS\rangle$ is the ground state of the system and ξ is the correlation length. The above equality holds up to $O(e^{-|x-x'|/\xi})$ corrections. Physically, this corresponds to the fact that the state has short-range correlations, so that a disturbance in the vicinity of x has exponentially decreasing effects in the ground state beyond a correlation length.

The anyons can be moved from one place to another by applying an operator along an arbitrary path. In particular, we define a Wilson line operator $W_a(\gamma)$ along a path γ starting at x_1 and ending at x_2. $W_a(\gamma)$ moves the anyon excitation from position x_1 to x_2 along the path γ as shown in Fig. 1.1(a). Such operators are referred to as "movement operators" in [51]. Specifically,

$$|a_{x_2}\rangle = W_a(\gamma)|a_{x_1}\rangle. \tag{1.4}$$

In general, $W_a(\gamma)$ has support, up to exponentially small corrections, on a ribbon of thickness

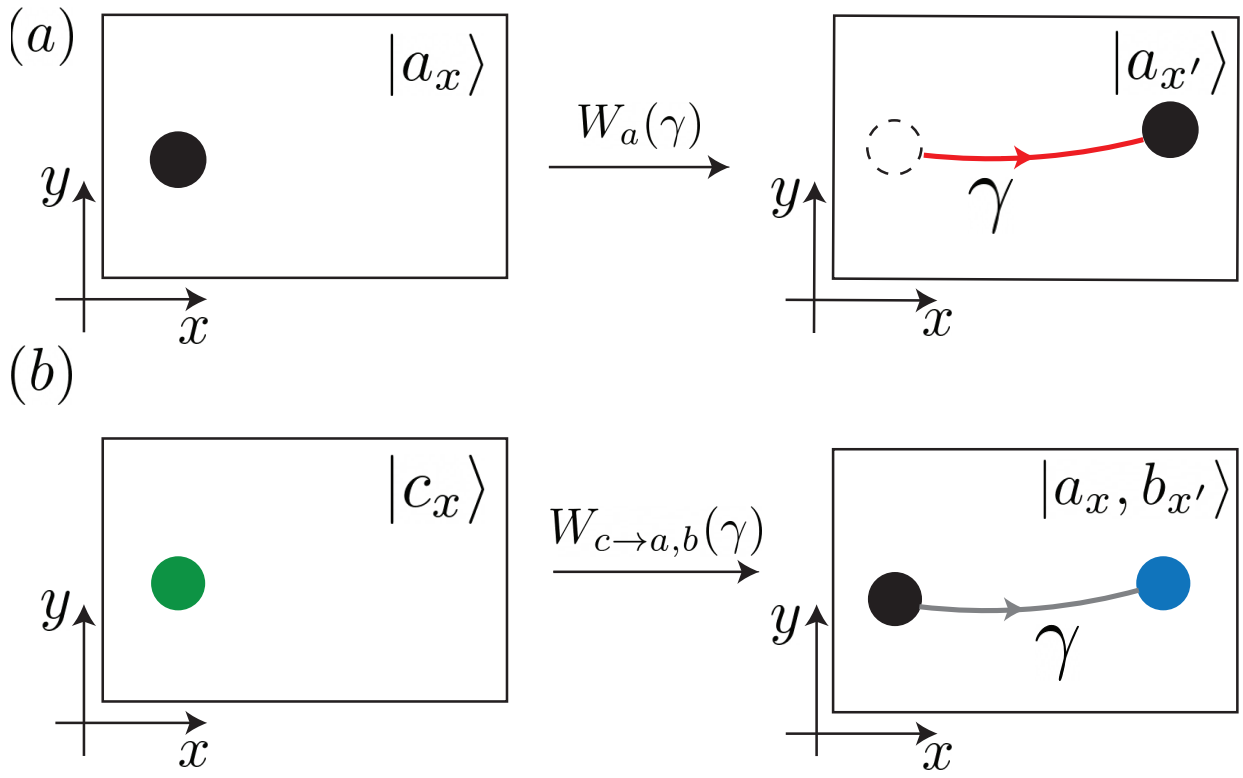

Figure 1.1: (a) When the movement operator $W_a(\gamma)$ is applied to the state $|a_x\rangle$, the anyon excitation is moved to x'. (b) When the splitting operator $W_{c\to a,b}(\gamma)$ is applied to the state $|c_x\rangle$, the anyon splits into two anyons a and b at position x and x', respectively.

on the scale of ξ, centered on γ. [2] The precise choice of the operator $W_a(\gamma)$ is not unique in general, and a precise definition is also non-universal and depends on the microscopic details of the system. Nevertheless, $W_a(\gamma)$ encodes certain universal topological data that we wish to extract.

Note that $W_a(\gamma)$ in general need not be a unitary or even invertible operator, although in many simple examples, particularly when a is an Abelian anyon, $W_a(\gamma)$ can be chosen to be

[2] Specifically, $W_a(\gamma)$ can be approximated by a ribbon operator with finite thickness t [40]. The error of the approximate Wilson line operator W is of order $\epsilon = |\langle\psi|W - W_{\text{exact}}|\psi\rangle| \sim O(N_s e^{-t/\xi})$, where N_s is the number of sites in the support of W, and W_{exact} is the exact, and presumably non-local WLO, for the ground state wave function $|\psi\rangle$.

unitary. Moreover, when a is Abelian, we can take

$$W_a^\dagger(\gamma) = W_{\bar{a}}(\gamma) = W_a(-\gamma), \tag{1.5}$$

where $-\gamma$ refers to the path γ traversed in the opposite direction and $\bar{a}$ is the anti-particle of a. That is, $W_a^\dagger(\gamma)$ effectively takes $\bar{a}$ along γ or, equivalently, takes a along the path $-\gamma$.

We can also define loop operators by picking γ in $W_a(\gamma)$ to be a closed loop. Physically this can be understood as creating a and its dual $\bar{a}$ out of the ground state, moving one around the loop γ, and reannihilating. If γ is a contractible loop in the space, such operators should keep the ground state invariant. Therefore, for each loop γ we have a loop operator $W_a(\gamma)$, which keeps the ground state invariant:

$$W_a(\gamma)|GS\rangle = d_a|GS\rangle. \tag{1.6}$$

Here $d_a \geq 1$ is referred to as the quantum dimension of the anyon a, and is part of the universal data of the UMTC. We have chosen a convention where $d_a \geq 1$ appears on the RHS; we could in principle absorb d_a into the definition of $W_a(\gamma)$. The choice above allows us to make contact with the fusion algebra of the UMTC description.

As with the line operators, the Wilson loop operators $W_a(\gamma)$ are in general not unitary operators, unless a is an Abelian anyon, in which case we also have $d_a = 1$.

Eq. 1.6 makes explicit that the ground state of a topologically ordered state has emergent symmetries, as there are loop operators that keep the ground state invariant. Importantly, the operators are supported, up to exponentially small corrections, on a codimension-1 region, and

therefore do not correspond to ordinary global symmetries, which have support over the entire space. When the anyons are Abelian, the Wilson loop operators form a group structure and are referred to as 1-form symmetries [54]; more generally they are referred to as categorical or non-invertible symmetries.

1.3.2 Fusion rules and splitting operators

The anyons define a fusion algebra

$$a \times b = \sum_c N_{ab}^c c, \tag{1.7}$$

where the fusion multiplicities N_{ab}^c are non-negative integers, which indicate the number of different ways the anyons a and b can be fused to produce the anyon type c. Each anyon type a has a unique anti-particle $\bar{a}$, where $\bar{a} \in \mathcal{C}$ is such that $N_{a\bar{a}}^I \neq 0$. Note that we can define a fusion matrix N_a, with entries $(N_a)_{bc} = N_{ab}^c$; the quantum dimension d_a is then the largest eigenvalue of N_a.

An anyon a is Abelian if and only if it gives a unique fusion outcome upon fusing with another anyon b. That is, given b, $N_{ab}^c = 1$ for a unique c and $N_{ab}^c = 0$ otherwise.

The fusion rule leads to the following relation for the Wilson loop operator:

$$W_a(\gamma)W_b(\gamma)|GS\rangle = \sum_c N_{ab}^c W_c(\gamma)|GS\rangle, \tag{1.8}$$

whenever γ is a loop. Note that with the conventions chosen above, this implies $d_a d_b = \sum_c N_{ab}^c d_c$.

In addition to movement operators and loop operators, we can define splitting operators.

For simplicity, here we only introduce the spliting operator in the case $N_{ab}^c \leq 1$; the generalization can be found in Ref. [51]. Suppose that c is contained in the fusion outcome of a and b, that is, $N_{ab}^c = 1$. We can define a splitting operator,

$$W_{c\to a,b}(\gamma)|c_{x_1}\rangle = |a_{x1}, b_{x_2}\rangle, \tag{1.9}$$

where $|a_{x1}, b_{x_2}\rangle$ denotes a state with two excitations: anyon a at position x_2 and anyon b at position x_1 and $|x_2 - x_1| \gg \xi$ as shown in Fig. 1.1(b).

One can also create the anyon a and its antiparticle $\bar{a}$ by applying

$$W_{I\to\bar{a},a}(\gamma)|I_{x_1}\rangle = |\bar{a}_{x_1}, a_{x_2}\rangle, \tag{1.10}$$

where $|I\rangle$ is a state in the identity superselection sector.

Observe that if we start with a loop operator $W_a(\gamma)$, and we project part of the operator along some segment of γ to the identity, then we obtain a cut operator that effective creates an anyon and its anti-particle out of the vacuum. Therefore we can obtain a choice of $W_{I\to a,\bar{a}}(\gamma_{\text{cut}})$ by starting with $W_a(\gamma)$ for a loop γ and implementing the above cutting procedure.

1.3.3 Modular S matrix and twist product

A large portion of the universal data of a topological phase of matter is encoded in the modular S and T matrices. In fact for almost all topological phases of interest in physics, the S and T matrices provide a complete set of invariants.

The modular S matrix contains information about the mutual braiding statistics between

far separated anyon excitations, and also completely defines the fusion coefficients N_{ab}^c.

In particular, S_{ab} is the quantum mechanical amplitude of the process where a particle of type a and another particle of type b are created and separated, the particle a is moved around the particle b, and then the particle-anti-particle pairs are annihilated.

Given a set of closed Wilson loop operators W_a, where $a \in \mathcal{C}$, we can define a matrix $\tilde{S}_{ab}$, as

$$\tilde{S}_{a,b} = \frac{\langle GS|W_a \infty W_b|GS\rangle}{\langle GS|W_a W_b|GS\rangle}, \tag{1.11}$$

where ∞ is the twist product (see e.g. Ref. [55]) and shown in Fig. 1.2. For arbitrary WLOs P and Q defined in regions A and B as shown in Fig. 1.2(a), $P = \sum_k P_k^A \otimes P_k^B$, $Q = \sum_l Q_l^A \otimes Q_l^B$, the twist product $P \infty Q$ is defined as

$$P \infty Q = \sum_{kl} P_k^A Q_l^A \otimes Q_l^B P_k^B, \tag{1.12}$$

where the product order is reversed in the region B.

Note that to define the above twist product, we need each operator W_a to have support strictly on a ribbon of finite thickness.

We expect that $\tilde{S}_{ab}$ is related to S_{ab} as

$$\tilde{S}_{ab} = \frac{d_a d_b}{\mathcal{D}} S_{ab}, \tag{1.13}$$

where $\mathcal{D} = \sqrt{\sum_a d_a^2}$ is the total quantum dimension. In this paper we only work with Abelian anyons, in which case $d_a = 1$ and $\mathcal{D}^2$ is the total number of distinct anyon types.

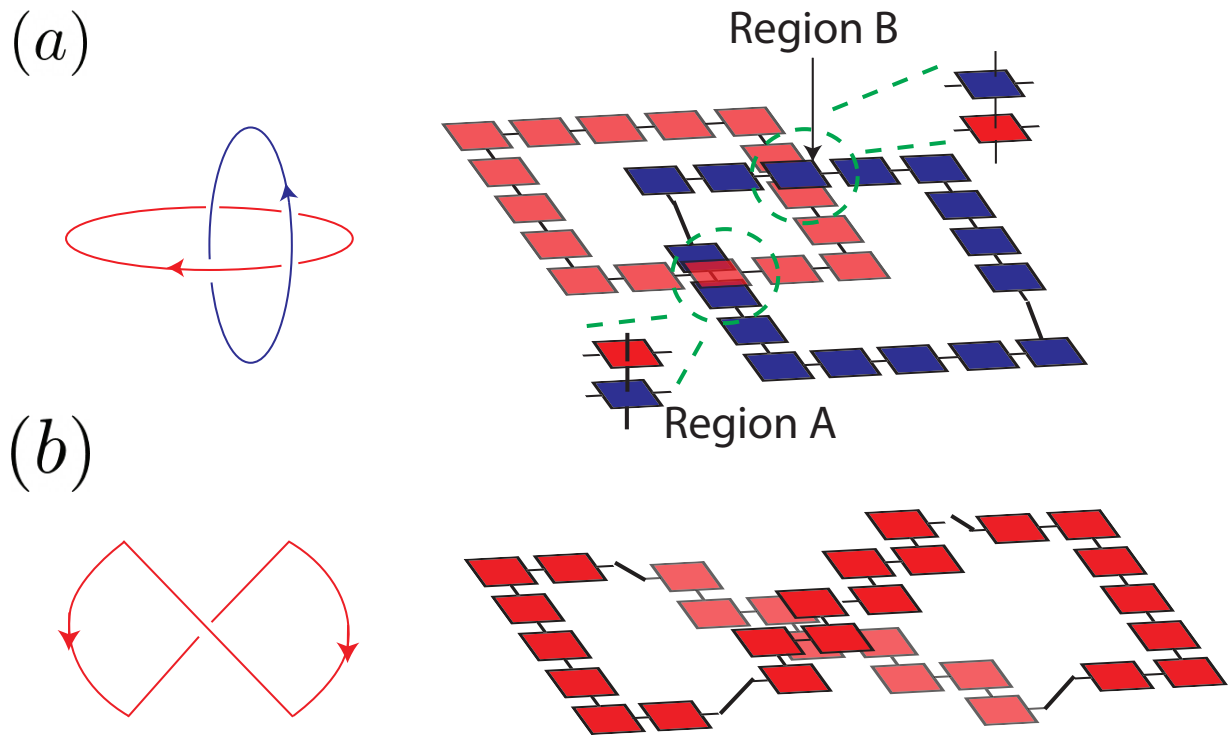

Figure 1.2: (a) **Mutual-braiding statistics.** To measure the mutual braiding statistics, we calculate twist product for two Wilson loop operators W_a and W_b. The supports of the two Wilson loop operators are divided into two regions. In region A, the order of the product is W_aW_b and in the region B, the order of the product is reversed. (b) The matrix product operator that measures the self-braiding statistic T_a.

For Abelian anyons, the braiding phase between anyon i and j can be measured from the phase of the twist product

$$\phi_{i,j} = \arg[\tilde{S}_{i,j}]. \tag{1.14}$$

1.3.4 Modular T matrix

The modular T-matrix is a diagonal matrix,

$$T_{ab} = \theta_a \delta_{ab} \tag{1.15}$$

where θ_a is the topological twist of the anyon a. Due to the spin-statistics theorem, θ_a also corresponds to the exchange statistics of a. In order to exchange a pair of identical anyons, we first create two anyon and anti-anyon pairs from the ground state, and we then move the two identical anyons and exchange them. Finally we fuse the anyon and anti-anyon and return the the ground state as shown in Fig. 1.2(b). If we normalize the process properly, the net effect of this procedure gives the exchange statistics of the anyons.

One can create and exchange anyons and measure the exchange statistics using the Wilson loop operators. The detailed implementation of the extraction of exchange statistics using the Wilson loop operators is given in Sec. 4.3.5.

1.4 Outline of thesis

The rest of this thesis is organized follows:

- In Chapter 2 we show that Synthetic quantum Hall bilayer (SQHB), realized by optically driven monolayer graphene in the quantum Hall regime, provides a flexible platform for engineering quantum Hall phases. The coherent driving which couples two Landau levels mimicks an effective tunneling between synthetic layers. The tunneling strength, the effective Zeeman coupling, and two-body interaction matrix elements are tunable by varying the driving frequency and the driving strength. Using infinite density matrix renormalization

group (iDMRG) techniques combined with exact diagonalization (ED), we show that the system exhibits a non-abelian bilayer Fibonacci phase at filling fraction $\nu = 2/3$. Moreover, at integer filling $\nu = 1$, the SQHB exhibits quantum Hall ferromagnetism. Using Hartree-Fock theory and exact diagonalization, we show that excitations of the quantum Hall ferromagnet are topological textures known as skyrmions.

- In Chapter 3 we propose an ancilla-free experimental scheme for the measurement of this invariant, without requiring any knowledge of the Hamiltonian. Specifically, we use the statistical correlations of randomized measurements to infer the many-body Chern number of a wavefunction. Remarkably, our results apply to disk-like geometries that are more amenable to current quantum simulator architectures.

- In Chapter 4 we present and implement an unbiased numerical optimization scheme to systematically find the Wilson loop operators given a single ground state wave function of a gapped, translationally invariant Hamiltonian on a disk. We then show how these Wilson loop operators can be cut and glued through further optimization to give operators that can create, move, and annihilate anyon excitations. We subsequently use these operators to determine the braiding statistics and topological twists of the anyons, yielding a way to fully extract topological order from a single wave function. We apply our method to the ground state of the perturbed toric code and doubled semion models with a Zeeman field that is up to a third of the critical value. From a contemporary perspective, this can be thought of as a machine learning approach to discover emergent 1-form symmetries of a ground state wave function.

Chapter 2: Engineering quantum Hall phases in a synthetic bilayer graphene system

2.1 Introduction

Fractional quantum Hall (FQH) phases are paradigm examples of topological order, providing the rich physics associated with anyonic statistics[56, 57]. Moreover, non-Abelian anyon statistics [58, 59, 60, 61, 62] have been shown to be a powerful resource for performing topological quantum computation [63, 64, 65]. Currently, there is intense interest in the realization of FQH states in the multicomponent systems [66, 67, 68, 69]. In contrast to the single-component system, the multicomponent FQH system with extra degree of freedom enables wider tunablity and exhibits a richer quantum phase diagram. Several non-abelian FQH phases have been proposed for bilayer FQH systems, including the Moore-Read state at filling $\nu = 1/2$ [70], interlayer and intralayer Pfaffian states at filling $\nu = 2/3$ [71, 72], and bilayer Fibonacci state at filling $\nu = 2/3$ [73, 74].

In addition to these topological order states, the multicomponent quantum Hall system may also exhibit synthetic quantum Hall ferromagnetism. In such ferromagnet, all electrons spontaneously align their (iso)spin in order to minimize the Coulomb exchange interaction, while their kinetic energy is quenched into highly degenerate Landau levels (LLs). Adding an additional

particle to the ferromagnet triggers a skyrmion excitation, which is characterized by a winding of the magnetization. Skyrmion excitations have been the subject of many theoretical [75, 76, 77, 78] and experimental studies [79, 80, 81].

It has been shown that the monolayer graphene coupled to a light field enables flexible control on the quantum level [82, 83, 84]. For example, optical driving can be used to induce topologically non-trivial band structure through Floquet mechanism [84, 85]. So far, Floquet topological insulators have mainly been studied from the perspective of single-particle physics, but more recently, it has also been proposed to modify effective interaction terms via optical driving [83]. This paves the way to the optical engineering of FQH phases. Specifically, when a classical light field couples to two LLs near resonance, the optical transitions between the two Landau levels mimick an effective tunneling between two synthetic "layers", so the system can be interpreted as a synthetic quantum Hall bilayer (SQHB). In contrast to real bilayers, the tunneling strength in the SQHB is freely tunable via the laser intensity. The detuning of the coupling can be used to adjust the chemical potential of the two synthetic layers.

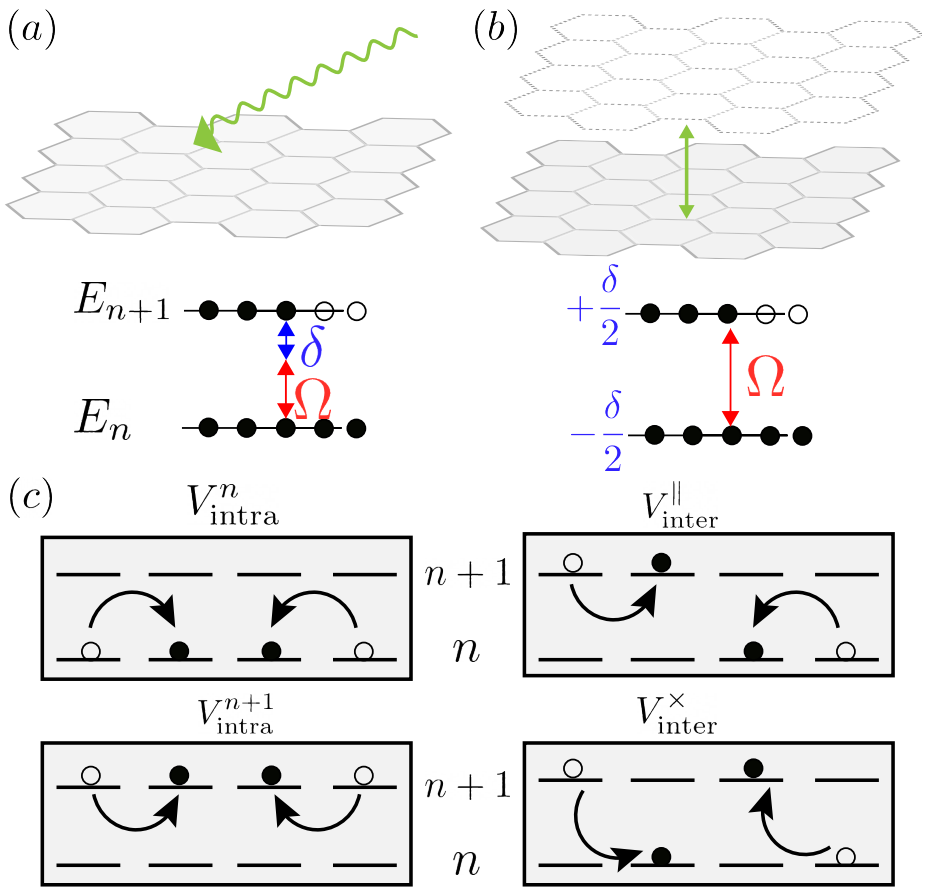

Figure 2.1: Illustration of the SQHB system. (a) A monolayer graphene in the quantum Hall regime is driven by light with Rabi frequency Ω and detunning δ. (b) In the rotating frame, the system effectively becomes a quantum Hall bilayer. The tunneling strength is given by the Rabi frequency and the energy difference between the two layers is determined by the laser detunning δ. (c) The effective Coulomb interaction in the SQHB picture: V^n_{intra} and V^{n+1}_{intra} are the intra-layer interaction that scatter electrons in the same layer. $V^{\parallel}_{\text{inter}}$ is the inter-layer interaction that preserve the layer index. The interaction $V^{\times}_{\text{inter}}$ exchanges the layer index of the two electrons during the scattering process. Such a process is absent in the usual quantum Hall bilayer.

One particularly intriguing case is when the first LL (LL_1) and the second LL (LL_2) are coupled ($LL_1 - LL_2$). Then, the repulsion between singlet pairs becomes small. To some extent, these interactions resemble a hollow-core model, that is, an interaction model based on Haldane pseudopotentials V_m [86], in which $V_1 \neq 0$, but $V_0 = 0$. Generally, such interactions favor the formation of many-body singlet states, and at filling fraction $\nu = 2/3$, the ground state of

the hollow-core Hamiltonian has been reported to be a non-abelian phase. Both the interlayer Pfaffian phase [72], and the bilayer Fibonacci phase [71] have been discussed in this context, but the topological phase of the SQHB at $\nu = 2/3$ has remained unclear in the previous study, mainly due to the limitation of small system size accessible to the exact diagonalization (ED). Here, by using the infinite density matrix renormaliztion group (iDMRG)[87, 88, 89] along with ED, we identify the non-Abelian phase of the $LL_1 - LL_2$ synthetic bilayer system to be the bilayer Fibonacci phase. With this, the SQHB becomes an interesting environment for topological quantum computing.

The striking FQH behavior of the $LL_1 - LL_2$ SQHB is a consequence of the peculiar shape of its pseudopotentials. The behavior is very observed in a system where LL_0 and LL_1 are coupled. As we show in this paper, the qualitative change of interactions in $LL_0 - LL_1$ or $LL_1 - LL2$ bilayers can also be observed at integer filling $\nu = 1$, although interactions typically play a much smaller role in the integer quantum Hall regime. Specifically, we show that the $LL_0 - LL_1$ bilayer exhibits synthetic quantum Hall ferromagnetism at $\nu = 1$, whereas the $LL_1 - LL_2$ bilayer does not, due to its tendency towards singlet formation.

The synthetic ferromagnetic behavior can also be controlled by the laser detuning: it acts as an effective Zeeman term which lifts the (iso)spin degeneracy and competing with the ferromagnetic exchange energy whose scale is given by the strength of the Coulomb interaction. When the ferromagnetic exchange interaction dominates over the Zeeman energy, the addition of one particle leads to a spin flip of many particles in order to keep neighboring spins almost aligned with each other. This collective spin flip leads to a winding texture, which is known as a skyrmion. Using Hartree-Fock mean-field theory and exact diagonalization, we show that the $LL_0 - LL_1$ SQHB system exhibits such skyrmion excitations, whereas the $LL_1 - LL_2$ system

does not.

The chapter is organized as follows: In Sec. 2.2, we review the formalism of the graphene quantum Hall state and the SQHB. In Sec. 2.3, we provide the detail numerical evidence showing that the SQHB with filling fraction $\nu = 2/3$ is a bilayer Fibonacci phase. In Sec. 2.4, the isospin texture excitation in the quantum Hall ferromagnetic regime is discussed. Finally, in Sec. 2.5, we summarize our results.

2.2 Synthetic Bilayer Graphene System

In this section, we describe the SQHB system, that is, a single-layer quantum Hall system in which a synthetic bilayer degree of freedom is induced by a laser coupling between Landau levels. Such a system can be realized in monolayer graphene under a strong magnetic field [90]. We assume that both the electronic spin and valley degrees of freedom are fully polarized. In the quantum Hall regime, the single-particle eigenstates in graphene are given by spinors of the form

$$\psi_{\sigma,n,m} = \begin{bmatrix} C_n^- n-1, m \\ C_n^+ \sigma n, m \end{bmatrix}, \tag{2.1}$$

where $C_n^{\pm} = \sqrt{\frac{1\pm\delta_{0,n}}{2}}$. The quantum number $\lambda = \pm 1$ labels the states of positive and negative energy, respectively. The kets n, m denote the eigenstates of a non-relativistic quantum Hall system, with $\langle \mathbf{r}|n, m\rangle$ being the Landau level (LL) wave function of the nth LL with orbital quantum number m. In the symmetric gauge, the orbital quantum number m denotes the angular momentum. In the Landau gauge, it represents the momentum which is conserved along one

spatial direction. The single-particle energy of the state $\psi_{\sigma,n,m}$ is given by

$$E_\sigma = \sigma \frac{\hbar v_F}{l_B} \sqrt{2n}, \tag{2.2}$$

where $l_B = \sqrt{\hbar/eB}$ is the magnetic length, B is the magnetic field strength and v_F is the Fermi velocity. In the following, we only consider the positive energy part and, therefore, drop the subscript σ for simplicity.

Unlike the non-relativistic LL spectrum, the relativistic energy spectrum is not quantized at equally spaced values in the graphene quantum Hall system. We can thus selectively couple two distinct LLs via a mono-chromatic laser with frequency ω_L, according to the usual selection rule $|n| \leftrightarrow |n \pm 1|$. These two laser-coupled LLs represent the two "layers" of our synthetic bilayer quantum Hall system.

In the following, we consider a coupling between a (partially) filled LL and an empty $(n+1)$th LL. We assume that the driving laser is a plane wave such that the coupling is non-vanishing only between states with the same orbital quantum number m. Other selection rules are possible if the light is designed to have orbital angular momentum [82, 91]. Under the rotating wave approximation (RWA), the Hamiltonian of the synthetic bilayer system is given by [83]

$$\begin{aligned} H &= H_0 + H_{int}, \\ H_0 &= \sum_m \left(-\delta \tau^z_{n,m} + \Omega \tau^x_{n,m} \right), \\ H_{int} &= \sum_{n_1+n_2=n_3+n_4} \sum_{\{m\}} V^{n_1,n_2,n_3,n_4}_{m_1,m_2,m_3,m_4} c^\dagger_{n_1,m_1} c^\dagger_{n_2,m_2} c_{n_3,m_3} c_{n_4,m_4}, \end{aligned} \tag{2.3}$$

where $c_{n,m}$ and $c^{n,m}$ are the annihilation and creation operators in the nth Landau level with

angular momentum quantum number m, $\delta = E_{n+1} - E_n - \omega_L$ is the detuning, and Ω is the Rabi frequency. The isospin operators are given by $\tau^z_{n,m} = c^{n,m}c_{n,m} - c^{n+1,m}c_{n+1,m}$ and $\tau^x_{n,m} = c^{n,m}c_{n+1,m} + c^{n+1,m}c_{n,m}$. The first term in H_0 corresponds to an effective Zeeman coupling for the quantum Hall system with spin degree of freedom and the second term corresponds to the tunneling in the bilayer quantum Hall system. The interaction matrix elements $V^{n_1,n_2,n_3,n_4}_{m_1,m_2,m_3,m_4}$ are for Coulomb scattering of a pair of electrons in Landau orbitals $\{n_1, m_1\}$ and $\{n_2, m_2\}$ to orbitals $\{n_3, m_3\}$ and $\{n_4, m_4\}$, but the sum over n_i is restricted to $n_1 + n_2 = n_3 + n_4$ by the RWA.

In a conventional bilayer system, the spatial overlap between single-particle states in different layers is negligible, and thus, Coulomb terms which would scatter an electron from one layer into the other do not play a role. With this, the layer index of each particle is conserved in the scattering term. For the synthetic bilayer, however, the situation is different, as two particles can exchange their individual indices. This leads to the four different types of scattering process which are shown in 2.1(c): The intra-layer interaction in the nth LL and $(n+1)$th LL are $V^n_{\text{intra}} = \sum_{\{m\}} V^{n,n,n,n}_{m_1,m_2,m_3,m_4} c^\dagger_{n,m_1} c^\dagger_{n,m_2} c_{n,m_3} c_{n,m_4}$, and V^{n+1}_{intra} respectively. For a pair of electrons in different layers, there are two types of inter-layer interactions: the standard process which keeps the electrons in their layer is denoted by $V^{\parallel}_{\text{inter}} = 2\sum_{\{m\}} V^{n,n+1,n+1,n}_{m_1,m_2,m_3,m_4} c^\dagger_{n,m_1} c^\dagger_{n+1,m_2} c_{n+1,m_3} c_{n,m_4}$. In addition to this, the SQHB allows for an exchange interaction in which the layer index is changed, i.e. $V^{\times}_{\text{inter}} = 2\sum_{\{m\}} V^{n,n+1,n,n+1}_{m_1,m_2,m_3,m_4} c^\dagger_{n,m_1} c^\dagger_{n+1,m_2} c_{n,m_3} c_{n+1,m_4}$.

We may expand these different scattering potentials in terms of Haldane pseudopotentials, $V^n_m, V^{n+1}_m, V^{\parallel}_m, V^{\times}_m$. As shown in Ref. [83], the scattering of interlayer singlets is described by the pseudopotentials $V^{\parallel}_m - V^{\times}_m$, whereas the scattering of interlayer triplets is given by $V^{\parallel}_m + V^{\times}_m$. Noting that a symmetric (antisymmetric) layer configuration has to be combined with an antisymmetric (symmetric) spatial wave function, the interlayer scattering at even (odd) values

of m is given by the pseudopotentials for interlayer singlets (triplets):

$$V_m^{\text{inter}} = \begin{cases} V_m^{\parallel} + V_m^{\times} & \text{if } m \text{ is odd,} \\ V_m^{\parallel} - V_m^{\times} & \text{if } m \text{ is even.} \end{cases} \tag{2.4}$$

The form of the interlayer potential highlights the role which is played by the exchange interaction $V_m^{\times}$: While suppressing the scattering at $m = 0$, it enhances interactions at $m = 1$. As shown in Ref. [83], the strength of this effect depends crucially on the Landau levels which are coupled: When the zeroth and the first Landau levels are coupled ($LL_0 - LL_1$), the effect of the exchange interaction is only quantitative (in the sense that V_0^{inter} remains the strongest interlayer interaction channel). In contrast, when the first and the second Landau level are coupled ($LL_1 - LL_2$), a qualitative change of V_m^{inter} is seen. In this case, $V_1^{\text{inter}} > V_0^{\text{inter}}$, that is, the first Haldane pseudopotential dominates the interlayer interaction. Therefore, the synthetic bilayer with $LL_1 - LL_2$ coupling has a strong tendency to form spin singlet phases.

2.3 Bilayer Fibonacci phase

A huge variety of spin singlet phases have been discussed for bilayers at filling fraction $\nu = \frac{2}{3}$. These phases include Abelian composite fermion and Halperin phases, and also non-Abelian phases such as bilayer Fibonacci state and interlayer-Pfaffian state [71, 72, 73, 74]. Strikingly, in the SQHB non-zero overlaps have been reported for these non-abelian phases, but a clear identification of the phase has remained a challenge. Below, we provide a variety of numerical evidences which demonstrate that the SQHB exhibits the bilayer Fibonacci phase. Specifically, we compute various characteristics of topological phases, including entanglement

spectra, entanglement entropy, ground state degeneracies, using the large scale infinite density matrix renormalization group (iDMRG) algorithm on infinite cylinder geometry, as well as ED in a spherical geometry.

Before presenting the numerical evidences for the Fibonacci phase, let us briefly discuss the role played by the parameters in the single-particle Hamiltonian. The single-particle orbitals are superpositions of the two synthetic layers, and for $\Omega \gg \delta$, the orbitals are simply the symmetric and anti-symmetric combinations. The energy splitting between the two states are of the order of 2Ω, with the anti-symmetric orbits being the lower manifold. If this single-particle gap becomes large as compared to the interaction energy, i.e. $\Omega \gg \frac{e^2}{2\epsilon l_B}$, we can treat the system as a single layer quantum Hall system. In this case, the ground state at $\nu = 2/3$ is the hole-conjugate of the $\nu = \frac{1}{3}$ Laughlin state. The system undergoes a phase transition as the Rabi frequency Ω is decreased. In the weak coupling regime, the ground state forms a layer singlet state [83], which is identified as the Fibonacci phase below.

For the bilayer Fibonacci phase, there are six topologically distinct types of quasi-particles. Three of them are abelian quasi-particle denoted by Φ_n, where $n = 0, 1, 2$. The abelian quasi-particles follow the fusion rule $\Phi_a \times \Phi_b = \Phi_{(a+b)\%3}$. The Φ_0 sector corresponds to the vacuum sector $\mathcal{I}$ since it satisfies $\Phi_0 \times \Phi_n = \Phi_n$. On the other hand, there is a "Fibonacci" quasi-particle τ which satisfies the fusion rule $\tau \times \tau = 1 + \tau$. The braiding statistics of the Fibonacci anyon allows for universal topological quantum computation. The rest of two quasi-particles are can be described by $\Phi_a\tau$ with $a = 1, 2$ [73, 74].

The evidences for characterizing the bilayer Fibonacci phase are the following: (1) We perform the adiabatic continuation (AC) to show that the ground state on the sphere is in the same class as the bilayer Fibonacci phase. (2) We obtain two topologically distinct degenerate

ground states ψ_1 and ψ_2 on a infinite cylinder. Combined with the center-of-mass translation, this leads to a six-fold ground state degeneracy. (3) The counting of edge states is done within the orbital entanglement spectrum obtained from these two ground states, and it matches the counting expected for the bilayer Fibonacci phase. (4) By calculating the difference of the entanglement entropy and the momentum polarization between the two ground states ψ_1 and ψ_2, we obtain the topological entanglement entropy and the topological spin of the non-abelian anyon. Their values are consistent with the bilayer Fibonacci phase.

2.3.1 Adiabatic Continuation on the Spherical Geometry

The finite size limitation of the ED calculation make it challenging to extract useful topological information. However, since topological phase transitions require the closing of the energy gap, it is possible to test the topological behavior by adiabatically deforming the system Hamiltonian into a simpler model Hamiltonian for which the topological phase is known. We adiabatically change the electron interaction by interpolating between the Coulomb interaction of the synthetic graphene bilayer and a hollow-core model, that is, an interaction Hamiltonian with the interlayer pseudopotential V_1^{inter} being the only-non-zero pseudopotential. Such a model has been shown to support the bilayer Fibonacci phase [74]. The Hamiltonian which interpolates between Coulomb interaction and hollow-core model is given by

$$H_\lambda = (1-\lambda)H_{int} + \lambda \hat{V}_1^{\text{inter}}, \tag{2.5}$$

where $0 \leq \lambda \leq 1$. H_{int} is the Coulomb interaction of the synthetic bilayer graphene system, and $\hat{V}_1^{\text{inter}}$ is the interaction term generated by a interlayer Haldane pseudo-potential model with

$V_m^{\text{inter}} = \delta_{m,1}$. If the ground state of the synthetic bilayer graphene and the $\hat{V}_1^{\text{inter}}$ interaction are in the same universality class, the ground state wave function and the ground state energy should change smoothly when the parameter λ in the Hamiltonian in Eq. (2.5) varies adiabatically, and the gap above the ground state should not close.

To access the energy spectrum of the Hamiltonian in Eq. (2.5), the ED calculation is performed in the spherical geometry. The number of electrons N_e and total number of quantum fluxes N_ϕ are related by $N_\phi = \frac{1}{\nu}N_e - S$, where S is the shift of fractional QH state on sphere. For the bilayer Fibonacci phase, the shift $S = 3$. We start with infinitesimal Rabi frequency Ω and zero detuning δ and therefore occupation of each synthetic layer is conserved. Thus, we can to examine the entanglement spectrum with a fixed total layer polarization (or total pseudospin). The stability upon increasing the Rabi frequency Ω to a finite value in the weak coupling regime is shown in the fig. 2.2(b). The energy gap remains open under small perturbation of Ω.

The energy spectrum of the adiabatic continuation with $N_e = 12$ is shown in Fig. 2.2(a). The energy gap remains open in the process of the adiabatic continuation. This suggests that the ground state of the synthetic bilayer graphene is in the phase defined by $\hat{V}_1^{\text{inter}}$, i.e. the bilayer Fibonacci phase.

Fig. 2.2(c) and (d) show the orbital cut entanglement spectrum (OES) for zero and non-zero value of λ. The low energy part of the ES corresponds to the degeneracy of the edge excitation with angular momentum L_z relative to the ground state [92]. The counting of the edge excitation allows us to determine the topological order of a wave function. However, finite-size effects close the entanglement gap in most angular momentum sectors, which makes the correct counting difficult. However, we are able to verify that the counting for the SQHB [see panel Fig.2.2(c)] is compatible with the counting 1,1,3,6 which is characteristic for the Fibonacci phase, and which

we obtain when λ is chosen to be close to 1 [see panel Fig.2.2(d)].

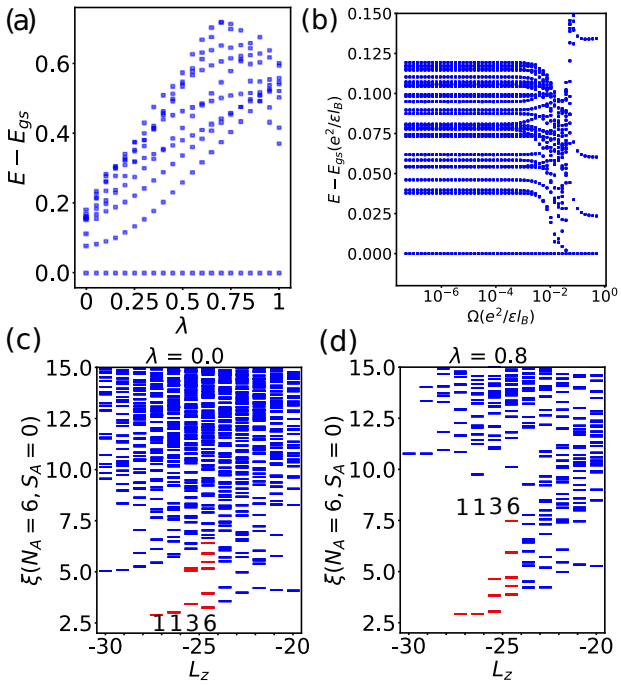

Figure 2.2: Adiabatic continuation via exact diagonalization (a) Energy spectrum in the process of adiabatic continuation for $N_e = 12$, $N_\phi = 15$. The energy gap remains open during the adiabatic continuation process. This indicates that the ground state wavefunction and bilayer Fibonacci phase are in the same class. (b) Energy spectrum for $N_e = 8$, $N_\phi = 10$ and $\lambda = 0$ as function of the Rabi frequency Ω. The system undergoes a phase transition to the particle-hole conjugate of Laughlin state when $\Omega \gg 1$. (c) and (d) show the orbital cut entanglement spectrum for $N_e = 12$, $N_\phi = 15$,with $\lambda = 0$ and $\lambda = 0.8$ respectively.

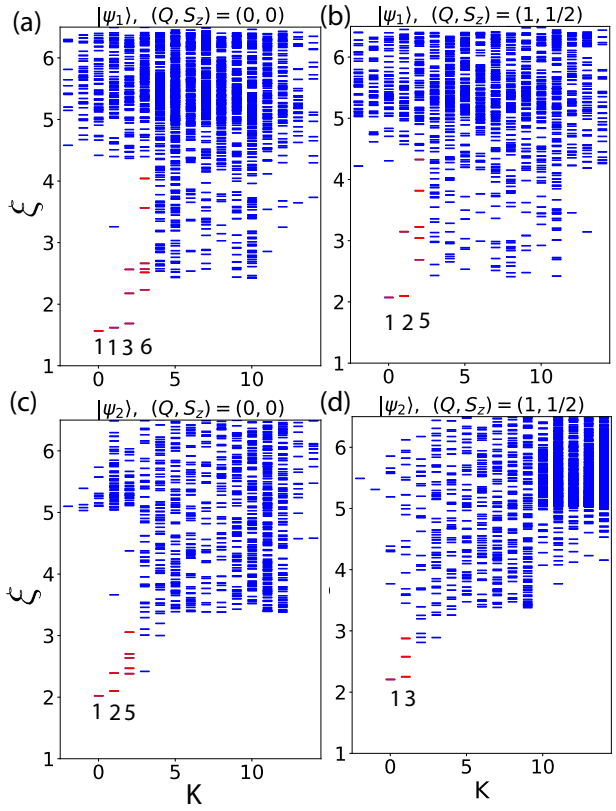

Figure 2.3: Orbital entanglement spectra for the two degenerate ground states at circumference $L = 30l_B$. The maximum bond dimension $\chi_{max} = 15000$. Two distinct orbital cuts are presented for each ground state. The low-lying spectra agree with the CFT prediction as described in the main text.

2.3.2 Ground State Degeneracy and Entanglement Spectrum

On topological non-trivial geometries, such as the torus, non-Abelian phases exhibit characteristic ground state degeneracies. The same degeneracies as for the torus can also be observed for infinite cylinders, for which we have computed the ground states via infinite DMRG (iDMRG) [88].

We perform the iDMRG simulation and obtain two orthogonal states ψ_1 and ψ_2. The two wave functions are nearly degenerate. Along with the center-of-mass translation, we have an (at least) six-fold degenerate ground state on the infinite cylinder. It should be noted, though, that this is as a lower bound on the degeneracy, since there is no systematic way to guarantee that

iDMRG finds all degenerate ground states. In order to further confirm our result, we initialize the infinite MPS ansatz with different configuration for perimeter of the infinite cylinder $4l_B \leq L \leq 10l_B$. After a few DMRG sweeps with moderate bond dimention (around 450), the wave function always converges to two orthogonal states.

In the following section, we examine the topological properties of the two wave functions by calculating the orbital entanglement spectrum (OES), topological entanglement entropy (TEE), and the topological spin. In order to resolve the entanglement spectrum in different total spin sector, we assume that the Rabi frequency Ω is infinitesimal and, therefore, the total pseudo-spin $S_z = N_\uparrow - N_\downarrow$ is a good quantum number, where $N_\uparrow$ and $N_\downarrow$ denote the number of electrons in the nth and $(n+1)th$ LLs, respectively. Fig. 2.3 shows the entanglement spectrum of the ground state ψ_1 and ψ_2. The level counting of the OES can be obtained using the thin torus patterns and generalized exclusion rules [74]. For the ground state ψ_1, the counting is $1, 1, 3$ when the partition has even charge Q and it is $1, 2, 5$ when the partition has odd charge Q, as shown in Fig. 2.3 (a) and (b). For state ψ_2, the spectrum follows $1, 2, 5$ for even Q and $1, 3, 6$ for odd Q as shown in Fig. 2.3 (c) and (d).

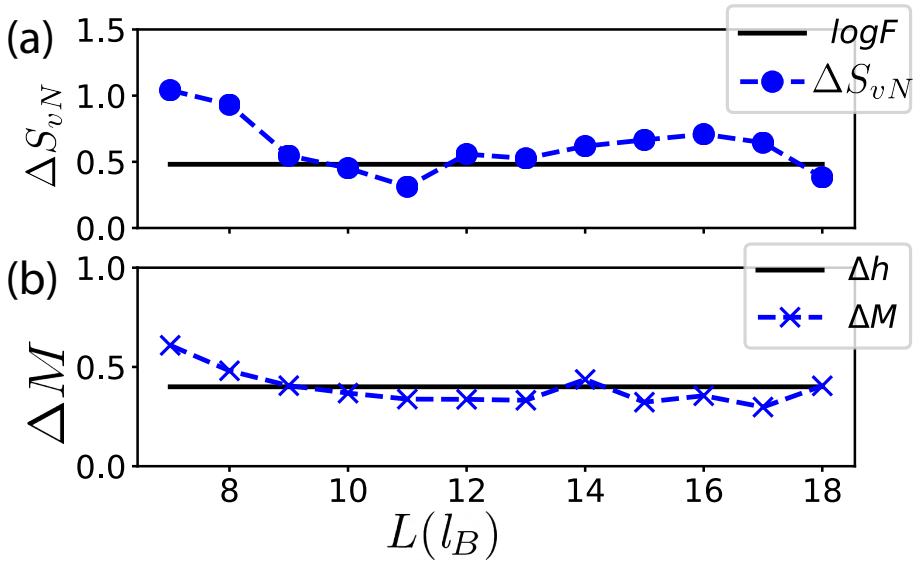

Figure 2.4: iDMRG simulation of the differences in (a) entanglement entropy (ΔS_{vN}) and (b) momentum polarization (ΔM) for the two degenerate states as a function of circumference (L). The black lines show the theoretical value of $\Delta S_{\mathbf{vN}} = S^{\tau}_{\mathrm{vN}} - S^{\mathcal{I}}_{\mathrm{vN}}$ and $\Delta M = h_\tau - h_{\mathcal{I}}$ for bilayer Fibonacci phase as described in the main text.

2.3.3 Topological Entanglement Entropy and Topological Spin

The entanglement entropy S^a_{vN} of a FQH system with an anyon type a on the infinite cylinder scales as

$$S^a_{\mathrm{vN}} = \alpha L - \gamma^a, \tag{2.6}$$

where α is a non-universal constant, L is the perimeter of the cylinder. By γ^a, we denote the topological entanglement entropy of the anyon type a, which is related to the quantum dimension d_a of the anyon a, and the total quantum dimension $\mathcal{D}$ of the topological phase via the relation $\gamma^a = \log(\mathcal{D}/d_a)$.

We calculate the difference of the entanglement entropy between the two ground states.

Since the quantum dimension of the two topological sectors are given by $d_{\mathcal{I}} = 1$ and $d_\tau = F = \frac{1+\sqrt{5}}{2}$, which is the golden ratio, we have

$$\Delta S_{\mathrm{vN}} = S^{\tau}_{\mathrm{vN}} - S^{\mathcal{I}}_{\mathrm{vN}} = \log(d_\tau / d_{\mathcal{I}}) \approx 0.48. \tag{2.7}$$

Figure 2.4(a) shows the result of ΔS_{vN}. Due to finite size effects and the truncation error of the bond dimension, the data exhibits a significant systematic error. Although we do not determine the quantum dimension unambiguously, the results are still consistent with bilayer Fibonacci phase $d_\tau = F$.

The momentum polarization M^a computes the Berry phase in the process of twisting the left half of the infinite cylinder. It is defined as $M^a = \mathrm{Tr}(\rho^a_L K)$ where ρ_L is the density matrix of the anyon type a in the left half of the infinite cylinder and K is the momentum operator on the cylinder. The momentum polarization is related to three topological invariants: the shift S, the topological spin h and the central charge c [89]:

$$M^a = -\frac{\nu S L^2}{(4\pi)^2} + h_a - \frac{c}{24} \pmod 1, \tag{2.8}$$

where L is the perimeter of the infinite cylinder and ν is the filling fraction. The difference of the momentum polarization between the two topological sectors is of the form

$$\Delta M = M^{\tau} - M^{\mathcal{I}} = h_\tau - h_{\mathcal{I}} \pmod 1. \tag{2.9}$$

The different of topological spin is given by $h_\tau - h_{\mathcal{I}} = 2/5$. Fig. 2.4(b) shows our calculation of the momentum polarization, which is consistent with the CFT prediction [73].

2.4 Spin textures at integer filling

The results presented in the previous section show that the synthetic quantum Hall bilayer is a promising candidate for realizing intriguing non-Abelian phases of matter. The crucial ingredient which gives rise to the non-Abelian behavior is the strong enhancement of the interlayer pseudpotential V_1^{inter}, when the synthetic layers are given by LL_1 and LL_2. It is interesting to further investigate the role of these exotic interactions in the synthetic bilayer. This section takes a look onto the integer quantum Hall regime, which in comparison to the regime of fractional filling factors, is technically less difficult to realize. In this context, we will focus on the charged excitation of the integer quantum Hall system, in which interactions may give rise to interesting spin structures.

In the integer quantum Hall regime, interactions play a role when the gap between two Landau levels becomes comparable to the Coulomb interaction energy. In the literature, such a situation has first been considered for systems where the two Landau levels are given by manifolds of opposite spin, separated by the Zeeman gap [75]. It has been shown that, if ferromagnetic exchange interactions overweigh the single-particle gap, then the elementary charged excitation will be a collective excitation of many electrons occupying the upper Zeeman manifold. This results in a spin texture which slowly winds around when going from the center to the edge of the system, known as a skyrmion. Similar pseudospin textures have been discussed for bilayer quantum Hall systems [78]. Here, we will investigate the spin textures in the synthetic quantum Hall bilayer using exact diagonalization and mean-field techniques.

The single-particle part of the synthetic bilayer system is described in Eq.(2.3),

$$H_0 = \sum_m -\delta\tau^z_{n,m} + \Omega\tau^x_{n,m} = \sum_m \omega_g \tilde{\tau}^z_{n,m}, \tag{2.10}$$

where the effective Zeeman energy $\omega_g = \sqrt{\delta^2 + \Omega^2}$, $\tilde{\tau}^z_{n,m} = \cos\theta\tau^z_{n,m} + \sin\theta\tau^x_{n,m}$ and $\theta = \tan^{-1}\frac{-\Omega}{\delta}$. As in usual spin systems, the Zeeman energy tends to polarize the electrons (at finite Ω in a dressed state), and the Coulomb interaction competes with it. However, in contrast to a physical bilayer, the effect of Coulomb interaction is significantly different in the synthetic bilayer. In the following, we present our results from a mean-field approach and and from an exact numerical treatment.

2.4.1 Mean field approach

In the case of non-relativistic spin-1/2 quantum Hall systems, it has been shown that skyrmionic spin textures are obtained within a mean-field description [76]. This approximation replaces the fourth-order operator products in H_{int} by second-order products,

$$c^\dagger_1 c^\dagger_2 c_3 c_4 = \langle c^\dagger_1 c_4\rangle c^\dagger_2 c_3 - \langle c^\dagger_2 c_4\rangle c^\dagger_1 c_3 + \langle c^\dagger_2 c_3\rangle c^\dagger_1 c_4 - \langle c^\dagger_1 c_3\rangle c^\dagger_2 c_4.$$

By applying this approximation, one obtains a quadratic Hamiltonian, and truncating to M orbitals per Landau level, the system is described by a $2M \times 2M$ matrix. To ease the notation, we define $a_i \equiv c_{n+1,m_i}$, $b_i \equiv c_{n,m_i}$, $a^\dagger_i \equiv c^\dagger_{n+1,m_i}$, $b^\dagger_i \equiv c^\dagger_{n,m_i}$. Further, we denote interaction matrix elements by $V^{x_1,x_2,x_3,x_4}_{1234}$, with $x_i = \{a, b\}$, and the subscript being a short-hand notation for the orbitals m_i of the scattered electrons. We distinguish between three contributions to the

mean-field interactions, $V_{\rm HF} = V_{\rm H} - V_{\rm X} + V_{\rm bg}$, which read:

$$\begin{aligned} V_{\rm H} = \sum_{\{m\}} \Big(& V^{aaaa}_{1234} \langle a_2^\dagger a_3 \rangle a_1^\dagger a_4 + V^{bbbb}_{1234} \langle b_2^\dagger b_3 \rangle b_1^\dagger b_4 + \\ & + V^{baab}_{1234} \langle a_2^\dagger a_3 \rangle b_1^\dagger b_4 + V^{abba}_{1234} \langle b_2^\dagger b_3 \rangle a_1^\dagger a_4 + \\ & + V^{abab}_{1234} \langle b_2^\dagger a_3 \rangle a_1^\dagger b_4 + V^{baba}_{1234} \langle a_2^\dagger b_3 \rangle b_1^\dagger a_4 \Big), \end{aligned} \tag{2.11}$$

being the Hartree potential,

$$\begin{aligned} V_{\rm X} = \sum_{\{m\}} \Big(& V^{aaaa}_{1234} \langle a_1^\dagger a_3 \rangle a_2^\dagger a_4 + V^{bbbb}_{1234} \langle b_1^\dagger b_3 \rangle b_2^\dagger b_4 + \\ & + V^{baab}_{1234} \langle b_1^\dagger a_3 \rangle a_2^\dagger b_4 + V^{abba}_{1234} \langle a_1^\dagger b_3 \rangle b_2^\dagger a_4 + \\ & + V^{abab}_{1234} \langle a_1^\dagger a_3 \rangle b_1^\dagger b_4 + V^{baba}_{1234} \langle b_2^\dagger b_3 \rangle a_1^\dagger a_4 \Big), \end{aligned} \tag{2.12}$$

being the exchange potential,

$$V_{\rm bg} = -\sum_{\{m\}} \Big(V^{abba}_{1221} a_1^\dagger a_1 + V^{abba}_{1221} b_1^\dagger b_1), \tag{2.13}$$

being the potential which stems from a uniform positive background (identical to a completely filled b-level). We stress that, in contrast to a spin system or a real bilayer, the interactions are not SU(2) invariant. We also highlight the existence of flipping terms, V^{abab}_{1234} and V^{baba}_{1234}, which are not present in spin systems or real bilayers.

The mean-field Hamiltonian is then solved self-consistently: An initial guess for the correlators defines the Hamiltonian $H_{\rm MF} = H_0 + V_{\rm HF}$, and the many-body eigenstates of the Hamiltonian

define the correlators. Iteratively, this leads to a self-consistent solution. To calculate the correlators from the eigenstates of H_{MF}, we note that the mean-field ground state is given by a Slater determinant over the N lowest single=particle levels, where N is the number of electrons.

Writing the kth single-particle level as $|\Psi^k\rangle = \sum_i \left(\alpha_i^k a_i^\dagger + \beta_i^k b_i^\dagger\right)|\mathrm{vac}\rangle$, the correlators with respect to the Slater determinant over the levels $1 \leq k \leq N$ are given by $\langle a_i^\dagger a_j\rangle = \sum_{k=1}^N \alpha_i^{k*}\alpha_j^k$, $\langle b_i^\dagger b_j\rangle = \sum_{k=1}^N \beta_i^{k*}\beta_j^k$, and $\langle a_i^\dagger b_j\rangle = \sum_{k=1}^N \alpha_i^{k*}\beta_j^k$.

As there are different fix points, the self-consistent solutions will not be independent from the initial guess, and to obtain a skyrmion solution, the initial guess shall already contain the skyrmionic correlations. As we are going to consider skyrmions with one electron added to the ferromagnetic ground state, the characteristic skyrmion correlations are as follows: If the ferromagnetic ground state is polarized in the b-manifold, the skyrmion is characterized by one a-particle in the center ($m = 0$), and the other particles occupy single-particle states which are superpositions of $b_m^\dagger|\mathrm{vac}\rangle$ and $a_{m+1}^\dagger|\mathrm{vac}\rangle$. The skyrmionic correlations are then characterized by non-zero coherences $\langle a_{m+1}^\dagger b_m\rangle$ and $\langle b_m^\dagger a_{m+1}\rangle$, and the spin polarization winds from a-polarized in the center to b-polarized at the edge. In contrast, if the ferromagnetic ground state is polarized in the a-manifold, the skyrmion has a b-particle in the center, its single-particle orbitals are spanned by $a_m^\dagger|\mathrm{vac}\rangle$ and $b_{m+1}^\dagger|\mathrm{vac}\rangle$, and the characteristic coherences are given by $\langle a_{m-1}^\dagger b_m\rangle$ and $\langle b_m^\dagger a_{m-1}\rangle$. The spin winding then goes from b-polarized in the center to a-polarized at the edge. As a side remark, we note that when the skyrmionic coherences are chosen as the only non-zero coherences in the initial guess, as has been done in Ref. [76], the Hartree-Fock Hamiltonian decouples into M 2-by-2 matrices. We also note that in all cases, the occupations are constrained by the number of electrons, $\langle\sum_i(a_i^\dagger a_i + b_i^\dagger b_i)\rangle = N$, which we define such that $N = M + 1$. These occupations also provide a natural bound for any of the coherences $\langle X^\dagger Y\rangle \leq \sqrt{n_X n_Y}$,

where $X, Y \in \{a_i, b_i\}$ and $n_X = \langle X^\dagger X \rangle$.

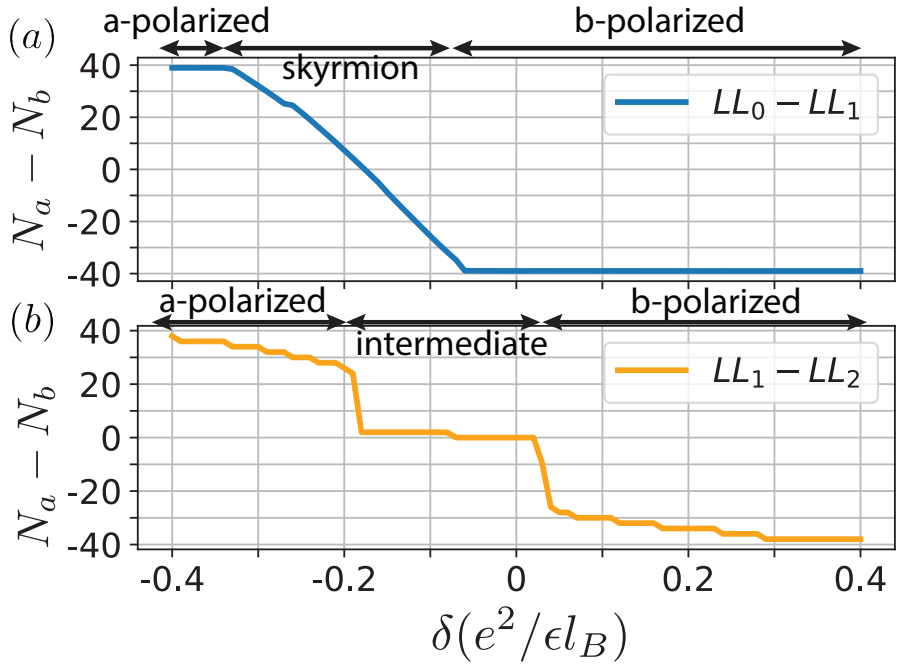

Figure 2.5: Layer occupation. The occupation difference $N_a - N_b = \sum_m \langle a_m^\dagger a_m \rangle - \langle b_m^\dagger b_m \rangle$ in a synthetic quantum Hall bilayer is plotted as a function of the detuning δ. (a) The bilayer system is obtained from coupling ($\Omega = 10^{-4} e^2/\epsilon l_B$) between LL_0 and LL_1. (b) The bilayer system is obtained from coupling between LL_1 and LL_2. We consider $M = 40$ states per Landau level, with $N = M + 1$ electrons, and initialize the self-consistent iteration scheme with non-zero coherence $\langle a_m^\dagger b_{m+1} \rangle$ and $\langle b_{m+1}^\dagger a_m \rangle$. For sufficiently strong detuning, the system is trivially polarized in the manifold favored by the detuning. When LL_0 and LL_1 are coupled, the b-polarized phase extends to the regime of weak negative detuning due to the level-dependent interactions. Between the a-polarized and the b-polarized. The system exhibits the skyrmion phase for the $LL_0 - LL_1$ whereas for the $LL_1 - LL_2$ system, an intermediate minimally polarized phase is found.

Layer occupation. A first indication of skyrmionic behavior can be seen from the layer occupation $N_a - N_b = \sum_m (\langle a_m^\dagger a_m \rangle - \langle b_m^\dagger b_m \rangle)$ as a function of the detuning δ, as illustrated in Fig. 2.5. We consider both the $LL_0 - LL_1$ synthetic bilayer, and the $LL_1 - LL_2$ synthetic bilayer. Obviously, both systems exhibit highly polarized phases for sufficiently large $|\delta|$. Interestingly, when LL_0 and LL_1 are coupled, the b-polarized phase non-trivially extends into the regime of negative

detuning. This already indicates that, in this regime, the layer polarization is not a single-particle effect, but due to the fact that the Coulombic repulsion is most efficiently minimized when the majority of particles occupy the $n = 0$ Landau level (the b-level). On the other hand, for the case of $LL_1 - LL_2$ coupling, such a phase with interaction-induced polarization is absent.

Another difference between the $LL_0 - LL_1$ bilayer and the $LL_1 - LL_2$ bilayer can be seen from Fig. 2.5: While for $LL_0 - LL_1$ coupling, the occupation N_a linearly increases as the detuning δ is decreased, the behavior in the $LL_1 - LL_2$ bilayer exhibit abrupt jumps. At $\delta \approx 0$, the system jumps from an b-polarized phase into an (almost) unpolarized phase. At $\delta \approx -0.15e^2/\epsilon l_B$, it jumps from this unpolarized phase into the a-polarized phase. This behavior is not consistent with a skyrmionic texture, which would allow for a continuous depolarization of the system. Hence, from the behavior of the layer occupation, we may already expect that skyrmions are supported by the $LL_0 - LL_1$ bilayer, but not by the $LL_1 - LL_2$ bilayer.

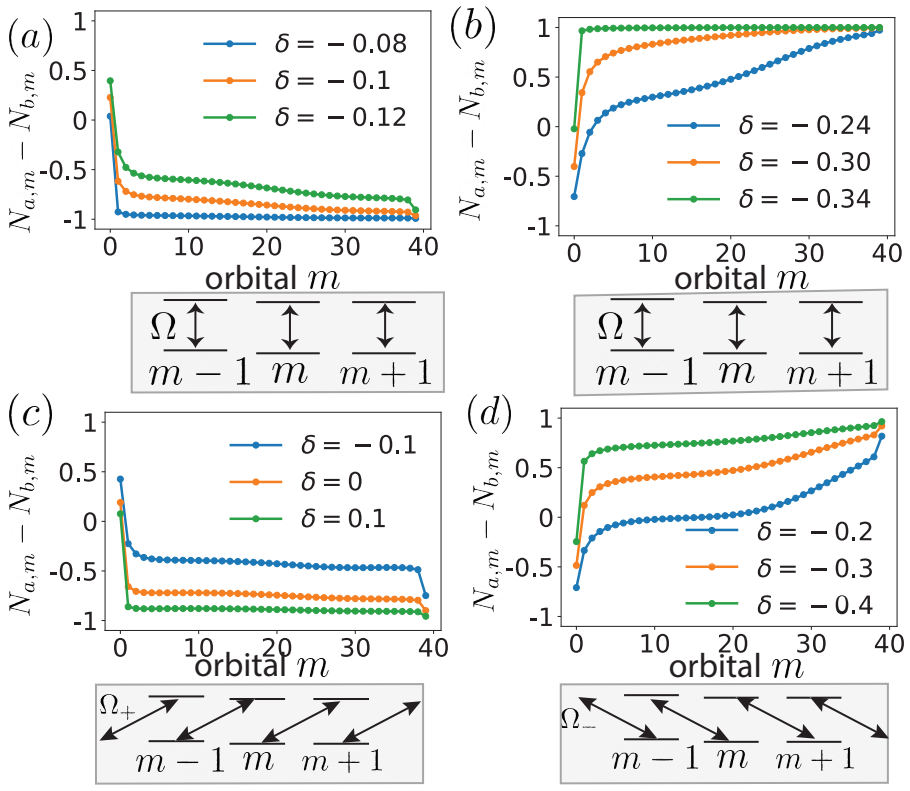

Figure 2.6: Orbital occupation. We plot the population difference $N_{a,m} - N_{b,m} = \langle a_m^\dagger a_m \rangle - \langle b_m^\dagger b_m \rangle$ between the two synthetic layers for each orbital m, for different values of the detuning δ (in units $e^2/\epsilon l_B$) The system is a $LL_0 - LL_1$ synthetic bilayer, consisting of $M = 40$ orbitals filled with $N = M + 1$ electrons. In (a), the detuning favors polarization in the b-manifold, and accordingly, the skyrmionic solution is triggered by dominant coherences $\langle a_m^\dagger b_{m-1} \rangle$ and $\langle b_{m-1}^\dagger a_m \rangle$ in the initial guess. In (b), the situation is opposite, as the detuning favors the a-manifold, and coherences $\langle a_m^\dagger b_{m+1} \rangle$ and $\langle b_{m+1}^\dagger a_m \rangle$ have to be chosen. In both panels, the Rabi coupling is $\Omega = 10^{-4} e^2/\epsilon l_B$, and it connects orbitals with equal m, as schematically indicated below each of the plots. In panel (c) and (d), all initial coherences are chosen to be very weak ($\sim 10^{-5}$) and random, and the skyrmionic solution is now triggered through coupling of photons with orbital angular momentum $\ell = \pm\hbar$, with $\Omega_+ = 0.05 e^2/\epsilon l_B$ in (c), and $\Omega_- = 0.05 e^2/\epsilon l_B$ in (d). As illustrated below the plots, such an optical coupling connects orbitals m and $m \pm 1$. In all four panels, the blue curves are chosen closer to the Zeeman-polarized regime, and the extra particle affects the polarization of only a few orbitals. In contrast, the green curves (which are furthest away from the Zeeman-polarized regime) show that most orbitals throughout the system become depolarized.

Orbital occupation. In the Fig. 2.6, we plot the orbital occupation difference $N_{a,m} - N_{b,m} = \langle a_m^\dagger a_m \rangle - \langle b_m^\dagger b_m \rangle$, where m is the orbital angular momentum. It reveals how the layer polarization

changes locally, as one moves from the center (small m) to the edge (large m) of the system. When the detuning is chosen closer to a Zeeman-polarized regime (blue curves), only the orbital in the center becomes depolarized from the presence of an extra electron (on top of filling 1). The extra particle behaves like a single-particle excitation. In contrast, when the effect of Zeeman-polarization becomes weaker (green and orange curves), more orbitals become depolarized or even oppositely polarized through the presence of the extra particle. In these cases, the layer polarization winds from one polarization to the opposite polarization, as one moves through the system. The extra particle behaves like a skyrmion.

In Fig. 2.6(a), close to the b-polarized regime, the skyrmion is obtained by choosing non-zero coherence $\langle a_m^\dagger b_{m-1}\rangle$ and $\langle b_{m-1}^\dagger a_m\rangle$ in the initial guess, and the system winds from an a-polarization in the center to b-polarization at the edge. For smaller values of δ, when the system comes closer to the a-polarized paramagnetic phase, this kind of skyrmion becomes instable. Instead, we then obtain solutions with opposite winding behavior, as shown in panel (b). These solutions are obtained from non-zero coherences $\langle a_m^\dagger b_{m+1}\rangle$ and $\langle b_{m+1}^\dagger a_m\rangle$.

In both cases, Fig. 2.6(a) and (b), the Rabi frequency must be chosen sufficiently small ($\Omega \sim 10^{-4} e^2/\epsilon l_B$) in order to obtain skyrmionic solutions. Strikingly, for the synthetic bilayer there is a relatively simple way of stabilizing the spin textures in the presence of stronger coupling: This can be achieved by replacing $\frac{\Omega}{2}(a_m^\dagger b_m + \text{h.c.})$ with $\frac{\Omega_\pm}{2}(a_m^\dagger b_{m\pm1} + \text{h.c.})$, that is, by applying a coupling with photons with orbital angular momentum $\ell = \pm\hbar$. Such a strategy has already been suggested to create topological defects in chiral magnets [93]. As we show in panel (c) and (d) of Fig. 2.6, the OAM coupling leads to very similar spin textures as in panels (a) and (b). Notably, the self-consistent equations now converge to this solution even without imposing them in the initial guess, and the spin textures remain present even for strong Rabi couplings,

$\Omega_{\pm} \sim 0.05e^2/\epsilon l_B$.

$LL_1 - LL_2$ bilayer. The behavior of the $LL_1 - LL_2$ bilayer is found to be quite different. In this case, skyrmionic correlations are fully suppressed. This is true both for the situation where we initialize the system in a state with non-zero skyrmionic correlations, and for the case where a coupling $\Omega_{\pm}$ is applied. The orbital populations will then remains close to zero throughout the system, with approximate the same population for all of the $2M$ orbitals. The dominant coherences established in the $LL_1 - LL_2$ bilayer are of the form $\langle a_m^\dagger a_{m\pm1}\rangle$ and $\langle b_m^\dagger b_{m\pm1}\rangle$. These correlations indicate antiferromagnetic ordering: If an a-type (b-type) particle occupies an orbital m, the neighboring orbitals $m \pm 1$ are unlikely to be populated by the same type of particle. Notably, these coherences acquire large non-zero values even if they are initially set to zero. This is possible only due to finite machine precision.

The absence of spin textures in the $LL_1 - LL_2$ bilayer is not very surprising if one recalls the tendency of singlet formation due to its peculiar Haldane pseudopotentials. Such interactions prevent the formation of a quantum Hall ferromagnet at $\nu = 1$, and thus, of skyrmionic excitations in the presence of $N = M+1$ electrons. This behavior illustrates, once more, that the $LL_0 - LL_1$ bilayer and the $LL_1 - LL_2$ bilayer behave in completely different ways, despite being seemingly very similar systems.

2.4.2 Exact diagonalization

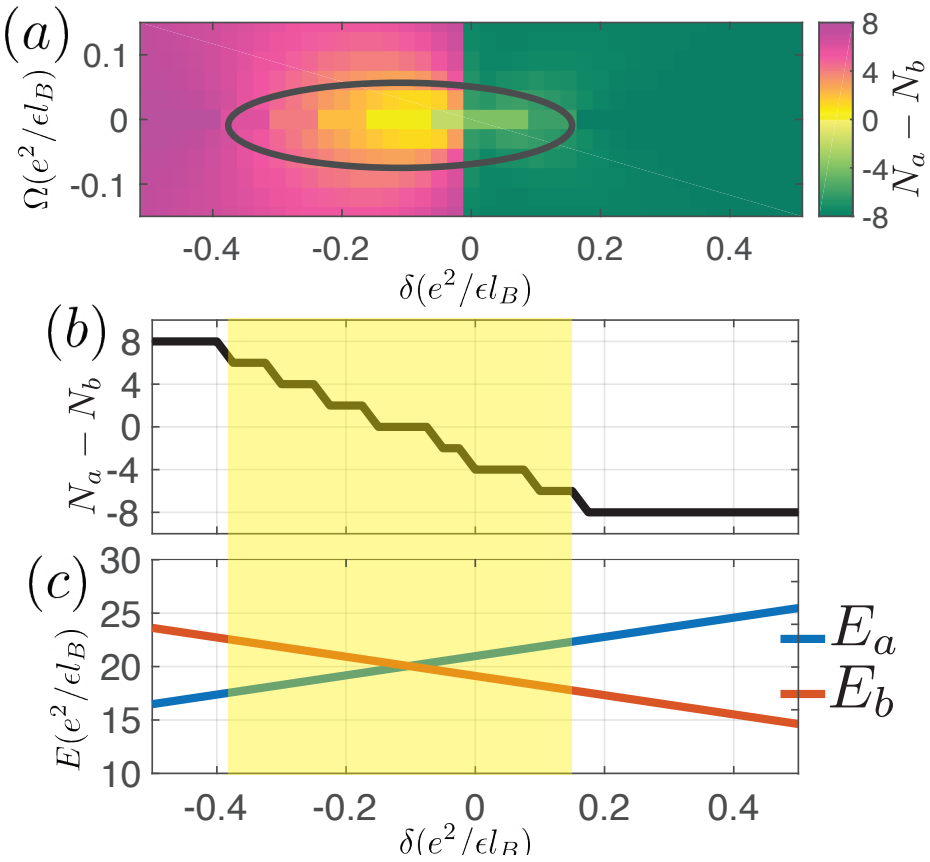

Figure 2.7: (a) The occupation difference $N_a - N_b$ as function of detunning δ and Rabi frequency Ω. As $\delta \approx -0.1$ and $\Omega \approx 0$, the occupation difference $N_a - N_b$ reaches zero, which indicates the skyrmion phase. In the simulation, we choose $N_e = 10$, $N_\phi = 9$. The skyrmion phase is enclosed in the black circle. (b) The occupation difference $N_a - N_b$ as function of δ with $\Omega = 10^{-4}(e^2/\epsilon l_B^2)$. The skyrmion phase is highlighted in the yellow region. (c) Coulomb interaction energy for the filled Landau level as function detunning δ. At $\delta = 0$, the Coulomb interaction energy of b-level is intrinsically lower than the a-level. The system exhibits the skyrmion phase when the detunning balance the unequal Coulomb interaction energy. In the simulation, we choose $N_e = 9$, $N_\phi = 9$.

In order to back our mean-field calculation, we have also performed exact diagonalization on the spherical geometry. We assume that the number of electrons is $N_e = 10$ and the total number of quantum fluxes $N_\phi = 9$. Here, we consider $LL_0 - LL_1$ coupling. In the large Zeeman energy limit, the system energetically favors a state with a single spin flip. As the Zeeman

energy decreases, the system undergoes a phase transition to the skyrmion phase. To explore the phase diagram in the regime where the detuning δ and the Rabi frequency Ω are comparable, we calculate the number difference between the dressed level $N_a - N_b = \langle \tilde{\tau}^z_{0,m} \rangle$ as shown in Fig. 2.7(a).

In the conventional bilayer quantum Hall system whith $SU(2)$ symmetric interactions, the system possesses large skyrmion excitations when the Zeeman energy vanishes. However, in the synthetic quantum Hall bilayer system, the largest skyrmion excitation occurs with the finite negative detunning, at around $\delta = -0.1$. This is in agreement with the behavior found in the mean-field calculation (cf. Fig. 2.5), indicating that this behavior is independent from the size of the system.

To understand the interplay between Coulomb interaction and the Zeeman energy in the synthetic bilayer graphene system, we show the ground state energy of the filled zeroth(first) Landau level as function of detunning in Fig. 2.7(c). When the detunning $\delta = 0$, we observe that the ground state energy of filled zeroth Landau level is higher than the filled first Landau level due to the Coulomb interaction. The unbalanced Coulomb energy competes with the formation of skyrmion. By decreasing the detunning, the energy of the two filled Landau level becomes the same. When the two Landau levels are energetically equally favorable, the size of the skyrmion reaches maximum.

2.5 Summary and outlook

In summary, we have demonstrated that the the laser field coupled to the single-layer graphene provides a versatile platform to study the bilayer quantum Hall physics. By using

the infinite density matrix renormalization group and exact diagonalization, we show that the system exhibits the bilayer Fibonacci phase which can be of interest for topological quantum computation with its non-abelian anyonic statistic. Moreover, we also explore the phase diagram for topological spin texture excitations known as skyrmion phase in the quantum Hall ferromagnetic regime. Apart from providing a synthetic bilayer structure, optical coupling between Landau levels may also enable the controlled engineering of three-body interaction terms from second-order transition processes. Future work on optically driven quantum Hall systems may explore this interesting scenario.

Chapter 3: Many-body Chern number from statistical correlations of randomized measurements

3.1 Introduction

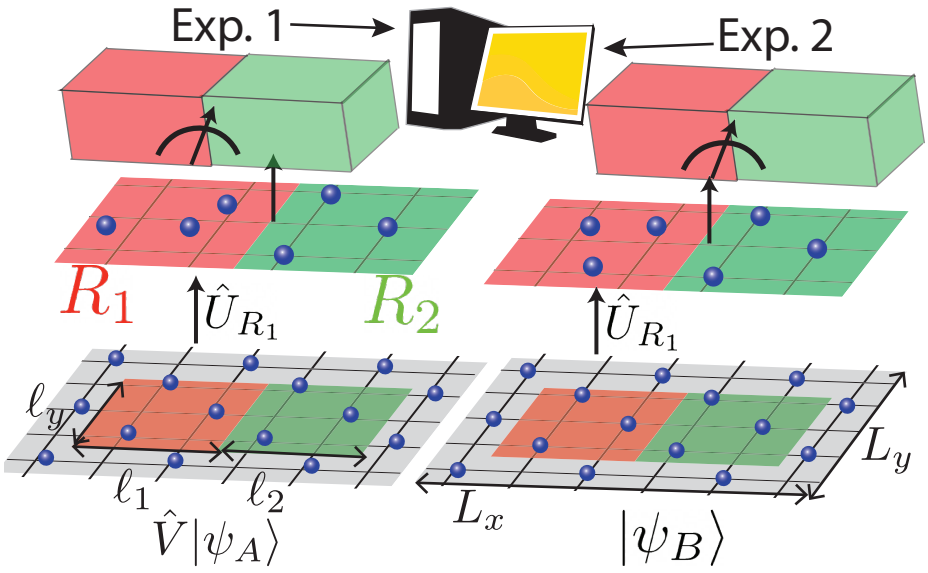

Figure 3.1: The randomized measurement scheme. We define two regions R_1 (red) and R_2 (green) in the lattice with side length $\ell_1 \times \ell_y$ and $\ell_2 \times \ell_y$ respectively. We prepare two identical wave functions ψ_A and ψ_B in experiment A and B respectively. The local unitary operator $\hat{V}$ is applied in the region R_1 in the exp. 1. Subsequently, the random unitary $\hat{U}_{R_1}$ is applied in the region R_1 on both wave functions. The projective measurements on the particle occupation basis are performed on regions R_1 and R_2 in both experiments. The MBCN can be inferred from the statistical correlation between the randomized measurement results in experiment A and experiment B.

Here, we propose a novel method for the measurement of MBCN. Using our recent findings [43], we show that given a wave function on a disk-like geometry, for a single set of parameters, one can construct the MBCN by applying certain operators on the wave function, without knowledge of the Hamiltonian. This should be contrasted with the common situation where one requires a family of many-body wave functions, e.g., different twist angles on a torus. Importantly, such a construction allows one to perform the measurements using random unitaries [94, 95, 96]. Our scheme requires only a single wave function at a given time, for the same set of parameters, as schematically shown in Fig. 4.1. In other words, in each experimental realization, one requires only a single copy of the system, and simultaneous access to several identical copies of the wave function is not required. Therefore, this scheme can be easily implemented with the state of the art ultracold atoms, Rydberg arrays and circuit-QED platforms.

First, in the context of topological quantum field theory (TQFT) [97], we interpret and generalize the polarization formula for the MBCN [43]. Our approach is extensively discussed in Ref. [43], here we outline the key concepts and results. Specifically, we demonstrate that by introducing two symmetry defects, in the space-time manifold, one can evaluate the MBCN, as an expectation value of symmetry defect operators. This allows us to effectively change the boundary conditions of the wave function. Then, by cutting and gluing space-time manifolds, we show that topologically non-trivial space-time manifolds, such as a torus, can be obtained from a given wave function on a rectangular geometry. Such operations can be obtained by applying a SWAP operator between two subregions [20]. Similar to the Renyi entropy, where the expectation of the SWAP operator can be evaluated using a single copy of the wave function at a time, we show how such space-time surgery can be implemented in an experimental setting. Importantly, we show that the symmetry defects can be implemented by post-processing the data.

As a prerequisite for our protocol, we need to know the number of flux quanta that must be adiabatically inserted into a region of the system before a topologically trivial excitation is obtained [43]. As another feature of our protocol, we note that the amplitude of the SWAP expectation value decreases exponentially with the subregions area, in the absence of spatial symmetries. Moreover, the number of randomized measurements increases exponentially with the system size. Therefore, for both reasons, our protocol is particularly suitable for Noisy Intermediate-Scale Quantum (NISQ) devices [98].

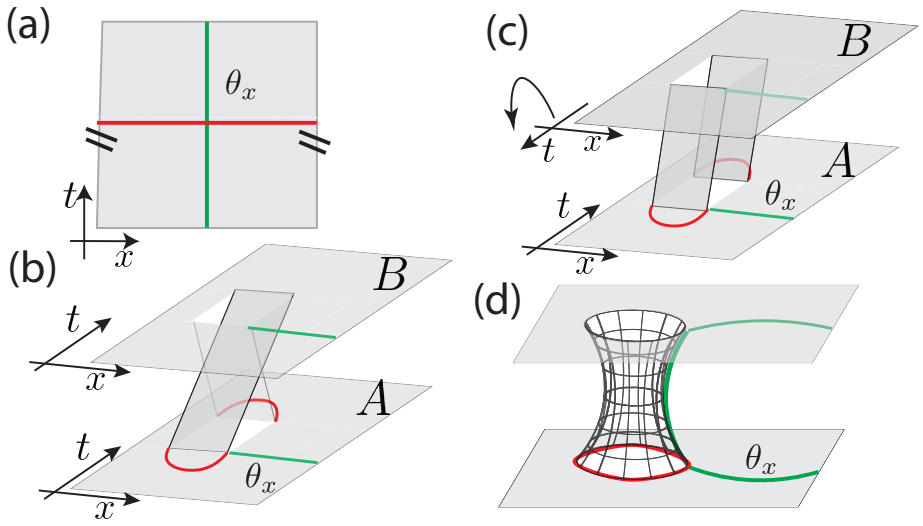

Figure 3.2: (a) The space-time manifold of the $\mathcal{Z}(M, A)$ in Eq. (3.1), without showing the y axis. The green line represents the symmetry defects A_x and the red line corresponds to A_t. (b) The SWAP operator $\hat{S}_{R_1}$ creates a branch cut in the region R_1 that connects the space time between system A and system B. The red and the green curves depict the operator $\hat{V}$ and $\hat{W}(\phi)$ respectively. (c) A π rotation around the x axis in the system B maps the branch cut in (b) to a space time cylinder which is topologically equivalent to (d).

3.2 TQFT generalization of Resta Formula

We interpret and generalize the polarization formula (1.2) using the TQFT formalism and the Chern-Simons response theory. The low-energy response of the system can be encoded in an

effective action for the background electromagnetic gauge field A, such that the TQFT partition function on a space-time manifold M is given by,

$$\mathcal{Z}(M, A) = \mathcal{Z}(M, 0)e^{i\frac{p}{q}S_{CS}[A]}. \tag{3.1}$$

The Chern-Simons response action is given by $S_{CS}[A] = \frac{1}{4\pi}\int_M \epsilon^{\mu\nu\lambda}A_\mu\partial_\nu A_\lambda$, where $\mu = t, x, y$. The space-time manifold M is $S^2 \times S^1$, where y and t are on the sphere S^2 and x is on the circle S^1. Note that $x - y$ plane forms a torus. The twisted boundary condition required in the wave functions of Eq.(1.2) can be realized by applying $A_x = \theta_x\delta(x)$ and $A_y = 0$. We interpret Resta's polarization operator as an application of an electric field along the y direction at $t = 0$ and therefore $A_t = \frac{2\pi sy}{\ell_y}\delta(t)$. Under these conditions, the partition function is given by $\mathcal{Z}(M, A) = \mathcal{Z}(M, 0)e^{iC\theta_x}$, where $C = sp/q = p$. The background gauge fields in Eq. (3.1) form two symmetry defects which are wrapped around two distinct non-contractible loops on the manifold M, as shown in Fig. 3.2(a).

Now instead of measuring the MBCN on the $x - y$ torus, here we cut and glue the space-time manifold in TQFT to construct the partition function on a topologically non-trivial manifold, by starting with the state on simple space manifolds. This allows us to create two non-contractible loops on a disk geometry. We start from two identical wave functions $\psi_A\psi_B$. We apply the SWAP operation $\hat{S}_{R_1^A,R_1^B}$ between the two wave functions in the region R_1 as shown in Fig. 4.1. For an infinitesimal time interval ϵ, the SWAP operation glues the space-time manifold from $t = \mp\epsilon$ in A to $t = \pm\epsilon$ in B, respectively, as shown in Fig.3.2(b). If we perform a π-rotation on the manifold of B along the $\hat{x}$ axis, it becomes clear that the two required non-contractible loops are formed, as shown in the Fig. 3.2 (c) and (d). These non-contractible loops are used to apply the symmetry

defects of the gauge potential A_t and A_x in this synthetic non-trivial topology.

Now, we make a connection between the TQFT and the microscopic theory to explicitly express the symmetry defects in Fig. 3.2 in terms of the system operators. These symmetry defects are local in time and can be simply constructed by the local density operator $\hat{n}(x, y)$. Specifically, the operators that represent the polarization and the twist angle are

$$\hat{V}_R = \prod_{(x,y)\in R} e^{i\frac{2\pi s y}{\ell_y}\hat{n}(x,y)}, \ \hat{W}_R(\theta_x) = \prod_{(x,y)\in R} e^{i\hat{n}(x,y)\theta_x}. \tag{3.2}$$

Now the MBCN can be obtained as the expectation value of the SWAP operator, which constructs the non-trivial space-time, and the above operators. Specifically,

$$\mathcal{T}(\theta_x) = \psi_A\psi_B\hat{V}^\dagger_{R_1^A}\hat{W}_{R_2^B}(\theta_x)\hat{S}_{R_1^A,R_1^B}\hat{W}^\dagger_{R_2^A}(\theta_x)\hat{V}_{R_1^A}\psi_A\psi_B, \tag{3.3}$$

where $R_i^{A(B)}$ is the ith region of the wave function $\psi_{A(B)}$, $\hat{S}_{R_1^A,R_1^B}$ is the swap operation between the two copy of the wave function and $\mathcal{T}(\theta_x) \propto e^{iC\theta_x}$. Therefore, the winding number of $\arg[\mathcal{T}(\theta_x)]$ corresponds to the MBCN. We note that while our TQFT derivation of this formula is applicable to cylindrical geometries, extensive numerical simulations indicates that the same formula can also be applied to disk-like geometries [43].

3.3 Randomized Measurement Scheme

We now present the experimental protocol to measure the MBCN via random measurements. Eq. (3.3) involves the SWAP operator between two copies of the wave function, and the expectation value can be obtained by performing a beam-splitter interaction between the two copies and

a parity measurement [99, 100, 101, 102]. In contrast, we show that a random measurement protocol requires only a single wave function, at a given time. Our key observation is that, without the symmetry defect operators, Eq.(3.3) is reminiscent of the second Renyi entropy expression and its evaluation through the SWAP operator expectation value, which can be extracted using randomized measurement [94]. Here, we need to generalize that scheme to incorporate the symmetry defect operators.

Let us consider a two-dimensional square lattice system with open boundary condition. Eq. (3.3) involves non-local SWAP operations between two replica of the wave functions. It can be performed through the following two randomized measurements as described in Fig. 4.1.

We start by preparing the wave function ψ in the open boundary condition. We first apply the operator $\hat{V}_{R_1}$ on the state in the experiment A. We then perform the random unitary operation $\hat{U}$ and the measurements on the occupation probability in the region R_1 and R_2 for both experiment A and B. The random unitary operations are sampled from an approximate unitary 2-design [103, 104]. After repeating the measurement N_M times, we obtain the probability distribution over the occupation basis b. The results of the two experiments are $P_U^V(b) = |\langle b|\hat{U}\hat{V}|\psi\rangle|^2$ and $P_U(b') = |\langle b'|\hat{U}|\psi\rangle|^2$ respectively. We repeat the two experiments with different random unitary operations $\hat{U}$ for N_U times. The statistical correlation of the measurement results in the experiment A and B gives

$$\tilde{\mathcal{T}}(\theta_x) = \sum_{\{b\}} \sum_{\{b'\}} O_{b,b'}(\theta_x) \overline{P_U^V(b) P_U(b')}, \tag{3.4}$$

where the bar, $\overline{\cdots}$, means the average over the random unitaries from an approximate unitary 2-

design. The coefficient $O_{b,b'}(\theta_x) = \delta_{N_1(b),N_1(b')}\mathcal{D}_b(-\mathcal{D}_b)^{\delta_{b,b'}-1}e^{i[N_2(b)-N_2(b')]\theta_x}$, where $N_1(b)$ and $N_2(b)$ are the number of particles of the basis state $|b\rangle$ in the region R_1 and R_2 respectively and $\mathcal{D}_b = \binom{\ell_1\ell_y}{N_1(b)}$. Since $\tilde{\mathcal{T}}(\theta_x) = \mathcal{T}(\theta_x)$ for an ensemble average over a unitary 2-design [1], the winding number of the measurement result $\arg[\tilde{\mathcal{T}}(\theta_x)]$ gives the Chern number $\tilde{C}$.

In the following, we consider the randomized measurement scheme for system with non-trivial Chern number with finite number of N_U and number of projective measurements N_M for each realization of randomized measurement.

3.4 Numerical results

We present the measurement of MBCN for bosonic fractional quantum Hall states with filling $\nu = 1/2$. We consider hard-core boson on the $N_x \times N_y$ square lattice in the open boundary condition, with a magnetic tunneling Hamiltonian of the form

$$H_{\mathrm{t}} = -J\sum_{x,y}(\hat{a}^\dagger_{x+1,y}\hat{a}_{x,y} + e^{-i\Phi x}\hat{a}^\dagger_{x,y+1}\hat{a}_{x,y}) + \mathrm{h.c.}, \tag{3.5}$$

where $\hat{a}_{x,y}(\hat{a}^\dagger_{x,y})$ is the bosonic annihilation (creation) operator on site (x, y), $\Phi = 2\pi/q$ is the magnetic flux on each plaquette. The ground state is known to be a FCI phase, with the MBCN $C = 1$ [105, 106, 107]. The FCI ground state with the open boundary condition can be prepared via adiabatic process [106, 107] [2] and engineered dissipation [108]. We note that the system size of our simulation is within reach to the state of the art quantum computation platform [109].

In Fig. 3.3(a), we first show that the MBCN of this phase can be extracted, using the SWAP

[1] See supplementary for the derivation.
[2] See supplementary for details

operator formula, Eq. (3.3). We observe that the correct quantized value $\tilde{C} = 1$ can be obtained, when the region size is larger than the magnetic length of the system, which is less than a lattice spacing in our case.

Then, in Fig. 3.3(b-d), we show that the MBCN can be extracted using randomized measurement (Eq.(3.4)). In order to implement random unitaries, we apply quench dynamics [95]. We consider the number conserving random quench unitary operation $\hat{U} = \prod_{k=1}^{\eta} e^{-iH_{q_k}T}$, where η is the depth of the random quench, T is the time step of each quench. The kth quench Hamiltonian is of the form

$$H_{q_k} = -J \sum_{\langle i,j\rangle,\ i,j\in R_1} (a_i^\dagger a_j + \mathrm{h.c.}) + \sum_{\mathrm{i}\in\mathrm{R}_1} \Delta_{\mathrm{i}}^{\mathrm{k}} \hat{\mathrm{n}}_{\mathrm{i}}, \tag{3.6}$$

where Δ_i^k is a Gaussian distributed random number with mean zero and standard deviation Δ. It has been shown that when the magnitude of Δ is comparable to T^{-1} and J, the random quench unitary operator gives the approximate 2-design unitary [95].

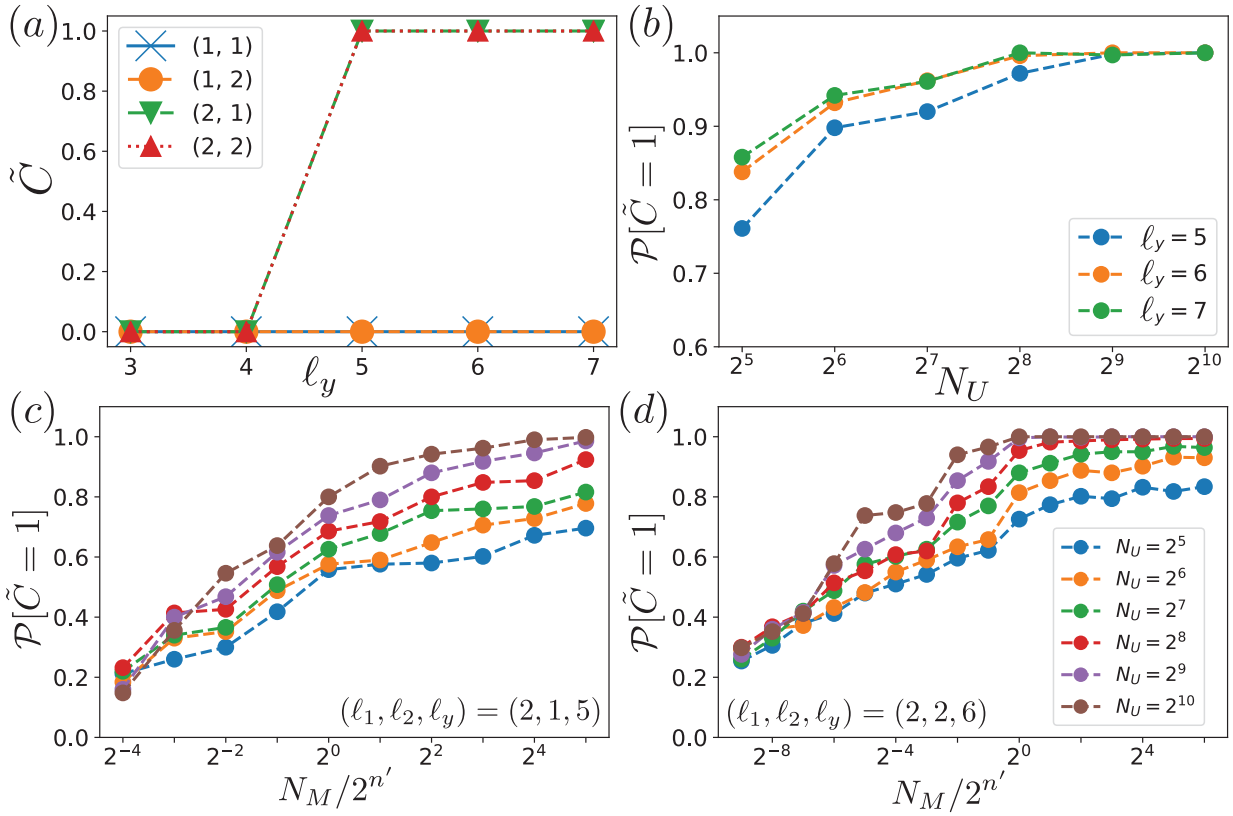

Figure 3.3: Simulation results for Eq. (3.3) and (3.4), for the FCI phase with $C = 1$. (a) Obtained MBCN by Eq. (3.3) for various region size (ℓ_1, ℓ_2) and ℓ_y with $N_x = 6$, $N_y = 8$. , labeled with different markers. (b) Probability of obtaining the expected MBCN ($\mathcal{P}[\tilde{C} = 1]$) from Eq. (3.4), using randomized measurements, as a function of the number of random unitary operations N_U with $N_M = \infty$. Region sizes are taken to be $\ell_1 = \ell_2 = 2$. (c, d) Probability of obtaining the expected MBCN versus number of measurements N_M, for two sets of region sizes. For all panels, $J = 1$, and $\Phi = 2\pi/3$. the probability $\mathcal{P}[\tilde{C}]$ is computed by averaging over 500 times independent randomized measurement results. Random quench parameters are $\eta = 20$, $\Delta = J$, $T = J^{-1}$ and $n' = 0.5n_1 + n_2$.

The performance of the randomized measurement is characterized by the probability of obtaining the correct MBCN $\mathcal{P}[\tilde{C} = 1]$. In Fig. 3.3(b), we consider the limit of $N_M \to \infty$, the performance of the randomized measurement weakly depends on the number of qubits in the measurement region R_1 and R_2. In Fig. 3.3 (c) and (d), the shot-noise of the measurements are taken into account. When the number of measurements N_M is of the same order of magnitude as $2^{n'}$, where $n' = 0.5n_1 + n_2$, and n_1 and n_2 are the number of sites in the region R_1 and R_2

respectively, the probability $\mathcal{P}[\tilde{C} = 1]$ starts to saturate. The factor $2^{0.5n_1}$ originates from the birthday paradox scaling of the randomized measurement in the region R_1 [94] and the factor 2^{n_2} is contributed by the shot-noise of the number operator measurement in the region R_2. The randomized measurements can be realized in the current and near-term experimental platform. For example, in the circuit QED architecture with 10kHz repetition rate, each randomized measurement can be performed within a few minutes.

3.5 Robustness against errors of the NISQ devices

In order to demonstrate the feasibility in the NISQ devices, we show that our protocol is robust against various types of experimental imperfections. First, we note that the randomize measurement protocol is robust against the small miscalibration of the quantum hardware. It has been shown that the leading order contribution of the miscalibration vanish in the randomized measurement protocol [110].

For the amplitude damping error and the readout error, since the total number of excitations in the whole system is conserved during the state preparation and random unitary gate, when either the amplitude damping error or the readout error occurs, the total number of excitation is changed. A change of the number of excitation heralds an error and the run should be discarded. Therefore, up to the first order of the error rates, the amplitude damping error or the readout error can be detected.

In the case of the depolarization error, the quantum state after performing the random

unitary operation is of the form

$$\rho_{\text{dep}} = (1 - p_{\text{dep}})\rho_{\text{ideal}} + \frac{p_{\text{dep}}}{\mathcal{D}} I_{\mathcal{D}} + O(p_{\text{dep}}^2), \tag{3.7}$$

where ρ_{ideal} is the density matrix in the ideal situation, $\mathcal{D}$ is the dimension of the Hilbert space and p_{dep} is the depolarization probability. After performing the measurement and post-processing described in Eq. (3.4), we have

$$\tilde{\mathcal{T}}_{\text{dep}}(\theta_x) \approx (1 - p_{\text{dep}})^2 \tilde{\mathcal{T}}(\theta_x) + p_{\text{dep}} c(\theta_x), \tag{3.8}$$

where $c(\theta_x)$ is a constant offset which can be calculated from the measurement results [3].

Since the amplitude of $\tilde{\mathcal{T}}(\theta_x)$ is rescaled, the number of measurements should be increased in order to have converged results. For example, one can increase the number of random unitary N_U by a factor of $\frac{1}{(1-p_{\text{dep}})^4}$ in order to increase the measurement accuracy by a factor of $(1-p_{\text{dep}})^2$ [94]. The winding number of $\tilde{\mathcal{T}}(\theta_x)$ can be extracted by fitting the measurement result in Eq. (3.8) with parameters θ_x and p_{dep}.

3.6 Derivation of Eq. (3.4)

In this supplementary, we derive Eq.(3.4) in the main text, which allows us to extract the MBCN from the statistical correlations of randomized measurements.

We start by considering two arbitrary density matrices ρ_A and ρ_B with dimension $\mathcal{D}$. As shown in [94], the expectation value of the SWAP operator can be implemented by the 2-design

[3] See supplementary for the derivation.

random unitary operations of the form

$$tr(\rho_A \otimes \rho_B \hat{S}_{A,B}) = \mathcal{D} \sum_{s_1,s_2} (-\mathcal{D})^{1-\delta_{s_1,s_2}} \overline{P_U^A(s_1) P_U^B(s_2)}, \tag{3.9}$$

where $P_U^\alpha(s) = tr(U\rho_\alpha U^\dagger ss)$ and $\alpha = A, B$.

Notice that the right hand side of the above equation can be written as

$$\begin{aligned} & \mathcal{D} \sum_{s_1,s_2} (-\mathcal{D})^{1-\delta_{s_1,s_2}} \overline{P_U^A(s_1) P_U^B(s_2)} \\ = \; & \mathcal{D} \sum_{s_1,s_2} (-\mathcal{D})^{1-\delta_{s_1,s_2}} \\ \times \; & \overline{tr(s_1 s_1 \otimes s_2 s_2 U \otimes U\rho_A \otimes \rho_B U^\dagger \otimes U^\dagger)} \\ = \; & \overline{tr(U^\dagger \otimes U^\dagger \hat{O} U \otimes U\rho_A \otimes \rho_B)}, \end{aligned} \tag{3.10}$$

where $\hat{O} = \mathcal{D} \sum_{s_1,s_2} (-\mathcal{D})^{1-\delta_{s_1,s_2}} s_1 s_1 \otimes s_2 s_2$.

By using the 2-design property of the random unitary operation, we obtain

$$\begin{aligned} \overline{U \otimes U\hat{O}U^\dagger \otimes U^\dagger} = & \frac{1}{\mathcal{D}^2 - 1} (tr(\hat{O}) - \frac{1}{\mathcal{D}} tr(S_{A,B}\hat{O}))\hat{I} \\ & + \frac{1}{\mathcal{D}^2 - 1} (tr(\hat{S}_{A,B}\hat{O}) - \frac{1}{\mathcal{D}} tr(\hat{O}))\hat{S}_{A,B}, \end{aligned} \tag{3.11}$$

Since $tr(\hat{O}) = \mathcal{D}$ and $tr(\hat{O}\hat{S}_{A,B}) = \mathcal{D}^2$, we arrive at equation (3.9).

Using equation (3.9), now we can rewrite $\mathcal{T}(\theta_x)$ defined in the main text, in terms of statistical correlations,

$$\mathcal{T}(\theta_x) = \tilde{\psi_A}\psi_B \hat{W}^\dagger_{R_2^B}(\theta_x) \hat{S}_{R_1^A, R_1^B} \hat{W}_{R_2^A}(\theta_x) \tilde{\psi_A}\psi_B, \tag{3.12}$$

where $\tilde{\psi}_A = \hat{V}_{R_1^A}\psi$.

Since the operators $\hat{W}_{R_2^A}$ and $\hat{W}_{R_2^B}$ are diagonal in the particle occupation basis, we can apply it after projective measurements. Specifically, we use the following identity

$$\begin{aligned}\mathcal{T}(\theta_x) &= \sum_{s_{R_2}, s'_{R_2}} e^{iN(s_{R_2})\theta_x} e^{-iN(s'_{R_2})\theta_x} \\ &\times \tilde{\psi}_A \psi_B \hat{S}_{R_1^A, R_1^B} \hat{P}^A_{s_{R_2}} \hat{P}^B_{s'_{R_2}} \tilde{\psi}_A \psi_B, \end{aligned} \tag{3.13}$$

where s_{R_2} is the basis of particle number configuration in the region R_2, $N(s)$ is the number of particle in the basis state s and $\hat{P}^{A(B)}_{sR2}$ is the projector that projects the particle configuration in the region R_2 into the state s_{R_2}.

Now, we perform the partial trace operator on wave functions A and B and only keep the region R_1. Correspondingly, we can rewrite (3.13) as,

$$\begin{aligned}\mathcal{T}(\theta_x) &= \sum_{s_{R_2}, s'_{R_2}} e^{iN(s_{R_2})\theta_x} e^{-iN(s'_{R_2})\theta_x} \\ &\times tr(\rho_{A;s_{R_2}} \otimes \rho_{B;s'_{R_2}} \hat{S}_{R_1^A, R_1^B}), \end{aligned} \tag{3.14}$$

where the reduced density matrix is defined as $\rho_{p;s_{R_2}} = tr_{R/R_1}(\hat{P}_{s_{R2}}|\psi_p\rangle\langle\psi_p|)$, where $p = A, B$.

For the ground state of a number conserving Hamiltonian, the reduced density matrix $\rho_{p;s_{R_2}}$ can be written as the direct sum of the density matrix with different number of particles. Therefore, $\rho_{p;s_{R_2}} = \bigoplus_{k=0}^{\infty} \rho^k_{p;s_{R_2}}$, where $\rho^k_{p;s_{R_2}}$ is the reduced density matrix with k particle in the region R_1.

The SWAP operation $\hat{S}_{R_1^A, R_1^B}$ is a number conserving operation and it can also be factorized into the direct sum of SWAP operations with different number of particles sectors $\hat{S}_{R_1} = \bigoplus_{k=0}^{\infty} \hat{S}^k_{R_1}$.

Equation (3.14) can be simplified as

$$\begin{aligned}\mathcal{T}(\theta_x) &= \sum_{s_{R_2}, s'_{R_2}} e^{iN(s_{R_2})\theta_x} e^{-iN(s'_{R_2})\theta_x} \\ &\times \bigoplus_{k=0}^{\infty} tr(\rho^k_{A;s_{R_2}} \otimes \rho^k_{B;s'_{R_2}} \hat{S}^k_{R_1}).\end{aligned} \tag{3.15}$$

The SWAP operator in the k-particle sector can be implemented by equation (3.9) with the random unitary acting on the k-particle sector $\hat{U}_k$ which can be implemented with the random quench dynamics with number conserving Hamiltonian. By replacing the SWAP operation in equation (3.15) by the random unitary operation defined in equation (3.9), we reach equation (3.3) in the main text.

3.7 The Randomized measurement under depolarizing channel

In this section, we focus on the depolarizing error when implementing the random unitary operations $\hat{U}$ in the region R_1. Without the depolarizing error, the measurement results of the two experiments are $P^V_U(b) = |b\hat{U}\hat{V}\psi|^2$ and $P_U(b) = |b\hat{U}\psi|^2$ as defined in the main text. In the presence of the depolarizing error in the region R_1, the measurement results become

$$\begin{aligned}P^{V'}_U(b) &= (1 - p_{\text{dep}}) P^V_U(b) + \frac{p_{\text{dep}}}{\mathcal{D}_{R_1}}, \\ P'_U(b) &= (1 - p_{\text{dep}}) P_U(b) + \frac{p_{\text{dep}}}{\mathcal{D}_{R_1}},\end{aligned} \tag{3.16}$$

where $\mathcal{D}_{R_1}$ is the dimension of Hilbert space in the region R_1. If we substitute the equation above to eq. (7) in the main text, we have

$$\mathcal{T}'(\theta_x) \;\; = \;\; (1-p_{\rm dep})^2\mathcal{T}(\theta_x) + p_{\rm dep}c(\theta_x), \tag{3.17}$$

where $c(\theta_x) = \frac{1}{\mathcal{D}_{R_1}} \sum_b \sum_{b'} O_{b,b'}(\theta_x)[\overline{P_U^V(b)} + \overline{P_U(b)}]$.

In the equation above, we assume that $p_{\rm dep} \ll 1$ and therefore we neglect the terms of order $O(p_{\rm dep}^2)$. The function $c(\theta_x)$ can be simplified as

$$\begin{aligned} c(\theta_x) &= \tfrac{1}{\mathcal{D}_{R_1}} \textstyle\sum_b \sum_{b'} O_{b,b'}(\theta_x)[\overline{P_U^V(b)} + \overline{P_U(b)}] \\ &= \tfrac{1}{\mathcal{D}_{R_1}} \textstyle\sum_{b_1} \mathcal{D}_{b_1} \sum_{b_2,b_2'} e^{iN_2(b_2)\theta_x} e^{-iN_2(b_2')\theta_x} [\tfrac{P(b_2)}{\mathcal{D}_{b_1}} + \tfrac{P(b_2')}{\mathcal{D}_{b_1}}] \\ &= \textstyle\sum_{b_2'} e^{-iN_2(b_2')\theta_x} \sum_{b_2} e^{iN_2(b_2)\theta_x} P(b_2) + c.c. \\ &= \textstyle\sum_{b_2'} e^{-iN_2(b_2')\theta_x} \sum_{k} e^{ik\theta_x} P(N_2 = k) + c.c., \end{aligned} \tag{3.18}$$

where $P(N_2 = k)$ is the probability of having k particles in the region R_2.

From the first line to the second line above, we use the 1-design property of the random unitary and we define the probability of measuring the configuration b_2 in the region R_2 as $P(b_2)$. In the final expression, we observe that $c(\theta_x)$ can be uniquely determined if we measure $P(N_2 = k)$ for all k, which can be obtained from the measurement results $P_U(b)$.

3.8 Adiabatic preparation of FCI

In order to experimentally realize the above FCI state, one can start by a Mott insulator state, by adding a trapping potential in form of a superlattice $V_{\text{trap}} = M\sum_{x,y}(-1)^{y+p_x}\hat{n}_{x,y}$, where and $p_x = \text{floor}(\text{x}/\text{q})$ [105, 106]. Specifically, the Mott insulator for large trapping strength M, can be adiabatically melted into a FCI state by decreasing the strength M. In Fig. 3.4, we consider an adiabatic process with $M(t) = M_0(1 - t/T_{ad})$, where M_0 is the initial trapping strength and T_{ad} is the adiabatic preparation time. The energy gap remains open in the process of adiabatic preparation, as shown in Fig. 3.4(b). For slow enough sweep, the overlap between the instantaneous ground state and the adiabatic wave function remains higher than 0.999 for $T_{ad} = 100J^{-1}$, as shown in Fig.3.4 (c). In Fig. 3.4(d), we show that the randomized measurement results agree with the theoretical values, in both trivial and topological limits. However, if the sweep time is not in the adiabatic limit, e.g., $T_{ad} = 1J^{-1}$ as in Fig. 3.4 (c) and (d), then the system deviates from the FCI phase.

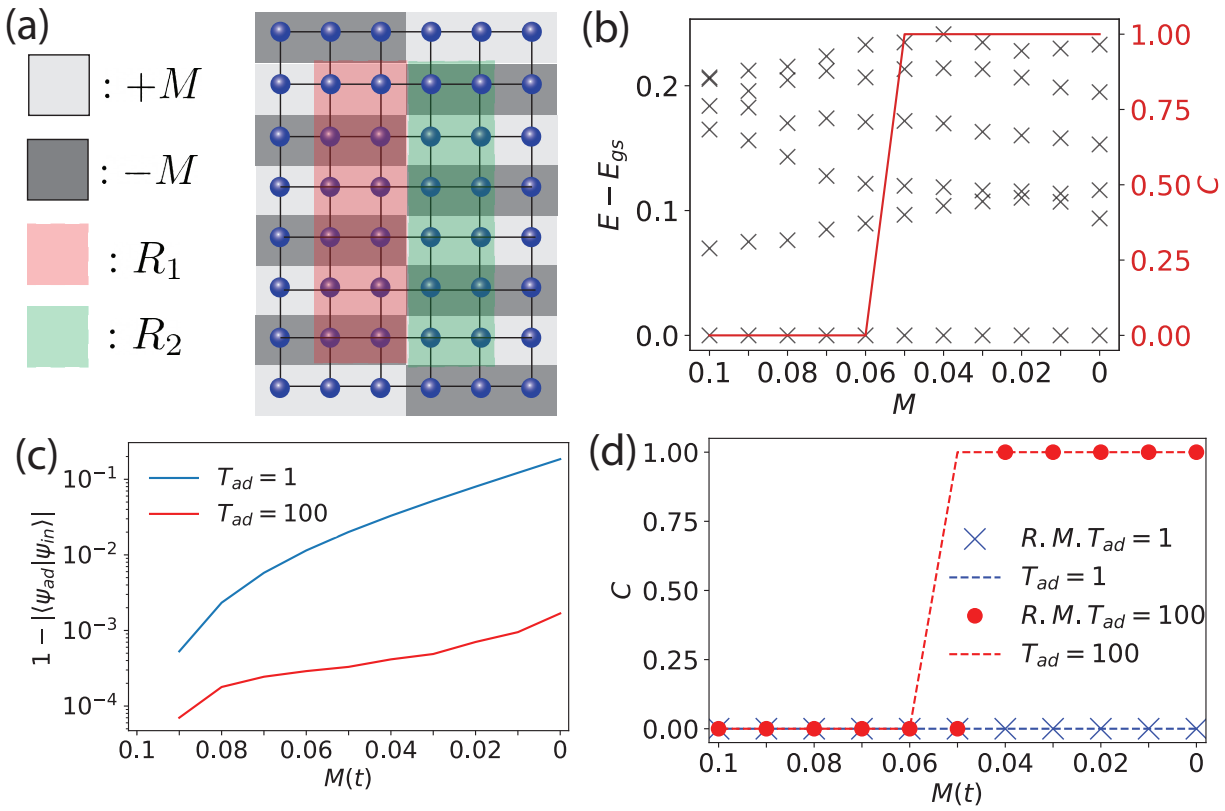

Figure 3.4: Adiabatic preparation of FCI and measurement of MBCN by varying a trapping potential. (a) Schematics of the system considered in the simulation, with open boundary condition and $N_x = 6$, $N_y = 8$. Region lengths are $\ell_1 = 2$, $\ell_2 = 2$, $\ell_y = 6$ and $\Phi = 2\pi/3$. The potential energy is $-M/+M$ in the dark/bright regions, respectively. (b) The energy spectrum, and the corresponding MBCN as a function of M. (c) The fidelity $1 - |\langle\psi_{in}|\psi_{ad}\rangle|$, where $|\psi_{in}\rangle$ is the instantaneous eigenstate and the $|\psi_{ad}\rangle$ is the adiabatic wave function prepared by linearly decreasing the trapping strength M, with the preparation time T_{ad}. (d) The MBCN randomized measurement results with parameters $N_U = 1024$, $N_M = 2^{n'}$, $\eta = 20$, $\Delta = 1$ and $T = 1$.

3.9 Summary and outlook

Our work opens up a new avenue for creating non-trivial topology on space-time manifold, using the SWAP operation. It is particularly intriguing that the SWAP operation can be implemented by random unitaries in the NISQ devices. More broadly, quantum simulators are poised to realize topologically-ordered states that might not occur in a conventional electronic matter. Given this opportunity, it is important to develop measurement methods that go beyond linear response

formalism. For example, it is interesting to investigate whether the application of SWAP operator through randomized measurement can be used to probe other topological characterizations, such as modular matrices [111], topological entanglement entropy [27, 28] and the order parameter of the symmetry enriched topological phases [112].

Chapter 4: Extracting Wilson loop operators and fractional statistics from a single ground state on a disk

4.1 Introduction

Topologically ordered phases are gapped quantum phases of matter that cannot be characterized by local order parameters, but rather by long-range entanglement and fractional statistics of quasiparticle excitations. For decades, a major question has been how to properly diagnose and characterize topological order in a quantum many-body system. While much progress has been made [22, 23, 50, 51, 113, 114, 115, 116, 117], an outstanding question remains: Can we fully extract topological order from a single bulk ground state wave function, with no access to the Hamiltonian?

Apart from the fundamental interest in the above question, there is a growing body of experimental effort in creating topologically ordered matter in quantum simulators. Recent examples include the implementation of toric code in superconducting qubit systems [118], and dimer models in Rydberg arrays [119, 120]. Since various kinds of perturbation are present in any experimental implementation, the precise Hamiltonian may not be known and may depart significantly from that of the pristine, idealized models. It is thus important to find a systematic approach to characterize topological order given a wave function, with minimal knowledge of the

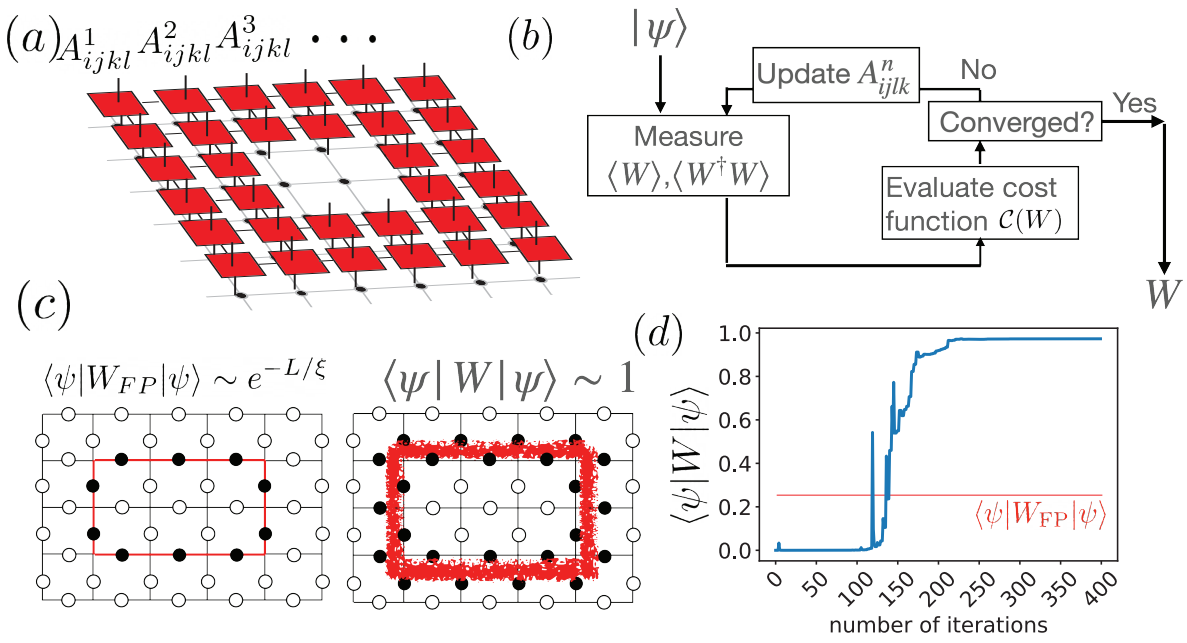

Figure 4.1: (a) WLO parameterized with a matrix product operator. (b) Numerical procedure to optimize a WLO. (c) The expectation value of the WLO W_{FP} for the exactly solvable fixed point follows perimeter law when evaluated in the perturbed ground state: $\langle\psi|W_{\mathrm{FP}}|\psi\rangle \sim e^{-L/\xi}$, where L and ξ are the perimeter of W_{FP} and correlation length, respectively. However, the expectation value of the optimized Wilson loop operator does not decrease exponentially with the perimeter. (d) The expectation value of the Wilson loop operator $\langle\psi|W|\psi\rangle$ during the optimization iteration described in (b). The typical total number of iterations is around 400. $|\psi\rangle$ is a ground state of the perturbed toric code model with $h_x = 0.15$, $h_z = 0.05$. The Wilson loop operator is a rectangle with side length $L_x = 36$ and $L_y = 6$ and thickness 1.

Hamiltonian.

From a modern perspective, one key aspect of topological order is the existence of an emergent, higher symmetry. To each curve in space, there exists a set of Wilson line operators (WLOs), which correspond to adiabatically transporting topologically non-trivial quasiparticles along γ. If γ is a contractible loop, the corresponding Wilson loop operators, or closed WLOs, keep a particular ground state invariant [40], while a WLO with open ends creates quasiparticle excitations near the two endpoints of γ. In this sense, the closed WLOs on contractible loops can be thought of as an *emergent* symmetry of the ground state.[1] The symmetry is emergent in general

[1]Closed WLOs on non-contractible loops can be thought of as a spontaneously broken emergent symmetry [54], because while they keep the ground state subspace invariant, implying an emergent symmetry, they act non-trivially

because, aside from certain exactly solvable models [52, 53], the Hamiltonian need not commute with these WLOs. In contrast to ordinary symmetries, which are implemented by operators with support over the entire space, the closed WLOs have support only on loops; in the case where all topological quasiparticles are Abelian, the WLOs can be thought of, in modern terminology, as emergent 1-form symmetries of the system [54]. These WLOs should in principle contain all of the data that characterizes the topological order, however it is not well-understood how to tease it out in practice.

In this work, we propose a numerical method to systematically search for a complete set of Wilson loop operators for the case of Abelian topological orders, using only the ground state of a gapped Hamiltonian defined on a disk-like region of space. We do this by considering a variational ansatz for Wilson loop operators in terms of a matrix product operator with support on a ribbon along γ, as schematically shown in Fig. 4.1(a). We then set up a cost function in terms of the variational parameters of the WLOs. The minima of the cost function, which we numerically optimize for, gives the WLOs as diagrammatically shown in Fig. 4.1(c). The obtained Wilson loop operator expectation value can reach close to unity after a few hundred iterations (Fig. 4.1(d)). We emphasize that our procedure is *unbiased* and assumes no prior knowledge of the form of the WLOs.

Once the WLOs are obtained, we show how one can perform further optimization-based schemes to find operators that can create, move, and annihilate the anyons. Finally, we show that these operators can be utilized to extract the modular S and T matrices of an Abelian topological order, which gives a complete characterization of the topological order. In particular the S and T matrices encode all of the information about the fractional statistics.

on ground states, implying 'spontaneous symmetry breaking.'

We successfully demonstrate our numerical protocol in models with non-zero correlation lengths. For example, we show how one can extract the modular S and T matrices from only the ground states of the perturbed toric code and doubled semion models, with a Zeeman field that is up to half of the critical value.

To date, several invariants of two-dimensional topologically ordered states have been shown to be obtainable from the ground state wave function through a variety of methods. This includes the total quantum dimension measured through topological entanglement entropy [27, 28], the many-body Chern number and Hall conductance [33, 34, 121], various invariants of symmetry-protected topological (SPT) states [19, 20, 21], and the chiral central charge [35, 36, 37, 38, 39]. The modular S and T matrices, which encode details of the fractional statistics of the quasiparticles, can, under certain conditions, be extracted from the full set of ground states on a torus [29, 30, 31] or in the presence of twist defects [32], but not to date from a single ground state on a disk.

We note that Ref. [122, 123] also proposed to find WLOs through an optimization approach, by searching for WLOs that commute with the Hamiltonian. However generic systems are not expected to have WLOs that commute with the Hamiltonian; instead as discussed above WLOs only appear as emergent symmetries that keep the ground state subspace invariant. Our work, in contrast to Ref.[122, 123], uses only the ground state without requiring knowledge of the Hamiltonian.

The paper is organized as follows. In Sec. 1.3, we review the basic properties of Wilson line operators and the algebraic theory of anyon. In Sec. 4.2, we provide the optimization scheme for probing closed Wilson loop operators. In Sec. 4.3, we propose the scheme to create, move, annihilate anyons and measure the topological twist. We present numerical simulations

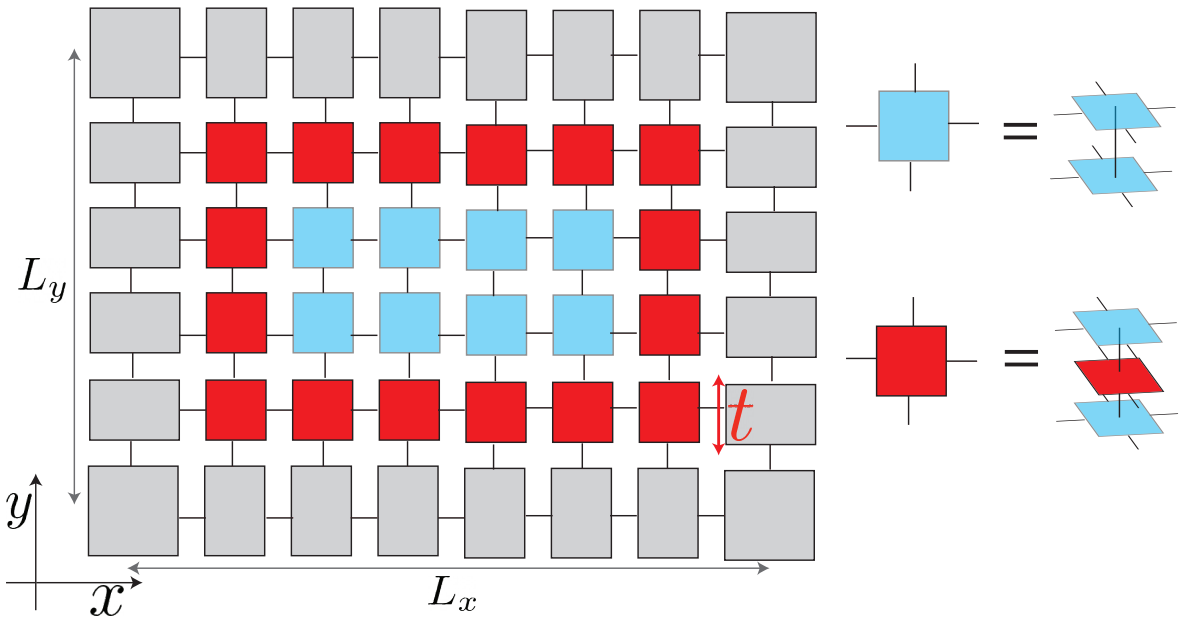

Figure 4.2: Illustration of the tensor contraction for calculating $\langle\psi|W|\psi\rangle$. The gray tensors represents corner transfer matrix (CTM). The blue tensors are the contraction of the bra and ket of the PEPS wave function. The two are connected by contraction of the physical bond. The red tensors are the contraction of the PEPS wave function and the WLOs.

for abelian topological order models in Sec. 4.4. Finally, we provide an outlook for future works in Sec. 4.5.

4.2 Optimization Scheme

In order to study the WLOs in the bulk of a ground state wave function, we propose a numerical scheme to extract contractible closed WLOs $W_a(\gamma)$ as defined in Eq. (1.6). We parametrize the WLOs by an ansatz based on matrix product operators (MPOs) [122, 124, 125]. The ansatz is defined by two parameters: (R, χ), where R is a set of sites corresponding to the support of the WLO and χ is the bond dimension, as shown in Fig. 4.1. For a certain class of analytically solvable topologically ordered states, e.g. the Levin-Wen model and the Kitaev quantum double model, it is known that the WLOs can be efficiently expressed by MPOs with a

support region R with small thickness t and bond dimension χ [52, 53, 125].

To extract the closed WLOs using the MPO ansatz, we numerically optimize the MPO ansatz in order to obtain a $W_a(\gamma)$ which approximately satisfies Eq. (1.6). In order to efficiently optimize a Wilson loop, we note that for Abelian topological orders, *an operator W and a wave function $|\psi\rangle$ satisfies Eq.* (1.6) *if and only if*

$$\langle\psi|W|\psi\rangle = 1, \tag{4.1}$$

$$\langle\psi|W^\dagger W|\psi\rangle = 1. \tag{4.2}$$

The forward proof is trivial. For the backward proof, we assume that W and $|\psi\rangle$ satisfy Eqs. (4.1) and (4.2) and without loss of generality, $W|\psi\rangle = a|\psi\rangle + b|\psi_\perp\rangle$, where a and b are complex numbers and $\langle\psi|\psi_\perp\rangle = 0$. Solving Eqs. (4.1) and (4.2) we can obtain $a = 1$ and $b = 0$. Note that Eq. (11) implies that $a = 1$ and Eq. (12) ensures that $W|\psi\rangle$ is normalized to 1, which then requires $b = 0$.

Therefore, we can define the cost function for a wave function $|\psi\rangle$ as

$$\mathcal{C}(W) = [\langle\psi|W|\psi\rangle - 1]^2 + [\langle\psi|W^\dagger W|\psi\rangle - 1]^2. \tag{4.3}$$

It reaches a global minimum $\mathcal{C}(W) = 0$ only when W is an exact Wilson loop operator.

To variationally optimize the WLO, we start by initializing a random MPO with fixed (R, χ). Each tensor in the MPO is initialized randomly and independently from each other. For a translationally invariant system, one may naively expect that a translation symmetric closed WLO is a better ansatz. However, we found that the translation symmetric ansatz tends to be

unstable numerically, leading to diverging or vanishing gradients in the optimization procedure.

After the initialization, we minimize the cost function defined in Eq. (4.3) through gradient based optimization. In this work, we apply the Adam algorithm [126] to minimize the cost function. In this work, we fix the hypermeters of the Adam algorithm as $\beta_1 = 0.9, \beta_2 = 0.999$ and learning rate 10^{-3}. We iterate the optimization procedure until the cost function converges, which typically takes a few hundred to a few thousand iterations.

We repeat the initialization and minimization N_{sample} times to obtain N_{sample} optimized WLOs W_k, where $1 \leq k \leq N_{\text{sample}}$. Throughout the manuscript, we fix $N_{\text{sample}} = 20$. We then measure the braiding phases and topological twists to classify the WLOs through the equivalence relation described as follows : we compute the mutual-braiding phases between W_i and W_j, $\phi_{i,j}$, where $1 \leq i, j \leq N_{\text{sample}}$ and topological twist for W_i θ_i, where $1 \leq i \leq N_{\text{sample}}$. We say the two WLOs W_i and W_j are equivalent when $\phi_{i,k} = \phi_{j,k}$ for $1 \leq k \leq N_{\text{sample}}$, and $\theta_i = \theta_j$. After grouping the WLOs into equivalence classes, we randomly pick one representative WLO from each equivalent class.

This equivalence relation assumes that if two WLOs have the same braiding phase with the rest of the WLOs and identical topological twists, the two WLOs are equivalent. We note that this condition only holds when we obtain a complete set of WLOs in our optimization procedure. Missing one could result in a false classification. However, one can verify whether a complete set of WLOs is found by checking if the resulting S matrix is a unitary matrix. If one or more WLOs are missing, we can vary the hyper-parameters such as increasing the thickness of the WLOs or the bond dimension χ.

The bottleneck of the numerical optimization is in the tensor contraction when calculating the expectation values $\langle\psi|W|\psi\rangle$ and $\langle\psi|W^\dagger W|\psi\rangle$. Here, we briefly describe the tensor contraction

scheme and its computational time complexity. Given a ground state wave function $|\psi\rangle$, represented by an infinite projective entangled pair state (iPEPS) [127, 128, 129] as shown in Fig. 4.2 , we use the following procedure to evaluate the expectation value $\langle\psi|W|\psi\rangle$. Consider a closed WLO that takes the form of a rectangular loop with side lengths L_x and L_y as shown in Fig. 4.2, for a system on a square lattice. We first contract all tensors at $x = 0$ to form a tensor M with L_y bonds as shown in Fig. 4.2. We then contract the tensors at $x = 1$ with M one by one from $y = 0$ to $y = L_y + 1$. We then repeat this procedure for all $x \leq L_x + 1$. In this contraction procedure, the computational cost for contracting the tensors scales linearly with the number of sites along the x direction (L_x) and exponentially with number of sites along the y direction (L_y). Therefore, the total computational cost is bounded by $O(L_x L_y \chi^{L_y+5})$. Moreover, since the thickness t and the size of the hole need to be much larger than the correlation length, we have that $L_x, L_y > 3\xi$. Thus the total computational cost for calculating the expectation value scales up as $O(\xi^2 \chi^{\alpha\xi})$ for some constant $\alpha \gg 1$. Therefore, this method is particularly suitable for models with small correlation length. Importantly, the complexity of the computation scales with the correlation length, not the total system size.

4.3 Manipulation of anyons

Once we have obtained the closed WLOs, we can extract many non-trivial properties of the anyons. In particular, we can further obtain operators that create, move, and annihilate anyons.

In the following, we discuss how to manipulate anyons by starting from the closed WLOs. For simplicity in this section, we assume that the thickness of WLOs is $t = 1$. The idea can be easily generalized to $t > 1$ as is the case for our numerical results in Section 4.4.

4.3.1 Removing and adding a virtual bond

Before we proceed to the manipulation of anyons, we first define two basic operations of a tensor A, which is that of removing and adding a virtual bond. These two operations will be extensively used throughout this section.

Removing a virtual bond is useful for cutting open closed WLOs. To remove a virtual bond in a tensor $A_{\alpha,\beta,\ldots,\gamma}$, we define an edge tensor E_α that describes the boundary condition and contract the edge tensor E_α with $A_{\alpha,\beta,\ldots,\gamma}$; the resulting tensor is

$$A'_{\beta,\ldots,\gamma} = \sum_\alpha E_\alpha A_{\alpha,\beta,\ldots,\gamma}, \tag{4.4}$$

and it has rank $n-1$.

Adding a virtual bond is useful when extending an open WLO or connecting two open WLOs. To add a trivial virtual bond to an arbitrary tensor $A_{\alpha,\beta,\ldots,\gamma}$ with rank n, we define a new tensor $\tilde{A}$ with rank $n+1$ as

$$\tilde{A}_{\alpha',\alpha,\beta,\ldots,\gamma} = A_{\alpha,\beta,\ldots,\gamma}, \tag{4.5}$$

for all $1 \leq \alpha' \leq \chi$, where χ is the bond dimension of the new virtual bond.

Using the above two basic operations on tensors, we can create, move and annihilate anyons, as described in the following sections.

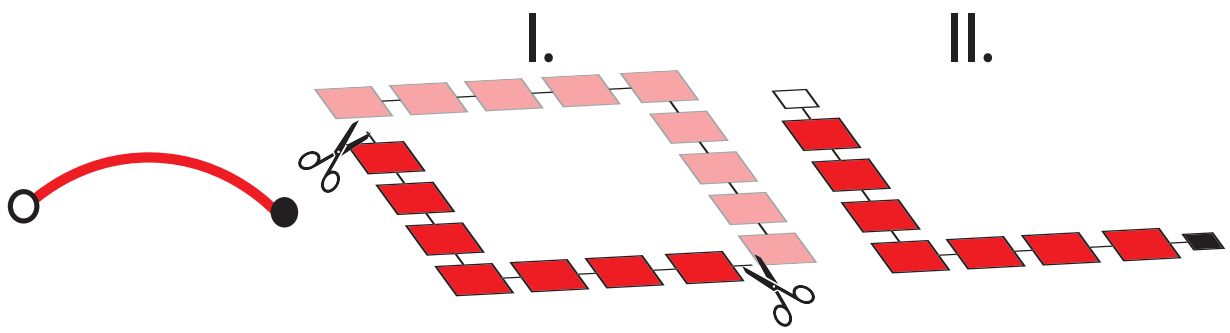

Figure 4.3: **Creation of an anyon and anti-anyon pair. Step I** : We truncate a closed WLO by discarding a segment of it. **Step II** : We contract two two boundary tensor with edge tensor to terminate the open WLO.

4.3.2 Creation of anyon and anti-anyon pairs

To create an anyon and anti-anyon pair, we simply discard a segment of the closed WLO and apply an arbitrary edge tensor to terminate its boundary as shown in Fig. 4.3. Specifically, we start with a closed WLO obtained using the procedure described in Sec. 4.2 for a give ground state wave function $|\psi\rangle$, which is of the form

$$W = \sum_{\{\alpha\}} A^1_{\alpha_0,\alpha_1} A^2_{\alpha_1,\alpha_2} \cdots A^{L-1}_{\alpha_{L-2},\alpha_{L-1}} A^L_{\alpha_{L-1},\alpha_0}, \tag{4.6}$$

where L is the length of the closed WLO.

We then keep the tensors from sites $1, \cdots, l$, as shown in step I of Fig. 4.3, so that the new MPO is of the form

$$\tilde{W}_{\beta,\beta'} = \sum_{\{\alpha\}} A^1_{\beta,\alpha_1} A^2_{\alpha_1,\alpha_2} \cdots A^{l-1}_{\alpha_{l-2},\alpha_{l-1}} A^l_{\alpha_{l-1},\beta'}. \tag{4.7}$$

We then remove the virtual indices β and β' $\tilde{W}_{\beta,\beta'}$ by applying the edge tensor E. The

edge tensors can be chosen arbitrarily, since different choices are related to each other by a local operator. Throughout out this article, we use

$$E_\gamma = \begin{cases} 1, & \text{if } \gamma = 1 \\ 0, & \text{otherwise} \end{cases}. \tag{4.8}$$

After removing the edge virtual bond shown in step II in Fig. 4.3, the open WLO is of the form

$$W^{\text{open}} = \sum_{\beta,\beta'} \tilde{W}_{\beta,\beta'} E_\beta E_{\beta'}. \tag{4.9}$$

When another WLO passes through the open WLO, the system acquires an anyonic braiding phase as long as the crossing point is away from the boundary of the open WLO by an $O(\xi)$.

Finally, in order to preserve the norm of the wave function, we normalize the open WLO defined above by a factor $\sqrt{\langle\psi|W^{\text{open}\dagger}W^{\text{open}}|\psi\rangle}$.

4.3.3 Moving anyons

Let us imagine we have a WLO $W^{\text{open}}_{x_1,x_2}$ that creates an anyon a at one endpoint x_1 and its conjugate $\overline{a}$ at the other endpoint x_2. We can use this to construct a different operator $W^{\text{open}}_{x_1',x_2}$, effectively moving a from x_1 to x_1'. We can do this as follows.

We start with an open WLO as shown in step I of Fig. 4.4. The open WLO with length L

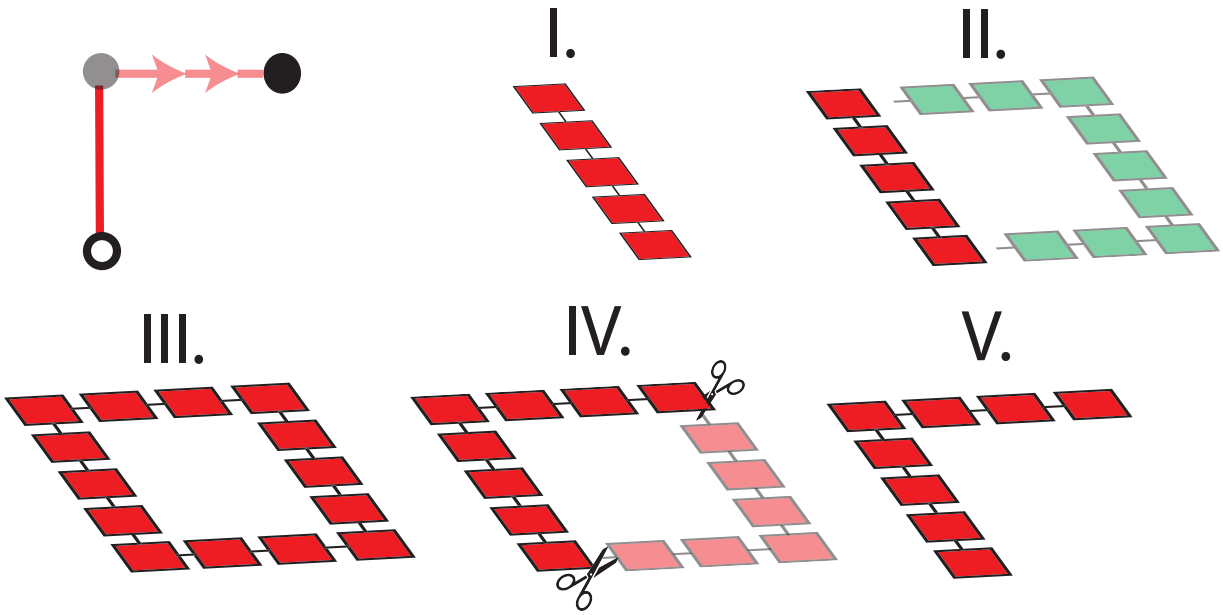

Figure 4.4: **Moving anyons. Step I** : We start with an open WLO that can be generated using the method described in Sec. 4.3.2. **Step II** : We randomly initialize an open MPO with virtual bond at the boundary tensors. The initialized open MPO and the open WLO form a closed MPO. **Step III**: We vary the closed MPO to minimize the cost function defined in Eq. (4.3). **Step IV and V** Finally, we cut the closed WLO to create two excitations that can be located at different sites from the anyons in Step I.

is of the form

$$W^{\text{open}} = \sum_{\{\alpha\}} A^1_{\alpha_1} A^2_{\alpha_1,\alpha_2} \cdots A^{L-1}_{\alpha_{L-2},\alpha_{L-1}} A^L_{\alpha_{L-1}}. \tag{4.10}$$

The open WLO can be obtained using the procedure described in Sec. 4.3.2.

We initialize another random MPO with length L' that is a loop complement of the WLO W^{open} as shown in step II of Fig. 4.4 and is of the form

$$W^{\text{open}}_C = \sum_{\{\beta\}} C^1_{\beta_1} C^2_{\beta_1,\beta_2} \cdots C^{L'-1}_{\beta_{L'-2},\beta_{L'-1}} C^{L'}_{\beta_{L'-1}}, \tag{4.11}$$

To connect W^{open} and W^{open}_P at the boundary, we add a trivial virtual bond on each

boundary tensor. By adding trivial virtual bond on all the boundary tensors $A^1, A^L, C^1, C^{L'}$, we have

$$\begin{aligned}\tilde{W}^{\text{open}}_{\gamma_0,\gamma_L} &= \sum_{\{\alpha\}} \tilde{A}^1_{\gamma_0,\alpha_1} A^2_{\alpha_1,\alpha_2} \cdots A^{L-1}_{\alpha_{L-2},\alpha_{L-1}} \tilde{A}^L_{\alpha_{L-1},\gamma_L}, \\ \tilde{W}^{\text{open}}_{C,\mu_0,\mu_{L'}} &= \sum_{\{\beta\}} \tilde{C}^1_{\mu_0,\beta_1} C^2_{\beta_1,\beta_2} \cdots C^{L'-1}_{\beta_{L'-2},\beta_{L'-1}} \tilde{C}^{L'}_{\beta_{L'-1},\mu_{L'}}.\end{aligned} \tag{4.12}$$

We can therefore have a closed WLO of the form

$$W = \sum_{\gamma_0,\gamma_L,\mu_0,\mu_{L'}} \tilde{W}^{\text{open}}_{\gamma_0,\gamma_L} \tilde{W}^{\text{open}}_{C,\mu_0,\mu_{L'}} \delta_{\gamma_0,\mu_{L'}} \delta_{\gamma_L,\mu_0}, \tag{4.13}$$

where $\delta_{i,j}$ is a Kronecker delta function.

In step III of Fig. 4.4, we minimize the cost function of Eq. (4.3) for the closed WLO defined above. We note that in addition to vary the tensors in the $\tilde{W}^{\text{open}}_{C,\mu_0,\mu_{L'}}$, we also have to vary tensors at the boundary of $\tilde{W}^{\text{open}}_{\gamma_0,\gamma_L}$ i.e. $\tilde{A}^1$, $\tilde{A}^L$,...etc. in order to eliminate the anyon excitation at the boundary.

We define a length parameter b, which is of order $O(\xi)$. In the optimization procedure, we vary all the tensors Cs and $\tilde{C}$s in W^{open}_C and the boundary tensor of W^{open}, $\tilde{A}^1$, A^2, ..., A^b and A^{L-b+1}, $\cdots$ A^{L-1}, $\tilde{A}^L$, while fixing the tensors A^i for $b+1 \leq i \leq L-b+1$.

Once we find the optimal solution that approximately satisfies Eq. (1.6), we can cut the closed WLO to create two ends as described in Sec. 4.3.2 and effectively move the anyon as shown in step IV and V in Fig. 4.4.

4.3.4 Annihilation of anyon and anti-anyon pairs

In this section, we describe a procedure to fuse an anyon and anti-anyon pair to identity. Given two open WLOs $W_a(\gamma)$ and $W_a(\gamma')$, we show how to join them into a single WLO, as shown in Fig. 4.5, by effectively bringing together two endpoints of γ and γ' and annihilating the anyons.

We consider two open WLOs of the form

$$\begin{aligned} W_1^{\text{open}} &= \sum_{\{\alpha\}} A^1_{\alpha_1} A^2_{\alpha_1,\alpha_2} \cdots A^{L_1-1}_{\alpha_{L_1-2},\alpha_{L_1-1}} A^{L_1}_{\alpha_{L_1-1}}, \\ W_2^{\text{open}} &= \sum_{\{\beta\}} B^1_{\beta_1} B^2_{\beta_1,\beta_2} \cdots B^{L_2-1}_{\beta_{L_2-2},\beta_{L_2-1}} B^{L_2}_{\beta_{L_2-1}}. \end{aligned} \tag{4.14}$$

For simplicity we assume that the tensors A^{L_1-1} and B^1 are located at nearest-neighbor sites as shown in step I of Fig. 4.4. If this is not the case, we can move the end of W_2^{open} using the procedure described in Sec. 4.3.3.

We then initialize a random MPO with length L' that is a loop complement of W_1^{open} and W_2^{open}, which takes the form

$$W_C^{\text{open}} = \sum_{\{\gamma\}} C^1_{\gamma_1} C^2_{\gamma_1,\gamma_2} \cdots C^{L'-1}_{\gamma_{L'-2},\gamma_{L'-1}} C^{L'}_{\gamma_{L'-1}}. \tag{4.15}$$

We can connect the three open WLOs by adding a trivial virtual bond on each boundary

tensor as in step III of Fig. 4.5. After adding a virtual bond, the WLOs become

$$\begin{aligned}
\tilde{W}^{\text{open}}_{1,\mu_0,\mu_L} &= \sum_{\{\alpha\}} \tilde{A}^{1}_{\mu_0,\alpha_1} A^{2}_{\alpha_1,\alpha_2} \cdots A^{L_1-1}_{\alpha_{L_1-2},\alpha_{L_1-1}} \tilde{A}^{L_1}_{\alpha_{L_1-1},\mu_{L_1}}, \\
\tilde{W}^{\text{open}}_{2,\nu_0,\nu_L} &= \sum_{\{\beta\}} \tilde{B}^{1}_{\nu_0,\beta_1} B^{2}_{\beta_1,\beta_2} \cdots B^{L_2-1}_{\beta_{L_2-2},\beta_{L_2-1}} \tilde{B}^{L_2}_{\beta_{L_2-1},\nu_{L_2}}, \\
\tilde{W}^{\text{open}}_{C,\sigma_0,\sigma_L} &= \sum_{\{\gamma\}} \tilde{C}^{1}_{\sigma_0,\gamma_1} C^{2}_{\gamma_1,\gamma_2} \cdots C^{L'-1}_{\gamma_{L'-2},\gamma_{L'-1}} \tilde{C}^{L'}_{\gamma_{L'-1},\sigma_{L'}}.
\end{aligned} \tag{4.16}$$

We can therefore connect the three WLO and have a closed MPO of the form

$$\begin{aligned}
W = \sum_{\mu_0,\mu_{L_1},\nu_0,\nu_{L_2},\sigma_0,\sigma_{L'}} & \tilde{W}^{\text{open}}_{1,\mu_0,\mu_{L_1}} \tilde{W}^{\text{open}}_{2,\nu_0,\nu_{L_2}} \tilde{W}^{\text{open}}_{C,\sigma_0,\sigma_L} \\
& \times \delta_{\mu_{L_1},\nu_0} \delta_{\nu_{L_2},\sigma_0} \delta_{\sigma_{L'},\mu_0}.
\end{aligned} \tag{4.17}$$

To minimize the cost in Eq. (4.3) for the WLO above, we vary the MPO above except for the tensors $A^{i}_{\alpha_{i-1},\alpha_i}$, $B^{i}_{\beta_{i-1},\beta_i}$, where $b \leq i \leq L_1 - b$. After obtaining a closed WLO as shown in step III of Fig. 4.5, we cut the WLO at the support of W^{open}_{C} using the procedure described in Sec. 4.3.2. The resulting open WLO is the fusion of W^{open}_{1} and W^{open}_{2}.

4.3.5 Topological twist (exchange statistics)

Here we present the scheme that we use to extract the topological twists of the anyons. To calculate the topological twists, we calculate the ratio of the amplitude for the following two processes. In the first process (P_1), we create an anyon and anti-anyon pair from the ground state wave function. We then exchange them, and finally, we annihilate the pair of anyon and anti-anyon. In the second process (P_2), we create and annihilate the pair directly without any exchange

For the first process, we start with a closed WLO with length L_o of the form

$$W = \sum_{\{\alpha\}} A^1_{\alpha_0,\alpha_1} A^2_{\alpha_1,\alpha_2} \cdots A^{L_o-1}_{\alpha_{L_o-2},\alpha_{L_o-1}} A^{L_o}_{\alpha_{L_o-1},\alpha_0}. \tag{4.18}$$

We then cut the closed WLO and keep two segments with length l as shown in step I of Fig. 4.6. These segments represent a creation of an anyon and anti-anyon. The end of the two segments of the WLOs are away from each other by distance b which is an integer larger than $O(\xi)$.

The WLOs are of the form

$$\begin{aligned} W_1^{\text{open}} &= \sum_{\{\alpha\}} A^1_{\alpha_1} A^2_{\alpha_1,\alpha_2} \cdots A^{l-1}_{\alpha_{l-2},\alpha_{l-1}} A^l_{\alpha_{l-1}}, \\ W_2^{\text{open}} &= \sum_{\{\alpha\}} A^{b+1}_{\alpha_{b+1}} A^{b+2}_{\alpha_{b+1},\alpha_{b+2}} \cdots A^{b+l-1}_{\alpha_{b+l-2},\alpha_{b+l-1}} A^{b+l}_{\alpha_{b+l-1}}. \end{aligned} \tag{4.19}$$

In Step II, we flip the direction of the anyon transport for the WLO W_2^{open} by applying Hermitian conjugation.

After cutting and flipping the WLO, we move the anyon located at the open ends i and n to sites m and j respectively, as shown in step III of Fig. 4.6. We then connect the WLOs by annihilating anyon and anti-anyon pairs in step IV of Fig. 4.6. The WLO becomes a self-intersecting closed loop of the form

$$W_{P_1}^{\text{twist}} = \sum_{\{\beta\}} B^1_{\beta_0,\beta_1} B^2_{\beta_1,\beta_2} \cdots B^{L-1}_{\beta_{L-2},\beta_{L-1}} B^L_{\beta_L,\beta_0}, \tag{4.20}$$

where L is the path length of the closed WLO $W_{P_1}^{\text{twist}}$. The labels for the supports are shown in Fig. 4.6. Finally, we contract the physical indices in the self-intersecting region as shown in step V of Fig. 4.6.

In step I of process P_1, we cut and discard two segments of a closed WLO as described in Eq. (4.19). This step explicitly breaks the gauge symmetry of a matrix product operator, which introduces non-universal complex phases to W_1^{open} and W_2^{open}. The non-universal complex phase depends on the details of the implementation. In order to cancel the non-universal complex phase, we calculate the amplitude of the second process P_2 using the same tensors in Eq. (4.20), but we contract the tensors without exchanging anyons. We conjecture and numerically verify that the process P_2 has the same non-universal complex phase as the process P_1. The calculation of process P_2 can be achieved by rotating the right half of the support of $W_{P_1}^{\text{twist}}$ around the center of self-intersecting region and stacking it on top of the left half of the support as shown in Fig. 4.7(a). Instead of creating, exchanging and annihilating the anyon and anti-anyon pair, this process creates an anyon and anti-anyon pair and the anyon travels around the left half of the support twice. And subsequently it is annihilated with the anti-anyon. We note that in order to perform the rotation, presumably the ground state wave function must have rotation symmetry around the center of the self-intersecting region and translation symmetry. We have not systematically studied how the above procedure would need to be modified if the translation and rotation symmetries of the system are broken.

The WLO after the rotation is of the following form

$$W_{P2}^{\text{twist}} = \sum_{\{\beta\}} C_{\beta_1,\beta_{\frac{L}{2}-1},\beta_{\frac{L}{2}+1},\beta_{L-1}} \prod_{i=2}^{\frac{L}{2}} D^i_{\beta_{i-1},\beta_{L-i+1},\beta_i,\beta_{L-i}} \tag{4.21}$$

where

$$
\begin{aligned}
C_{\beta_1,\beta_{\frac{L}{2}-1},\beta_{\frac{L}{2}+1},\beta_{L-1}} &= \sum_{\beta_0,\beta_{\frac{L}{2}}} B^{1}_{\beta_0,\beta_1} * B^{\frac{L}{2}}_{\beta_{\frac{L}{2}-1},\beta_{\frac{L}{2}}} \\
&* \quad B^{\frac{L}{2}+1}_{\beta_{\frac{L}{2}},\beta_{\frac{L}{2}+1}} * B^{L}_{\beta_L,\beta_0}, \\
D^{i}_{\beta_{i-1},\beta_{L-i+1},\beta_i,\beta_{L-i}} &= B^{i}_{\beta_{i-1},\beta_i} * B^{L-i+1}_{\beta_{L-i},\beta_{L-i+1}}
\end{aligned}
\tag{4.22}
$$

and the tensor multiplication $*$ denotes the contraction of physical indices as shown in Fig. 4.7(b).

Therefore, the topological twist that represents the exchange statistics is calculated from the ratio of the expectation value of $W_{P_1}^{\text{twist}}$ and $W_{P_2}^{\text{twist}}$,

$$
\tilde{T}_a = \frac{\langle\psi|W_{P_1;a}^{\text{twist}}|\psi\rangle}{\langle\psi|W_{P_2;a}^{\text{twist}}|\psi\rangle}, \tag{4.23}
$$

where the label a denotes the anyon type.

4.4 Numerical results

In this section, we present the numerical results for extracting WLOs and braiding statistics for various systems.

4.4.1 Z_2 toric code model in a magnetic field

We first consider the Z_2 toric code model in a magnetic (Zeeman) field [130, 131, 132, 133, 134]. The Hamiltonian is of the form

$$H_{\mathrm{TC}} = -\sum_{p\in\mathrm{plaquette}} B_p - \sum_{v\in\mathrm{vertex}} A_v - \sum_i (h_x X_i + h_z Z_i), \tag{4.24}$$

where the plaquette operators $B_p = \prod_{i\in p} Z_i$, the vertex operators $A_v = \prod_{i\in v} X_i$ and h_x and h_z are the magnetic fields along the x and z directions respectively.

In the following, we consider a dual lattice, so that the spins are on the lattice sites instead of the bonds. The plaquette operators A_p and the vertice operators B_v of the toric code model are then on alternating plaquettes, as depicted in gray and white respectively in Fig. 4.8 (a).

When the magnetic fields $h_x = h_z = 0$, the ground state of the toric code model can be solved analytically. The ground state has zero correlation length and the Wilson loop operators can be solved exactly (cost $\mathcal{C} = 0$) with bond dimension $\chi = 1$ and thickness $t = 1$ for any size of the closed WLOs L_x and L_y.

There exist four distinct Wilson loop operators for the anyon types : I, e, m and ψ, where I is the identity sector, e and m are bosons with trivial self-braiding phase and a π mutual-braiding phase and $\psi = e \times m$ is the fermion. The modular S matrix characterizing the mutual braiding

statistics, listing the anyons in the order I, e, m, ψ is of the form,

$$S = \frac{1}{2}\begin{pmatrix} 1 & 1 & 1 & 1 \\ 1 & 1 & -1 & -1 \\ 1 & -1 & 1 & -1 \\ 1 & -1 & -1 & 1 \end{pmatrix}. \tag{4.25}$$

The topological twists, which characterize the exchange statistics of the anyons, is given by

$$T = diag(1, 1, 1, -1). \tag{4.26}$$

Figure 4.8 (b) and (c) illustrate the measurement of modular S and T matrices with thickness $t = 1$ on 2D square lattice.

With non-zero magnetic fields, the ground state wave function has a finite correlation length ξ. The Wilson loop operators with finite thickness t can no longer represent the exact WLOs. However, the optimization scheme can still find approximate WLOs with error of order $\mathcal{O}(N_s e^{-t/\xi})$, where N_s is the number of sites.

We first obtain the ground state wave function by minimizing the infinite projective entangled pair state (iPEPS) using a recently proposed differential programming approach [128, 129] with corner transfer matrix renormalization group (CTMRG) [127].

Next, we follow the protocol described in Sec. 4.2, minimizing the cost function defined in Eq. (4.3) starting from random MPO initializations, to find the Wilson loop operators. Figure 4.8(d) shows the minimum cost as a function of h_x with a fixed $h_z = 0.05$ for thickness $t = 1$ and $t = 2$. The cost decreases when the thickess t increases, demonstrating that a larger thickness

gives a better approximation to the true Wilson loop operator.

In Fig. 4.8(e), we compare the optimized closed WLOs to the WLOs known for the fixed point toric code Hamiltonian ($h_x = h_z = 0$). The expectation values of the optimized closed WLOs stay close to 1 as the magnetic field is increased. However, the expectation values of the fixed point WLOs decrease with increasing h_x. We note that this is remarkable given that we do not use prior knowldge of the WLOs of the fixed point Hamiltonian; our scheme is completely unbiased and uses no prior information aside from the ground state of the perturbed Hamiltonian whose WLOs we are trying to find.

While we do not know the form of the exact WLOs in the presence of non-zero h_x, h_z, we do know that their expectation value in the ground state is 1. Therefore, we can compute how close our optimized WLOs are to the exact WLOs. We define the error

$$\epsilon = |\langle\psi|W - W_{\text{exact}}|\psi\rangle|, \tag{4.27}$$

where we use the fact that the exact WLO, W_{exact}, satisfies $\langle W_{\text{exact}}\rangle = 1$. Here W represents a WLO found through our optimization protocol.

We present the error ϵ of the WLOs as a function of the inverse of the correlation length $1/\xi$ and number of sites N_s in Fig. 4.8(f) and (g), respectively The correlation length is computed by through the exponential decay of the correlation funcion, $\langle X_{x_0,y_0}X_{x_0+d,y_0}\rangle - \langle X_{x_0,y_0}\rangle\langle X_{x_0+d,y_0}\rangle = Ae^{-d/\xi}$. The largest correlation length we reach in our simulation is $\xi = 1.21$.

In Fig. 4.8(f), we vary the correlation length by varying the magnetic field h_x. We show that the error drops exponentially as function of $1/\xi$. Fig. 4.8 (g) shows how the error ϵ scales with the number of sites N_s in the support of the WLO with $t = 1$, indicating that the error scales

up linearly with N_s. Therefore the error scaling is consistent with the error bound $\mathcal{O}(N_s e^{-t/\xi})$ [40].

Finally, we numerically evaluate the twist product matrix $\tilde{S}_{i,j}$ and the topological twist $\tilde{T}_i$. The twist product matrix is consistent with Eq. (4.25) up to 10^{-5} error and the topological twist has error up to 10^{-2}. For example, the twist product matrix for $h_x = 0.1$, $h_z = 0.05$, $t = 2$, $L_x = 6$, $L_y = 4$, $\chi = 1$ is

$$\tilde{S} = \begin{pmatrix} 1.0 & 1.0 & 1.0 & 1.0 \\ 1.0 & 1.0 & -1.00001 & -0.99996 \\ 1.0 & -0.99999 & 1.0 & -0.99977 \\ 1.0 & -1.00004 & -1.00024 & 1.0 \end{pmatrix}, \tag{4.28}$$

and

$$\tilde{T} = diag(1.0, 0.963, 0.912, -0.974). \tag{4.29}$$

4.4.2 Double semion model

In this section, we present our numerical results for the double semion model.

The Hamiltonian of the double semion model [53], which we take to be on the honeycomb lattice, is of the form

$$\begin{aligned} H_{DS} &= -\sum_{v \in vert.} A_v - \sum_i h_x X_i, \\ &+ \left(\sum_{p \in plaq.} B_p \prod_{j \in \text{legs(p)}} i^{\frac{1-X_j}{2}} + h.c.\right) \end{aligned} \tag{4.30}$$

where the plaquette operators $B_p = \prod_{i \in p} Z_i$, the vertex operators $A_v = \prod_{i \in v} X_i$ and legs(p) is the legs of plaquette p as shown in Fig. 4.9(a).

For $h_x = 0$, the ground state and the Wilson loop operators can be obtained analytically [53]. There exists four distinct WLOs denoted by I, s, s', $b = s \times s'$, which represent identity, right and left-handed semions and a boson. The two semions have π self-braiding statistics and trivial mutual braiding statistics. The modular S matrix, listing the anyons in the order I, s, s', b, is of the form

$$S = \frac{1}{2} \begin{pmatrix} 1 & 1 & 1 & 1 \\ 1 & -1 & 1 & -1 \\ 1 & 1 & -1 & -1 \\ 1 & -1 & -1 & 1 \end{pmatrix}. \tag{4.31}$$

The topological twists that characterize the exchnage statistics of the double semion model is given by

$$T = diag(1, i, -i, 1). \tag{4.32}$$

The exact closed WLOs for $h_x = 0$ are of the form

$$\begin{aligned} W_I &= I, \\ W_s &= \prod_{l\in\gamma} Z_l \prod_{k\in \text{L}-\text{vertex}} (-1)^{\frac{1}{4}(1-X_i)(1+X_j)} \prod_{l\in \text{R}-\text{leg}} i^{\frac{1}{2}(1-X_l)} \\ W_{s'} &= \prod_{l\in\gamma} Z_l \prod_{k\in \text{L}-\text{vertex}} (-1)^{\frac{1}{4}(1-X_i)(1+X_j)} \prod_{l\in \text{R}-\text{leg}} (-i)^{\frac{1}{2}(1-X_l)} \\ W_b &= \prod_{l\in\gamma'} X_l, \end{aligned} \tag{4.33}$$

where γ is a path of a closed WLO, γ' is a path of a closed WLO on the duel lattice, i and j are two legs attached to L-vertex k as shown in Fig. 4.9(b).

Note that the W_s and $W_{s'}$ operators above have thickness $t = 2$ and bond dimension $\chi = 1$. Interestingly, using our unbiased numerical optimization, we found an equivalent way to represent the exact WLOs at the fixed point with $t = 1$ and $\chi = 2$. We present its analytical form in Appendix **??**.

In order to numerically optimize the WLOs, we numerically optimize the iPEPS ground state wave function [135] and consider WLOs with thickness $t = 1$ and $t = 2$ as shown in Fig. 4.9(c) and 4.9(d) respectively. Fig. 4.9(e) shows the minimum cost achieved as a function of the magnetic field h_x. The optimizer converges to these minimum costs after roughly 1000 iterations. Fig. 4.9(f) shows the minimum cost as a function of the bond dimension χ for the two semions for $h_x = 0.1$ and $t = 1$.

We then numerically evaluate the twist product matrix $\tilde{S}_{i,j}$ and the topological twist $\tilde{T}_i$. The support of $\tilde{S}$ and $\tilde{T}$ are shown in Fig. 4.10(a) and (b) respectively. The twist product matrix is consistent with Eq. (4.31) up to 10^{-4} error and the topological twist has error up to 10^{-2}. For

example, the twist product matrix for $h_x = 0.1$, $t = 1$, $\chi = 2$ is

$$\tilde{S} = \begin{pmatrix} 1.0 & 1.0 & 1.0 & 1.0 \\ 1.0 & -1.0 & 1.001 & -0.994 \\ 1.0 & 0.999 & -1.0 & -1.002 \\ 1.0 & -1.006 & -0.998 & 1.0 \end{pmatrix}, \tag{4.34}$$

and

$$\tilde{T} = \mathrm{diag}(1.0, 0.9351e^{i\pi 0.502}, 0.9412e^{-i\pi 0.489}, 0.993). \tag{4.35}$$

The correlation length of the ground state, calculated through the exponential decay of the correlation funcion, $\langle X_{x_0,y_0} X_{x_0+d,y_0}\rangle - \langle X_{x_0,y_0}\rangle\langle X_{x_0+d,y_0}\rangle$, with $h_x = 0.1$ is $\xi = 0.87$.

4.5 Summary and outlook

In conclusion, we propose a numerical optimization-based scheme to extract Wilson loop operators of anyons from a single ground state wave function defined on a simply connected region of space. We show how, after extracting closed loop operators, one can then modify them to obtain Wilson line operators that create, move, and annihilate anyons. This allows us to ultimately extract the braiding statistics and topological twists of the anyons from a single bulk ground state wave function. While our protocol for extracting the modular S matrix is expected to be general, our protocol for extracting the topological twists may be benefiting from the lattice symmetries of our models; we leave a systematic investigation of this for future work.

Our algorithm fully succeeds only when all distinct equivalence classes of Wilson loop

operators have been found. We expect that in general, for a large enough bond dimension, all Wilson loop operators can be captured by our matrix product operator ansatz. In practice it may be the case that some Wilson loop operators might be more complicated than others, in the sense of having higher operator entanglement or requiring larger bond dimension. In this case, if there is an implicit bias of the optimization procedure towards the simpler loop operators, then the algorithm may never succeed in discovering a complete set of loop operators starting from random initialization. In this case, further work needs to be done on either finding improved initializations or modifying the optimization procedure to remove the implicit biases.

Our work also raises an interesting question of whether all Wilson loop operators for anyons can always be described by an MPO with finite bond dimension. This is particularly intriguing to study for chiral topological orders, such as fractional quantum Hall states, where loop operators have never been explicitly computed in MPO form and the ground state wave functions cannot be described by a PEPS with finite bond dimension.

So far, our optimization scheme is tailored to Abelian topological orders. It would be interesting to generalize it to the case of non-abelian topologically ordered phases, which can have anyons with quantum dimension greater than one. One possible direction is to design an optimization scheme to extract both the WLOs and the quantum dimension of anyons simultaneously.

As we discussed, the Wilson line operators can be generalized to more generic movement and splitting operators. If we discover such generic movement and splitting operators through a similar optimization approach to what we have described, it may also be possible to extract the F and R symbols of the underlying modular tensor category using the results of Ref. [51].

Looking further, similar optimization procedures applied to symmetry defect creation and movement operators may eventually allow us to extract the full G-crossed braided tensor category

[22] that describes a given symmetry-enriched topological ground state. This would allow the extraction of all possible topological invariants from a single bulk ground state wave function.

More broadly, recent developments in quantum simulators allow the realization of topologically ordered states that might not occur in conventional electronic matter [118, 119]. Given this opportunity, it is intriguing to develop measurement protocols for probing topological properties of a ground state wave function associated with a prior unknown gapped Hamiltonian. Our optimization protocol may be particularly relevant in this context. Since our scheme requires measuring several observables for a given wave function, it may be useful when combined with shadow tomography. [96].

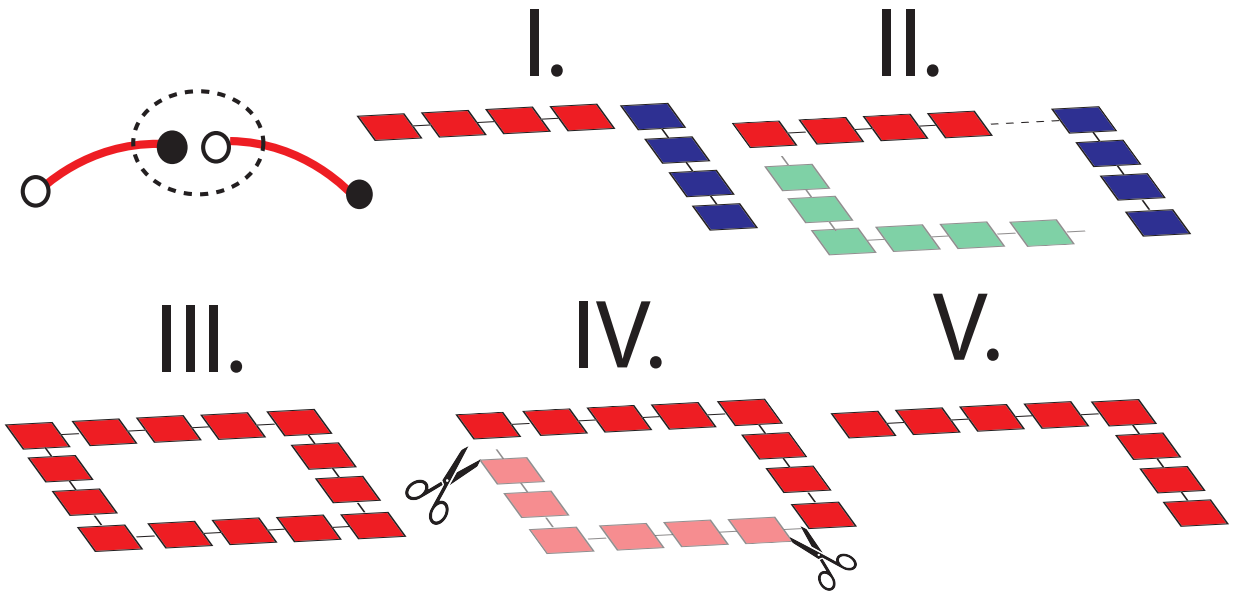

Figure 4.5: **Annihilation of anyon and anti-anyon pairs Step I**: We start with two open WLOs The boundary of the two open WLOs are at nearest neighbor sites. **Step II**: We randomly initialize an open MPO with virtual bonds at the boundary tensors. The two open WLOs and the MPO form a closed MPO. **Step III**: We vary the closed MPO to minimize the cost function defined in Eq. (4.3). **Step IV and V** : Finally, we cut the closed WLO and keep the tensors on supports of the two open WLOs in Step I.

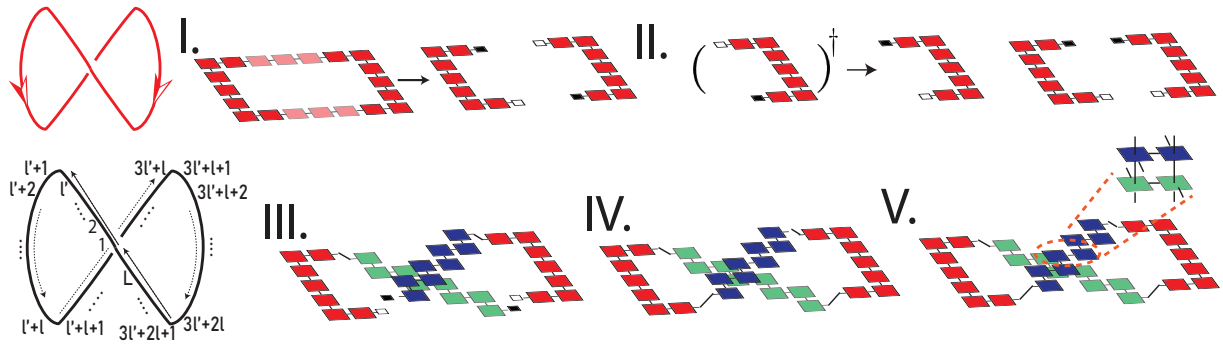

Figure 4.6: **Topological twist. Step I.** We cut a closed WLO and keep two open WLO. **Step II.** We flip the right open WLO to reverse the direction of the anyon and anti-anyon. The boundary sites are denoted as i, j, m and n. **Step III.** We move the anyons at i and n to m and j respectively. **Step IV.** We connect the WLO to form a closed loop. **Step V.** Finally, we contract the physical indices in the self-intersecting region.

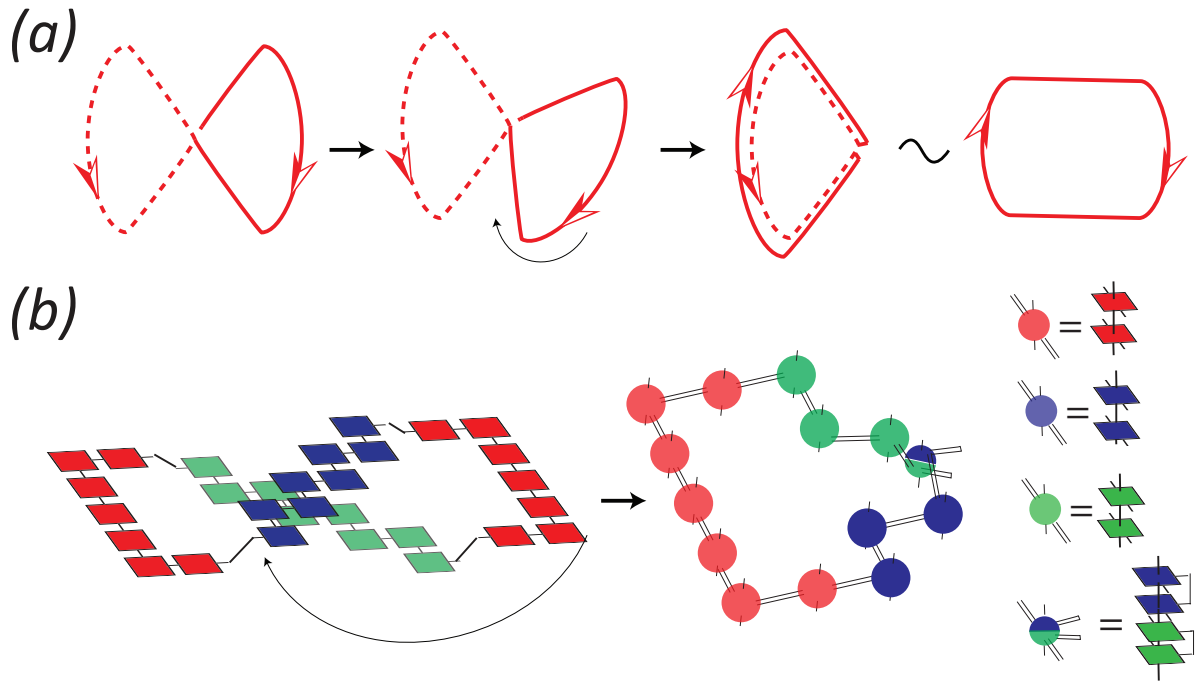

Figure 4.7: (a) Procedure for creating the support of WLO for process P_2 defined in Sec. 4.3.5 from process P_1. We start with the support of process P_1. We rotate the right half of the support and stack it on top of the left half of the support. This WLO is equivalent to a trivial loop. (b) Transformation from the WLO for process P_1 to process P_2, using the procedure described in (a).

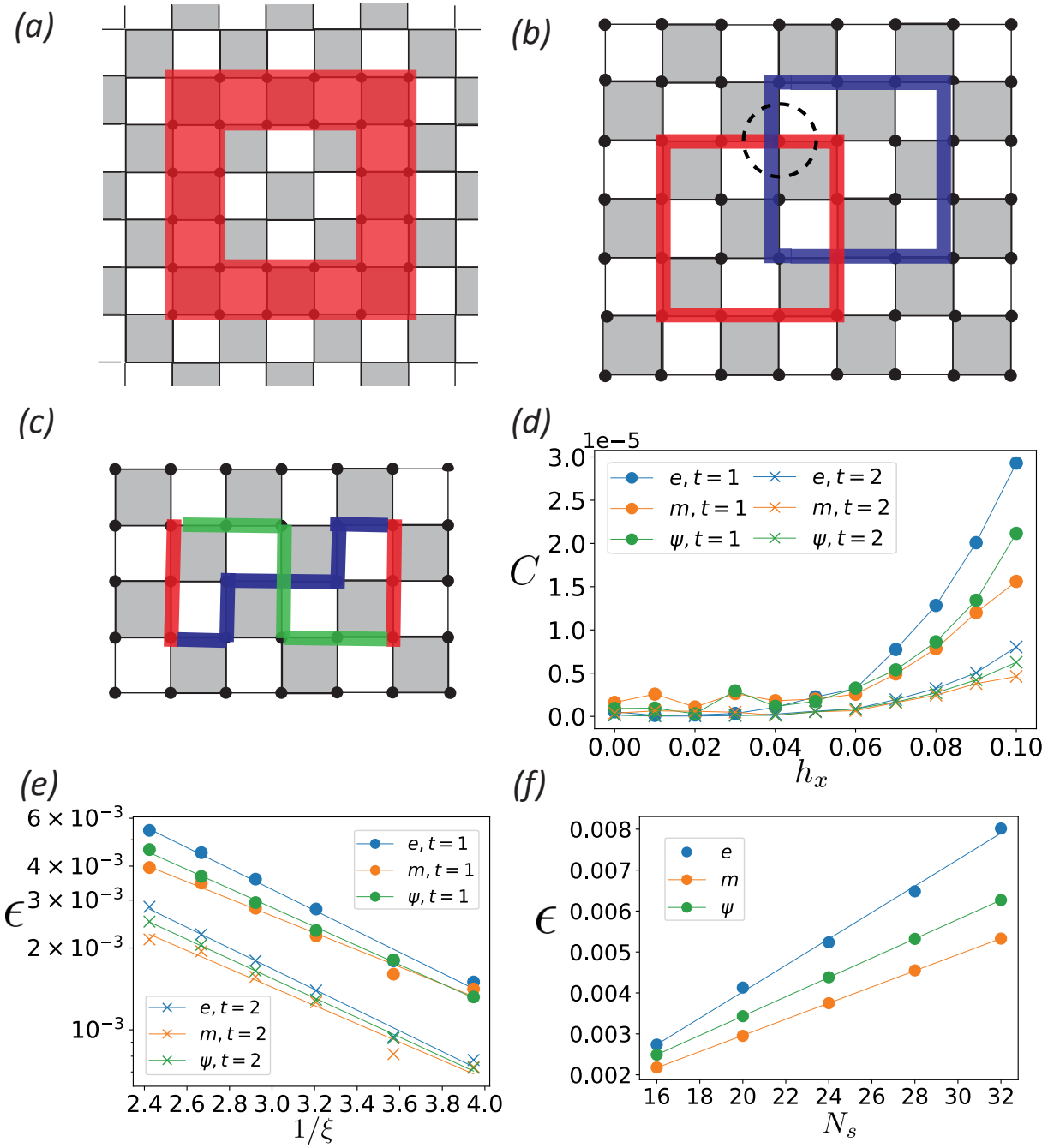

Figure 4.8: (a) Schematic of toric code model on an infinite plane. The red square is the region supporting the WLO. (b) The red and blue square are regions supporting the WLOs for calculating braiding statistic as described in 1.3.3. The circled region is region B defined in Eq. (1.12). (c) The curve is the region supporting the WLOs for calculating topological twist as described in 4.3.5. In the twist region, the blue curve is on top of the green curve. (d) The minimum costs as function of uniform magnetic field h_x for three anyon types in the toric code model with $h_z = 0.05$ and $\chi = 1$. For $t = 1$, the support of the Wilson loops is the perimeter of a $(L_x, Ly) = (6, 4)$ square. For $t = 2$, the support is depicted in (a). (e) The expectation value of the closed WLOs in renormalization group fixed points ($h_x = h_z = 0$), W_{FP} and the optimized closed WLOs as function of the magnetic field h_x. In this figure, $h_z = 0.05$, $L_x = 36$, $L_y = 6$, $\chi = 1$ and $t = 1$. (f) The error of the Wilson loop operators $\epsilon = |\langle W - W_{\text{exact}} \rangle|$ as function of the inverse of correlation length $(1/\xi)$ of the ground state wave function of toric code in uniform magnetic field with $h_z = 0.05$, $0.04 \leq h_x \leq 0.1$, $\chi = 1$. (g) The error of the Wilson loop operators ϵ as function of the number of sites N_s with $h_x = 0.1$, $h_z = 0.05$, $t = 1$, $\chi = 1$, $L_x = 4$. We vary N_s by increasing the side length L_x from $L_x = 4$ to $L_x = 8$.

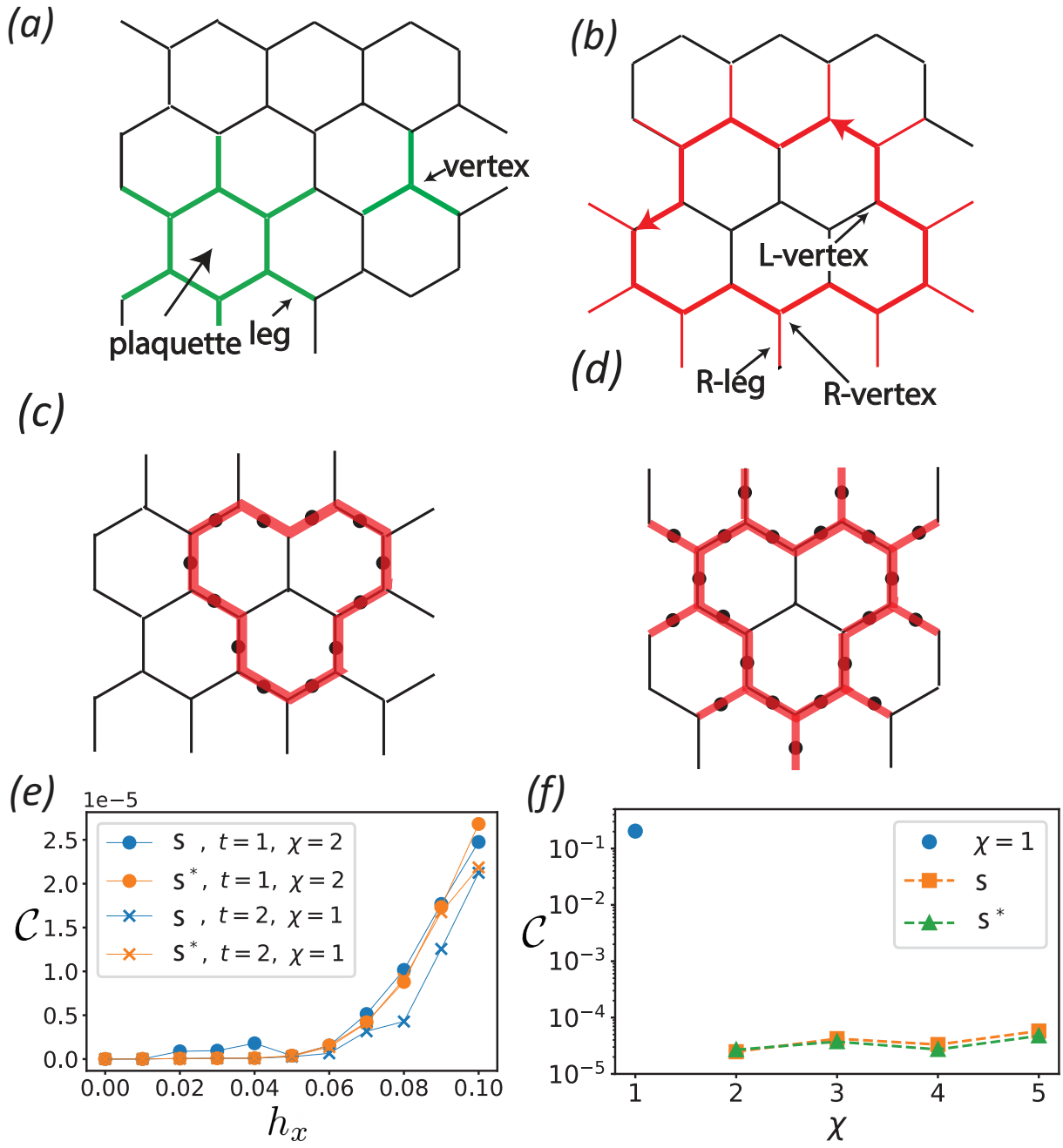

Figure 4.9: (a) Schematic of the plaquette and vertex for double semion model. The "legs" of a plaquette are the edges that stick out of the plaquette. (b) Schematic of the L-vertex, R-vertex and R-leg for double semion model. (c) and (d) The support of the Wilson loop operators with thickness $t = 1$ and $t = 2$ respectively. (e) The minimum cost as a function of uniform magnetic field h_x for two semions in the double semion model. The support of the Wilson loops are depicted in (c) and (d). (f) The minimum cost as a function of the bond dimension χ for the two semions for $h_x = 0.1$ and $t = 1$

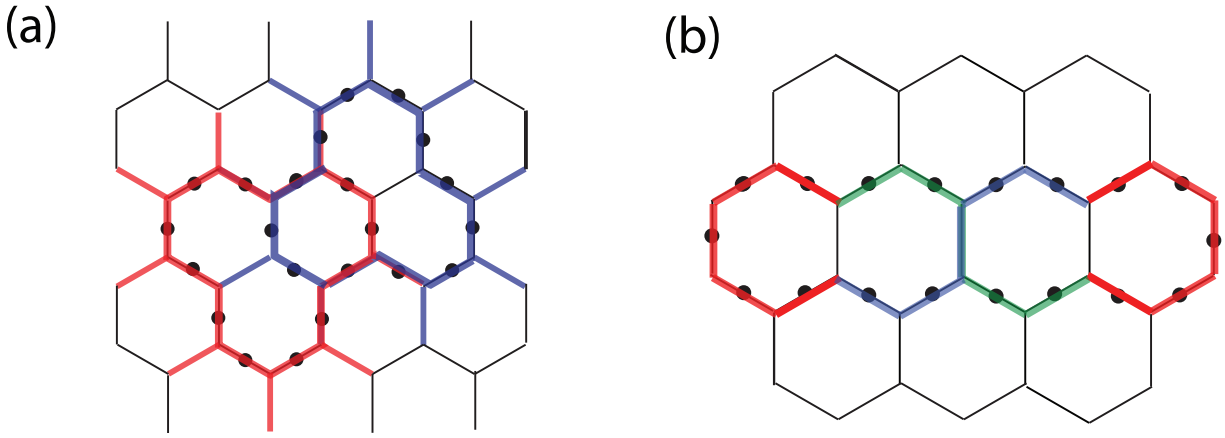

Figure 4.10: (a) The red and blue curves are regions supporting the WLOs for calculating braiding statistic for double semion model. (b) The twisted curve is the regions supporting the WLOs for calculating topological twist as described in 4.3.5. In the overlaping region, the blue curve is on top of the green curve.

Chapter 5: Conclusion and Outlook

In this dissertation, we have presented schemes to prepare and characterize topological phases of matter. In the preparation aspect in Chapter 2, we have demonstrated that an optically driven graphene in quantum Hall regime provides a versatile platform to study the bilayer quantum Hall physics. We further show that the system exhibits the bilayer Fibonacci phase which can be of interest for topological quantum computation with its non-abelian anyonic statistic. Apart from providing a synthetic bilayer structure, optical coupling between Landau levels may also enable the controlled engineering of three-body interaction terms from second-order transition processes. Future work on optically driven quantum Hall systems may explore this interesting scenario.

In Chapeter 3 and Appendix A, We have shown how a single wave function can be used to extract the many-body Chern number fractional quantum Hall system and we propose an ancilla-free protocol to extract the many-body Chern number in a NISQ quantum simulator. Our work opens up a new avenue for creating non-trivial topology on space-time manifold, using the SWAP operation. It is particularly intriguing that the SWAP operation can be implemented by random unitaries in the NISQ devices.

Finally, in Chapter 4, we propose a numerical protocol to measure the Wilson loop operators on the bulk of the ground state wave function. We present how to create, move and annihilate

anyons and measure the braiding statistic and topological spin of the anyon excitations. Therefore, we have extracted the braiding statistics and topological spins on anyons from the bulk of the ground state wave function.

From a fundamental prospective, it is intriguing to ask if one can characterize topological order for a wave function without any information from the Hamiltonian. To achieve this, we must remove the gap condition of the Hamiltonian. However, there exist models that are believed to be gapless, and the ground state wave function fails to exhibit several features of topological order. Yet, they have loop operators satisfying Eq. (**??**) and the twist products of loop operators are not equal to one. Examples include the two-dimensional quantum compass model (Bacon-Shor's code) [136, 137] and the deformed toric code model [138]. It is therefore interesting to further investigate the locally invisible operator [55] in the gapless system.

More broadly, the development of the quantum simulators opens the new avenue to realize topologically-ordered states that might not occur in a conventional electronic matter. It is therefore important to develop measurement protocols that go beyond linear response formalism.

Appendix A: Extraction of the many-body Chern number from a single wave function

This chapter is based on the author's contribution to Ref. [43]. We briefly describe the results and detail the author's contribution. We refer the reader to the original manuscript for more details [43].

A.1 Summary of the results

Let us consider a gapped many-body ground state $|0\rangle$ in (2+1)D with $U(1)$ symmetry. The system possesses an integer-valued invariant, the many-body Chern number C, which determines the Hall conductivity through the formula

$$\sigma_H = C\frac{1}{s}\frac{e^2}{h} = \frac{p}{q}\frac{e^2}{h}, \tag{A.1}$$

where p and q are coprime. Here s is another integer invariant that can be understood as follows. We consider the flux insertion operator $\hat{\Phi}_x$ for adiabatic insertion of 2π flux through the x cycle of the torus. s is then the minimal integer such that, given any ground state $|\psi\rangle$ on a torus,

$$\hat{\Phi}_x^s|\psi\rangle = |\psi\rangle. \tag{A.2}$$

Alternatively, adiabatically inserting flux at some point in the system gives a Laughlin quasihole, v, which we refer to as the vison. v is in general a topologically non-trivial excitation with fractional charge $Q_v = p/q$, and statistics $\theta_v = \pi p/q$. s is defined as the minimal integer such that v^s is a topologically trivial excitation. Furthermore, as we show in Appendix **??**, all fractional electric charges of the quasiparticles are integer multiples of $1/s$. For an IQH state which does not host any topologically non-trivial excitations, $s = q = 1$. However for a general FQH state, it follows that $s = rq$ for some integer r.

The state $|0\rangle$ that we consider can be defined on any space. For concreteness we take it to be defined on either a cylindrical geometry or an open region with coordinates $(x, y) \in [0, L_x] \times [0, L_y]$. In the cylindrical case, we take the y direction to be compactified.

We present the following formulas for the many-body Chern number:

$$C = \frac{1}{2\pi} \frac{d}{d\phi} \arg \mathcal{T}(\phi; s). \tag{A.3}$$

Here, $\arg \mathcal{T}(\phi; s) = \mathrm{Im} \ln \mathcal{T}(\phi; s)$, and $\mathcal{T}(\phi; s)$ is defined below. Note that $\arg \mathcal{T}(\phi; s)$ is linear in ϕ (in the thermodynamic limit), so that the slope can be calculated at any value of ϕ. This equation is reminiscent of formulas for measuring Chern number using polarization as a function of the twist angle on a cylinder. However $\mathcal{T}(\phi; s)$ defined here depends only on a single wave function, independent of any underlying Hamiltonian.

We note that for finite-size systems, it is more robust to compute the average Chern number from the winding number,

$$C = \frac{1}{2\pi} \oint d\phi \frac{d}{d\phi} \arg \mathcal{T}(\phi; s), \tag{A.4}$$

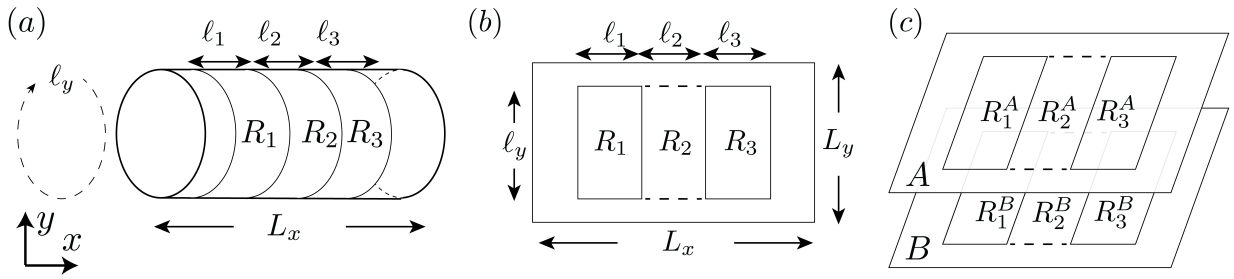

Figure A.1: Spatial geometries corresponding to the one-layer and bilayer formulas (A.5), (A.6) on a cylinder or rectangle. (a) We impose periodic boundary conditions along the y-direction corresponding to a cylinder in the $x-y$ space, and have the R_i regions wrap all along the y-cycle so that $\ell_y = L_y$. (b) We impose open boundary condition along the y-direction corresponding to a rectangle in the $x-y$ space, and have the R_i regions to be rectangular. In (a) and (b) to evaluate (A.5) regions R_1 and R_3 in the bra and ket states are swapped, therefore, $\ell_3 = \ell_1$. (c) Given a copy A and B of the wave function on the same rectangular geometry, to evaluate (A.6), the swap operator is applied to regions R_1^A and R_1^B and to R_3^A and R_3^B of the two wave functions. Similarly, one can impose periodic boundary conditions on the two copies of the wave function.

where ϕ winds from 0 to 2π. For $\mathcal{T}(\phi; s)$, we can consider two classes of formulas, based on using either a single copy of the state or two copies of the state:

$$\mathcal{T}(\phi; s) = \langle 0 | W^\dagger_{R_1}(\phi) S_{1,3} W_{R_1}(\phi) V^s_{R_1 \cup R_2} | 0 \rangle, \tag{A.5}$$

$$\mathcal{T}(\phi; s) = \langle 0_A 0_B | W^\dagger_{R_1^A}(\phi) V^{s\dagger}_{R_2^B} S_{1_A,1_B} S_{3_A,3_B} W_{R_1^A}(\phi) V^s_{R_2^A} | 0_A 0_B \rangle. \tag{A.6}$$

Let us first consider Eq. (A.5), which requires a single copy of the state. We have picked three subregions of the space, R_1, R_2, and R_3, which can be either cylindrical or rectangular, as shown in Fig. A.1(a) and Fig. A.1(b), respectively:

$$R_i = \{(x, y) | x_i \le x < x_{i+1}, y_1 \le y \le y_2\}. \tag{A.7}$$

In the case where the regions are cylindrical as in Fig. A.1(a), we take $y_1 = 0$ and $y_2 = L_y \sim 0$. We require R_1 and R_3 to have the same lengths along the x-direction:

$$\ell_i \equiv |x_{i+1} - x_i|, \quad i = 1, 2, 3,$$
$$\ell_y \equiv |y_2 - y_1|. \tag{A.8}$$

When the regions are cylindrical, $\ell_y = L_y$.

$S_{1,3}$ is a SWAP operator that swaps every particle in R_1 to its corresponding point in R_3 and vice versa. It can be written as

$$S_{R_1,R_3} = \prod_{(x,y)\in R_1} \text{SWAP}((x, y), (x', y)), \tag{A.9}$$

where $x' = x + (x_3 - x_1)$. Here SWAP$(\vec{r}, \vec{r}')$ moves any particle at $\vec{r}$ to $\vec{r}'$ and vice versa. Note that if we consider the Hilbert space $\mathcal{H}_R$ of the system restricted to a region R, we need $\mathcal{H}_{R_1}$ and $\mathcal{H}_{R_3}$ to be isomorphic so that we can define the above SWAP operator.

The operators V_R and $W_R(\phi)$, which have support in region R, take the form

$$W_R(\phi) = \prod_{(x,y)\in R} e^{i\hat{n}(x,y)\phi}$$
$$V_R = \prod_{(x,y)\in R} e^{i\frac{2\pi y}{\ell_y}\hat{n}(x,y)} \tag{A.10}$$

where $\hat{n}(x, y)$ is the number density operator.

Eq. (A.6) is defined by considering two identical copies of the given state, $|0_A 0_B\rangle \equiv |0\rangle_A \otimes |0\rangle_B$, where A and B label the two copies as in Fig. A.1(c). Here, R_i^I for $I = A, B$ and $i = 1, 2, 3$

now label two identical sets of three regions for the two copies of the system. In this case as well we can consider both cylindrical and rectangular geometries; Fig. A.1(c) shows the rectangular case. Eq. (A.6) is written entirely in terms of local operators, at the expense of requiring two copies of the system. This is reminiscent of the approach in Ref. zhu2017 to extract fractional statistics through a product of purely on-site unitary operations by considering multiple copies of a topologically ordered state. It is also analogous to the proposal of Ref. [18] for extracting SPT invariants using two-copies of the state.

Eq. (A.5) and (A.6) are special cases of a more general set of formulas for $\mathcal{T}(\phi; s)$:

$$\mathcal{T}(\phi; s) = \left\{ \frac{\langle 0| \left(W^a_{R_1}(\phi) V^{sc}_{R_1}\right)^\dagger S_{1,3} \left(W^a_{R_1}(\phi) V^{sc}_{R_1}\right) W^b_{R_1 \cup R_2}(\phi) V^{sd}_{R_1 \cup R_2} |0\rangle}{\langle 0| \left(W^a_{R_1}(\phi)\right)^\dagger S_{1,3} W^a_{R_1}(\phi) W^b_{R_1 \cup R_2}(\phi) |0\rangle} \right\}^{1/\det U}, \tag{A.11}$$

$$\mathcal{T}(\phi; s) = \left\{ \frac{\langle 0_A 0_B| \left[W^a_{R_1^A}(\phi) V^{sc}_{R_1^A} V^{sd}_{R_2^B} W^b_{R_2^B}(\phi)\right]^\dagger S_{1_A,1_B} S_{3_A,3_B} \left[W^a_{R_1^A}(\phi) V^{sc}_{R_1^A} V^{sd}_{R_2^A} W^b_{R_2^A}(\phi)\right] |0_A 0_B\rangle}{\langle 0_A 0_B| \left[W^a_{R_1^A}(\phi) W^b_{R_2^B}(\phi)\right]^\dagger S_{1_A,1_B} S_{3_A,3_B} \left[W^a_{R_1^A}(\phi) W^b_{R_2^A}(\phi)\right] |0_A 0_B\rangle} \right\}^{1/\det U}. \tag{A.12}$$

where $U = \begin{pmatrix} a & b \\ c & d \end{pmatrix}$ is a GL$(2, Z)$ matrix (i.e. $a, b, c, d \in Z$ and $ad - bc \neq 0$). Note that any choice of $U \in$ GL$(2, Z)$ can be used to obtain the Chern number. Eq. (A.11)-(A.13) therefore yield an infinite number of different formulae which in principle can be used to obtain the Chern number.

If $b = 0$, the denominator in Eq. (A.11)-(A.12) is real, and therefore does not contribute to

the Chern number. Eq. (A.5)-(A.6) correspond to the case where $U = \begin{pmatrix} 1 & 0 \\ 0 & 1 \end{pmatrix}$ is the identity matrix, and we have ignored the denominator.

We note that the numerator of Eq. (A.11) for $U = \begin{pmatrix} 0 & 1 \\ -1 & 1 \end{pmatrix}$ and $s = 1$ was proposed in Ref. Shiozaki2018many for extracting the many-body Chern number for integer Chern insulators from the ground state defined on a cylinder. However, we find that the denominator is also crucial to obtain correct results.

We find that we can also remove the swap in region R_3 above, to instead use the formula:

$$\mathcal{T}(\phi; s) = \left\{ \frac{\langle 0_A 0_B | \left[W^a_{R_1^A}(\phi) V^{sc}_{R_1^A} V^{sd}_{R_2^B} W^b_{R_2^B}(\phi) \right]^\dagger S_{1_A, 1_B} \left[W^a_{R_1^A}(\phi) V^{sc}_{R_1^A} V^{sd}_{R_2^A} W^b_{R_2^A}(\phi) \right] |0_A 0_B\rangle}{\langle 0_A 0_B | \left[W^a_{R_1^A}(\phi) W^b_{R_2^B}(\phi) \right]^\dagger S_{1_A, 1_B} \left[W^a_{R_1^A}(\phi) W^b_{R_2^A}(\phi) \right] |0_A 0_B\rangle} \right\}^{1/\det U} . \tag{A.13}$$

However we find from our numerical simulations that Eq. (A.13) is not as robust as Eq. (A.12) for finite size systems.

In the case where the regions R_i are cylindrical, we have an analytical understanding of these formulas in terms of topological quantum field theory (TQFT), which is backed up by extensive numerical simulations. However in the case where the regions R_i are rectangular, we do not have an analytical understanding in terms of TQFT. Nevertheless, our numerical results indicate that the formulas continue to reproduce the Chern number.

A.2 Numerical results

In this section we present extensive numerical simulations of the formulas of Eqs. (A.5),(A.6),(A.11),(A.12 for IQH and FQH states. Specifically, we present our results demonstrating how the Chern number can be extracted using Eqs. (A.5),(A.6),(A.11),(A.12),(A.13) for both cylindrical and rectangular geometries. We show that our numerical results are consistent with the analytical expectations.

For quantum Hall states, we use matrix product state (MPS) simulations on both cylindrical and rectangular geometries. For bosonic states, we consider the Laughlin state with filling fraction $\nu = 1/2$ [105], the bosonic Jain state at $\nu = 2/3$, the bosonic integer quantum Hall state at $\nu = 2$ [**?**] and the Moore-Read state with $\nu = 1$. For fermions, we consider the integer quantum Hall state with $\nu = 1$, and a free-fermion Chern insulator. For these non-interacting fermionic models, we use the Slater determinant representation of the many-body wave function of the system. This allows us to access larger system sizes compared to the interacting bosonic/fermionic cases. In particular, we use the free-fermion model to investigate the effect of changing the support of the symmetry defect operators on the Chern number in Sec. **??**, and to study the scaling of various expectation values with respect to the subregion size in Sec. **??**.

We start with the interacting Hofstadter model on a square lattice, which can realize a variety of fractional quantum Hall states at different values of the filling and flux per plaquette [**?**

?]. The Hamiltonian is of the form

$$H = -J \sum_{x,y} e^{i2\pi\alpha x} a^{\dagger}_{x,y+1} a_{x,y} + a^{\dagger}_{x+1,y} a_{x,y} + \text{h.c.}, \tag{A.14}$$

where α is magnetic flux per plaquette, the sum is taken over $x = 1, \cdots, L_x$ and $y = 1, \cdots, L_y$, where L_x and L_y are the number of lattice sites along the x and y directions, respectively. For the bosonic quantum Hall system, with $\nu = 1/2, 2/3$ and 2, the operator $a(x, y)$ obeys the commutation relation $[a(x, y), a^{\dagger}(x', y')] = \delta_{x,x'}\delta_{y,y'}$ and the hardcore condition $(a^{\dagger}(x, y))^2 = 0$. For the Pfaffian MR-state with $\nu = 1$, we impose the three body interaction $(a^{\dagger}(x, y))^3 = 0$. For the fermionic quantum Hall system, with $\nu = 1$, the operators obey the anti-commutation relation $\{a(x, y), a^{\dagger}(x', y')\} = \delta_{x,x'}\delta_{y,y'}$. For low flux density $\alpha \ll 1$, the lattice model is known to produce many-body states similar to the continuum model [105]. The ground state is obtained by performing density matrix renormalization group (DMRG) simulation [**?**].

We first consider a cylindrical geometry, where we impose periodic boundary conditions along the y axis of Fig. A.1(a) and choose the regions R_i to wrap the y direction, such that $\ell_y = L_y$. The numerical results for $\arg[\mathcal{T}(\phi; s)]$ as defined in Eq. (A.11) and (A.12), along with the choice of parameters in the simulation, are shown in Fig. A.2. As we can see in this figure, if the system size is sufficiently large, the slopes of the curves are nearly constant and thus can be used to obtain the Chern number.

Model	s	C	Formula	Geometry	Figure
QH $\nu = 1/2$ B	2	1	Eqs. (A.11,A.12)	Cylinder	Fig. A.2
QH $\nu = 2/3$ B	3	2			
QH $\nu = 2$ B	1	2			
QH $\nu = 1$ F	1	2			
QH $\nu = 1$ B MR	2	2			
QH $\nu = 1/2$ B	2	1	Eqs. (A.11,A.12)	Rectangle	Fig. A.3
QH $\nu = 1$ F	1	1			
QH $\nu = 1/2$ B	2	1	Eq. (A.13)	Cylinder	Fig. A.4
QH $\nu = 2/3$ B	3	2			
QH $\nu = 2$ B	1	2			
QH $\nu = 1$ F	1	1			
QH $\nu = 1$ B MR	2	2			
QH $\nu = 1/2$ B	2	1		Rectangle	
QH $\nu = 1$ F	1	1			
Chern insulator	1	1	Eq. (A.11)	Cylinder	Fig. **??**

Table A.1: Summary of the numerical simulations. B/F stands for bosonic/fermionic states, respectively. MR stands for Moore-Read state.

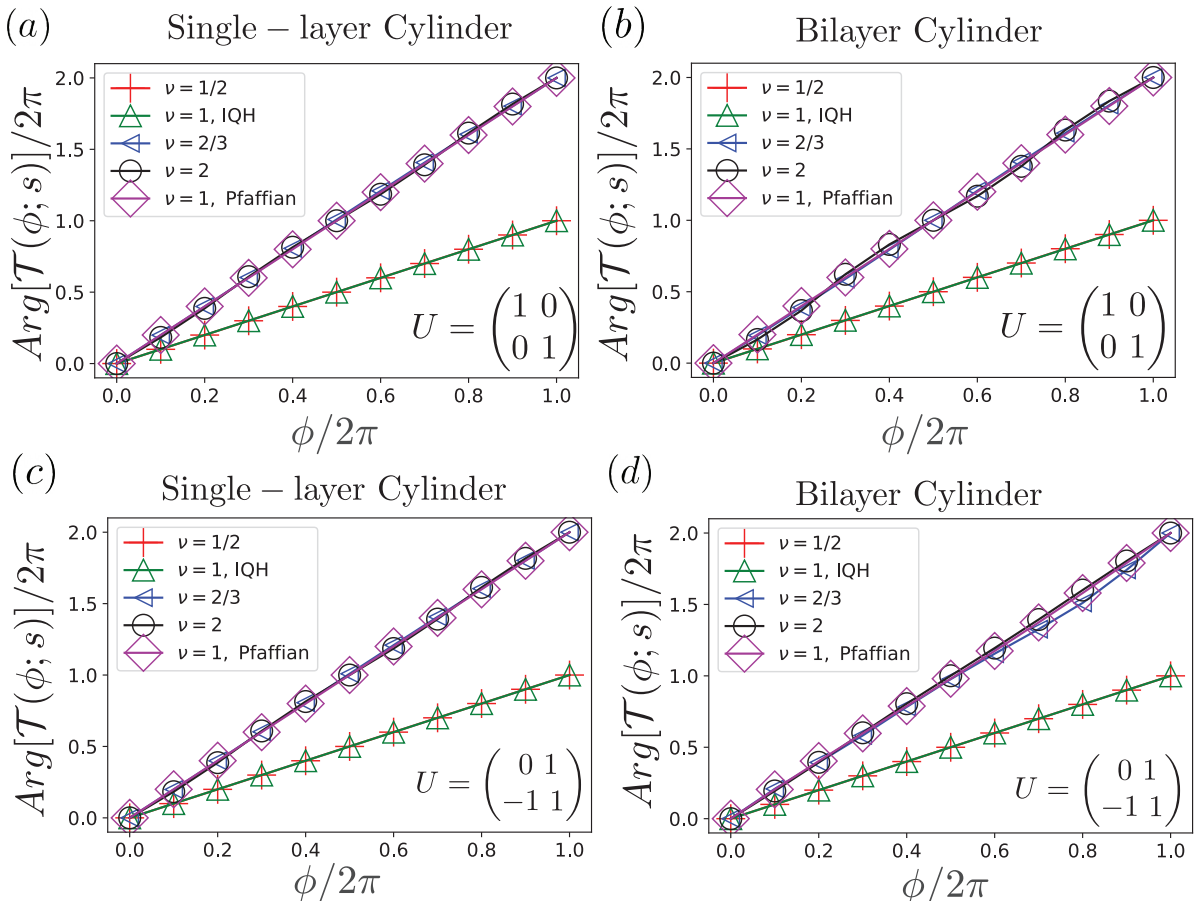

Figure A.2: The simulation results for single and bilayer formulas (Eqs. (A.11) and (A.12)) with cylindrical geometry for quantum Hall states. For the bosonic Laughlin state with filling fraction $\nu = 1/2$, we choose $\alpha = 1/6$, $L_y = \ell_1 = \ell_2 = \ell_3 = 6$, $L_x = 30$ and $s = 2$. For the Jain sequence state with $\nu = 2/3$, $\alpha = 1/9$, $L_y = \ell_1 = \ell_2 = \ell_3 = 9$, $L_x = 45$ and $s = 3$. For the bosonic integer quantum Hall state with $\nu = 2$, $\alpha = 1/6$, $L_y = \ell_1 = \ell_2 = \ell_3 = 6$, $L_x = 40$ and $s = 1$. For the fermionic integer quantum Hall state with $\nu = 1$, $\alpha = 1/6$, $L_x = 40$, $L_y = \ell_1 = \ell_2 = \ell_3 = 6$ and $s = 1$. For the bosonic Pfaffian MR-state with $\nu = 1$, $\alpha = 1/6$, $L_x = 60$, $L_y = 6, \ell_1 = \ell_2 = \ell_3 = 12$ and $s = 2$. Corresponding U's are shown in each panel.

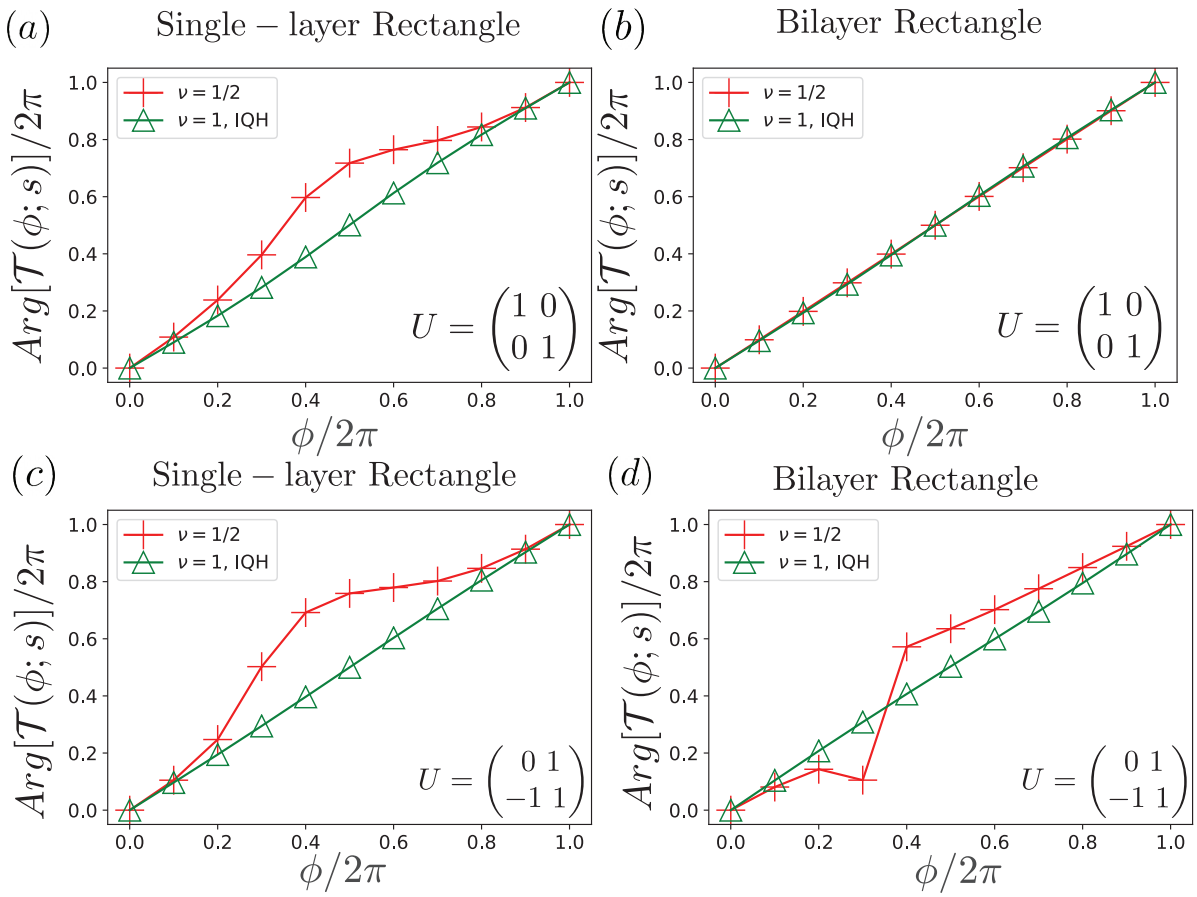

Figure A.3: The simulation results for single and bilayer formulas (Eqs. (A.11) and (A.12)) with rectangular geometry for quantum Hall states. For the bosonic Laughlin state with $\nu = 1/2$, we choose $\alpha = 1/6$, $L_x = 40$, $L_y = 9$, and $\ell_1 = \ell_2 = 9$, $\ell_y = 7$ and $s = 2$. For the fermionic integer quantum Hall state with $\nu = 1$, $\alpha = 1/4$, $L_x = 30$, $L_y = 8$, $\ell_1 = \ell_2 = \ell_y = 8$ and $s = 1$. Corresponding U's are shown in each panel.

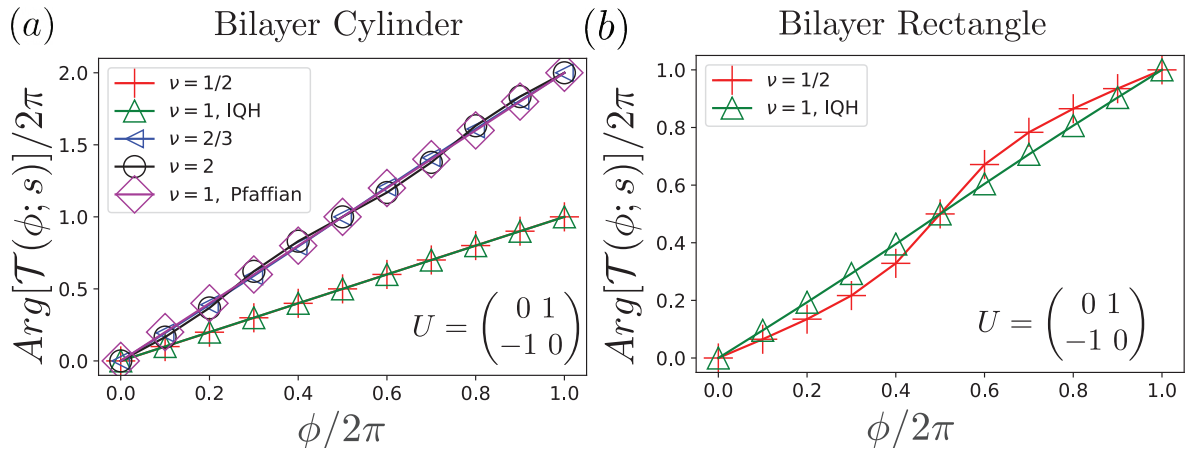

Figure A.4: The simulation result of single SWAP for bilayer formula (Eq. (A.13)). (a) Cylindrical geometry, with layer parameters identical to Fig. A.2. (b) Rectangular geometry, with layer parameters identical to Fig. A.3.

We also consider systems in the rectangular geometry as shown in Fig. A.1(b),(c). The length of the swapped regions R_i along the y direction is denoted by ℓ_y while the total length along the y direction is denoted by L_y as before. Since the Landau level of the Hofstadter model is not flat for small system sizes in the rectangular geometry, we do not find robust FQH states at $\nu = 2/3$ and $\nu = 2$ at the system sizes that we access. The winding number of $\arg[\mathcal{T}(\phi; s)]$ is an integer by definition, however it jumps to different values and is not converged with system size for $\nu = 2/3$ and $\nu = 2$. This is also the case even when we flatten the bands using the Kapit-Mueller tunneling terms [**?**]. We thus present in Fig. A.3 the result of the Chern number calculation for the $\nu = 1/2$ Laughlin state and the fermionic integer quantum Hall state with $\nu = 1$, which are robust to boundary effects in our simulations. As expected the winding number of the phase of the twist operator generates the correct Chern number. However, unlike in Fig. A.2, where we observe a linear behavior in ϕ, the finite size effects are significantly larger; nevertheless the winding number still correctly reproduces the Chern number in the system sizes that we have

accessed.

In Fig. A.4, we present the results for the bilayer formula where the SWAP in region R_3 is removed, as in Eq. (A.13). Although both the single and two SWAP bilayer formulas of Eq. (A.12) and (A.13) can be used to obtain the Chern number, the single SWAP formula Eq. (A.13) is significantly easier to implement in an experiment, and therefore, this formula is used in Ref. [**?**]. The results are consistent with the theoretical prediction. We summarize the simulation results for Figs. A.2, A.3 and A.5 in Table A.1.

In order to provide more evidence for the formulas of Eqs. (A.5),(A.6),(A.11),(A.12),(A.13) in the rectangular geometry, we perform finite size scaling for Eq. (A.13), as shown in Fig. A.5(a). We observe that when the areas of the regions R_1 and R_2 are large enough, the resulting Chern number converges to one. In addition, we also consider a fractional quantum Hall to Mott insulator phase transition by adding an extra potential term $V = M\sum(-1)^{p_x+y}\hat{n}(x,y)$, where $p_x = \lfloor \alpha x \rfloor$ in Eq. (A.14). The system undergoes a phase transition from a FQH phase to a Mott insulator when M is increased [105]. In Fig. A.5, we plot the correlation length ξ and the Chern number computed by Eq. (A.13) as functions of M. Although the correlation length peaks around the critical point ($M \sim 0.2$), it remains finite due to the finite bond dimension of the MPS which is chosen to be $\chi = 200$. We can see that the value of M at which the phase transition in the Chern number occurs and the the value of M at which the extremum of the correlation length occurs, are approximately coincident. This coincidence, which by increasing the bond dimension becomes more accurate, indicates that the SWAP formula in Eq. (A.13) can still detect the Chern number correctly, even in rectangular geometries.

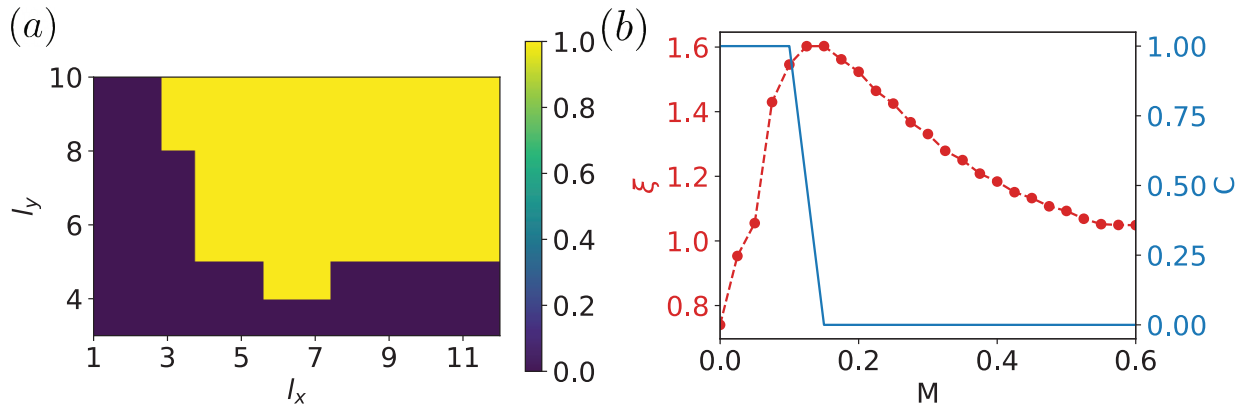

Figure A.5: (a) The simulation result for bilayer formula Eq. (A.13) with various region size. We consider the Laughlin state with $\nu = 1/2$, we choose $\alpha = 1/6$, $L_x = 40$, $L_y = 12$ and $\ell_1 = \ell_2 = \ell_x$ and $U = \begin{pmatrix} 0 & 1 \\ -1 & 0 \end{pmatrix}$. (b) Phase transition of a Laughlin state to a Mott insulator. The correlation length ξ (red) and the Chern number C (blue) are shown as functions of M. M is defined in the main text. We choose $L_x = 25$, $L_y = 12$, $\alpha = 1/6$ and $U = \begin{pmatrix} 0 & 1 \\ -1 & 0 \end{pmatrix}$. The correlation length remains finite around the critical point due the truncation of the bond dimension.

We have also numerically evaluated with our DMRG simulations both the single layer and bilayer formulas with cylindrical and rectangular geometry, Eq. (A.11) and (A.12), with all possible choices of $U \in \mathrm{SL}^{\pm}(2, Z)$ that have $|a|, |b|, |c|, |d| \leq 1$. While cases with $|a| > 1$ and $b = 0$ trivially correspond to rescaling ϕ, in general choosing $|a|, |b|, |c|, |d| > 1$ does not typically give stable results at the system sizes that are accessible to us.

Bibliography

[1] Xiao-Gang Wen. *Quantum field theory of many-body systems: from the origin of sound to an origin of light and electrons*. Oxford University Press on Demand, 2004.

[2] Chetan Nayak, Steven H Simon, Ady Stern, Michael Freedman, and Sankar Das Sarma. Non-abelian anyons and topological quantum computation. *Reviews of Modern Physics*, 80(3):1083, 2008.

[3] N. R. Cooper, J. Dalibard, and I. B. Spielman. Topological bands for ultracold atoms. *Rev. Mod. Phys.*, 91:015005, Mar 2019.

[4] Andrew A Houck, Hakan E Türeci, and Jens Koch. On-chip quantum simulation with superconducting circuits. *Nature Physics*, 8(4):292, 2012.

[5] Pedram Roushan, Charles Neill, Anthony Megrant, Yu Chen, Ryan Babbush, Rami Barends, Brooks Campbell, Zijun Chen, Ben Chiaro, Andrew Dunsworth, et al. Chiral ground-state currents of interacting photons in a synthetic magnetic field. *Nature Physics*, 13(2):146–151, 2017.

[6] Tomoki Ozawa, Hannah M Price, Alberto Amo, Nathan Goldman, Mohammad Hafezi, Ling Lu, Mikael C Rechtsman, David Schuster, Jonathan Simon, Oded Zilberberg, et al. Topological photonics. *Reviews of Modern Physics*, 91(1):015006, 2019.

[7] Logan W Clark, Nathan Schine, Claire Baum, Ningyuan Jia, and Jonathan Simon. Observation of laughlin states made of light. *arXiv preprint arXiv:1907.05872*, 2019.

[8] Antoine Browaeys and Thierry Lahaye. Many-body physics with individually controlled rydberg atoms. *Nature Physics*, pages 1–11, 2020.

[9] Cecile Repellin and Nathan Goldman. Detecting fractional chern insulators through circular dichroism. *Physical review letters*, 122(16):166801, 2019.

[10] Duc Thanh Tran, Alexandre Dauphin, Adolfo G Grushin, Peter Zoller, and Nathan Goldman. Probing topology by " heating ": Quantized circular dichroism in ultracold atoms. *Science advances*, 3(8):e1701207, 2017.

[11] Luca Asteria, Duc Thanh Tran, Tomoki Ozawa, Matthias Tarnowski, Benno S Rem, Nick Fläschner, Klaus Sengstock, Nathan Goldman, and Christof Weitenberg. Measuring quantized circular dichroism in ultracold topological matter. *Nature physics*, 15(5):449–454, 2019.

[12] C Repellin, J Léonard, and N Goldman. Hall drift of fractional chern insulators in few-boson systems. *arXiv preprint arXiv:2005.09689*, 2020.

[13] Johannes Motruk and Ilyoun Na. Detecting fractional chern insulators in optical lattices through quantized displacement. *arXiv preprint arXiv:2005.09860*, 2020.

[14] Fabian Grusdt, Norman Y Yao, D Abanin, Michael Fleischhauer, and E Demler. Interferometric measurements of many-body topological invariants using mobile impurities. *Nature communications*, 7:11994, 2016.

[15] Hannes Pichler, Guanyu Zhu, Alireza Seif, Peter Zoller, and Mohammad Hafezi. Measurement protocol for the entanglement spectrum of cold atoms. *Physical Review X*, 6(4):041033, 2016.

[16] Marcel den Nijs and Koos Rommelse. Preroughening transitions in crystal surfaces and valence-bond phases in quantum spin chains. *Phys. Rev. B*, 40:4709–4734, Sep 1989.

[17] Frank Pollmann and Ari M. Turner. Detection of symmetry-protected topological phases in one dimension. *Phys. Rev. B*, 86:125441, Sep 2012.

[18] Jutho Haegeman, David Pérez-García, Ignacio Cirac, and Norbert Schuch. Order parameter for symmetry-protected phases in one dimension. *Phys. Rev. Lett.*, 109:050402, Jul 2012.

[19] Ken Shiozaki and Shinsei Ryu. Matrix product states and equivariant topological field theories for bosonic symmetry-protected topological phases in (1+1) dimensions. *Journal of High Energy Physics*, 2017(4):100, Apr 2017.

[20] Ken Shiozaki, Hassan Shapourian, Kiyonori Gomi, and Shinsei Ryu. Many-body topological invariants for fermionic short-range entangled topological phases protected by antiunitary symmetries. *Phys. Rev. B*, 98:035151, Jul 2018.

[21] Andreas Elben, Jinlong Yu, Guanyu Zhu, Mohammad Hafezi, Frank Pollmann, Peter Zoller, and Benoît Vermersch. Many-body topological invariants from randomized measurements in synthetic quantum matter. *Science advances*, 6(15):eaaz3666, 2020.

[22] Maissam Barkeshli, Parsa Bonderson, Meng Cheng, and Zhenghan Wang. Symmetry fractionalization, defects, and gauging of topological phases. *Phys. Rev. B*, 100:115147, Sep 2019.

[23] Daniel Bulmash and Maissam Barkeshli. Fermionic symmetry fractionalization in (2+1)d, 2021.

[24] Maissam Barkeshli, Yu-An Chen, Po-Shen Hsin, and Naren Manjunath. Classification of (2+1)d invertible fermionic topological phases with symmetry, 2021.

[25] David Aasen, Parsa Bonderson, and Christina Knapp. Characterization and Classification of Fermionic Symmetry Enriched Topological Phases, 2021.

[26] Qing-Rui Wang and Zheng-Cheng Gu. Construction and Classification of Symmetry-Protected Topological Phases in Interacting Fermion Systems. *Phys. Rev. X*, 10:31055, 2020.

[27] Alexei Kitaev and John Preskill. Topological entanglement entropy. *Physical review letters*, 96(11):110404, 2006.

[28] Michael Levin and Xiao-Gang Wen. Detecting topological order in a ground state wave function. *Physical review letters*, 96(11):110405, 2006.

[29] Yi Zhang, Tarun Grover, Ari Turner, Masaki Oshikawa, and Ashvin Vishwanath. Quasiparticle statistics and braiding from ground-state entanglement. *Physical Review B*, 85(23):235151, 2012.

[30] Yi Zhang, Tarun Grover, and Ashvin Vishwanath. General procedure for determining braiding and statistics of anyons using entanglement interferometry. *Physical Review B*, 91(3), Jan 2015.

[31] X.G. Wen. Topological orders in rigid states. *Int. J. Mod. Phys.*, B:239, 1990.

[32] Guanyu Zhu, Mohammad Hafezi, and Maissam Barkeshli. Quantum origami: Transversal gates for quantum computation and measurement of topological order. *Physical Review Research*, 2(1), Mar 2020.

[33] Hossein Dehghani, Ze-Pei Cian, Mohammad Hafezi, and Maissam Barkeshli. Extraction of the many-body chern number from a single wave function. *Physical Review B*, 103(7):075102, 2021.

[34] Ze-Pei Cian, Hossein Dehghani, Andreas Elben, Benoît Vermersch, Guanyu Zhu, Maissam Barkeshli, Peter Zoller, and Mohammad Hafezi. Many-body chern number from statistical correlations of randomized measurements. *Physical Review Letters*, 126(5):050501, 2021.

[35] Hui Li and F. D. M. Haldane. Entanglement spectrum as a generalization of entanglement entropy: Identification of topological order in non-abelian fractional quantum hall effect states. *Phys. Rev. Lett.*, 101:010504, Jul 2008.

[36] Isaac H Kim, Bowen Shi, Kohtaro Kato, and Victor V Albert. Modular commutator in gapped quantum many-body systems. *arXiv preprint arXiv:2110.10400*, 2021.

[37] Isaac H Kim, Bowen Shi, Kohtaro Kato, and Victor V Albert. Chiral central charge from a single bulk wave function. *arXiv preprint arXiv:2110.06932*, 2021.

[38] Hong-Hao Tu, Yi Zhang, and Xiao-Liang Qi. Momentum polarization: An entanglement measure of topological spin and chiral central charge. *Physical Review B*, 88(19), Nov 2013.

[39] Michael P. Zaletel, Roger S. K. Mong, and Frank Pollmann. Topological characterization of fractional quantum hall ground states from microscopic hamiltonians. *Physical Review Letters*, 110(23), Jun 2013.

[40] Matthew B Hastings and Xiao-Gang Wen. Quasiadiabatic continuation of quantum states: The stability of topological ground-state degeneracy and emergent gauge invariance. *Physical review b*, 72(4):045141, 2005.

[41] Xie Chen, Zheng-Cheng Gu, and Xiao-Gang Wen. Local unitary transformation, long-range quantum entanglement, wave function renormalization, and topological order. *Physical review b*, 82(15):155138, 2010.

[42] Bei Zeng, Xie Chen, Duan-Lu Zhou, and Xiao-Gang Wen. Quantum information meets quantum matter–from quantum entanglement to topological phase in many-body systems. *arXiv preprint arXiv:1508.02595*, 2015.

[43] Hossein Dehghani, Ze-Pei Cian, Mohammad Hafezi, and Maissam Barkeshli. Extraction of many-body chern number from a single wave function. *arXiv preprint arXiv:2005.13677*, 2020.

[44] Qian Niu, D. J. Thouless, and Yong-Shi Wu. Quantized hall conductance as a topological invariant. *Phys. Rev. B*, 31:3372–3377, Mar 1985.

[45] Raffaele Resta. Quantum-mechanical position operator in extended systems. *Phys. Rev. Lett.*, 80:1800–1803, Mar 1998.

[46] Hwanmun Kim, Guanyu Zhu, James V Porto, and Mohammad Hafezi. Optical lattice with torus topology. *Physical review letters*, 121(13):133002, 2018.

[47] Mateusz Lacki, Hannes Pichler, Antoine Sterdyniak, Andreas Lyras, Vassilis E Lembessis, Omar Al-Dossary, Jan Carl Budich, and Peter Zoller. Quantum hall physics with cold atoms in cylindrical optical lattices. *Physical Review A*, 93(1):013604, 2016.

[48] Alexei Kitaev. Anyons in an exactly solved model and beyond. *Ann. Phys.*, 321(1):2 – 111, 2006.

[49] Parsa Hassan Bonderson. *Non-Abelian Anyons and Interferometry*. PhD thesis, California Institute of Technology, 2007.

[50] Zhenghan Wang. *Topological Quantum Computation*. American Mathematical Society, 2008.

[51] Kyle Kawagoe and Michael Levin. Microscopic definitions of anyon data. *Physical Review B*, 101(11):115113, 2020.

[52] A.Yu. Kitaev. Fault-tolerant quantum computation by anyons. *Annals Phys.*, 303:2–30, 2003.

[53] Michael A Levin and Xiao-Gang Wen. String-net condensation: A physical mechanism for topological phases. *Physical Review B*, 71(4):045110, 2005.

[54] Davide Gaiotto, Anton Kapustin, Nathan Seiberg, and Brian Willett. Generalized global symmetries. 2014.

[55] Jeongwan Haah. An invariant of topologically ordered states under local unitary transformations. *Communications in Mathematical Physics*, 342(3):771–801, 2016.

[56] Jon M Leinaas and Jan Myrheim. On the theory of identical particles. *Il Nuovo Cimento B (1971-1996)*, 37(1):1–23, 1977.

[57] Bertrand I Halperin. Statistics of quasiparticles and the hierarchy of fractional quantized Hall states. *Physical Review Letters*, 52(18):1583, 1984.

[58] R Willett, JP Eisenstein, HL Störmer, DC Tsui, AC Gossard, and JH English. Observation of an even-denominator quantum number in the fractional quantum Hall effect. *Physical review letters*, 59(15):1776, 1987.

[59] Gregory Moore and Nicholas Read. Nonabelions in the fractional quantum Hall effect. *Nuclear Physics B*, 360(2-3):362–396, 1991.

[60] Martin Greiter, Xiao-Gang Wen, and Frank Wilczek. Paired Hall state at half filling. *Physical review letters*, 66(24):3205, 1991.

[61] Chetan Nayak and Frank Wilczek. 2n-quasihole states realize 2n- 1-dimensional spinor braiding statistics in paired quantum Hall states. *Nuclear Physics B*, 479(3):529–553, 1996.

[62] Nicholas Read and Dmitry Green. Paired states of fermions in two dimensions with breaking of parity and time-reversal symmetries and the fractional quantum Hall effect. *Physical Review B*, 61(15):10267, 2000.

[63] Sankar Das Sarma, Michael Freedman, and Chetan Nayak. Majorana zero modes and topological quantum computation. *npj Quantum Information*, 1:15001, 2015.

[64] Abolhassan Vaezi. Superconducting analogue of the parafermion fractional quantum Hall states. *Physical Review X*, 4(3):031009, 2014.

[65] Chetan Nayak, Steven H. Simon, Ady Stern, Michael Freedman, and Sankar Das Sarma. Non-Abelian anyons and topological quantum computation. *Rev. Mod. Phys.*, 80:1083–1159, Sep 2008.

[66] Bertrand I Halperin. Theory of the quantized Hall conductance. *Helv. Phys. Acta*, 56:75–102, 1983.

[67] FDM Haldane and EH Rezayi. Spin-singlet wave function for the half-integral quantum Hall effect. *Physical review letters*, 60(10):956, 1988.

[68] Xiao-Gang Wen. Continuous topological phase transitions between clean quantum Hall states. *Physical review letters*, 84(17):3950, 2000.

[69] Maissam Barkeshli and Xiao-Gang Wen. Bilayer quantum Hall phase transitions and the orbifold non-Abelian fractional quantum Hall states. *Physical Review B*, 84(11):115121, 2011.

[70] W Zhu, Zhao Liu, FDM Haldane, and DN Sheng. Fractional quantum Hall bilayers at half filling: Tunneling-driven non-Abelian phase. *Physical Review B*, 94(24):245147, 2016.

[71] Maissam Barkeshli and Xiao-Gang Wen. Non-Abelian two-component fractional quantum Hall states. *Phys. Rev. B*, 82:233301, Dec 2010.

[72] Scott Geraedts, Michael P Zaletel, Zlatko Papić, and Roger SK Mong. Competing Abelian and non-Abelian topological orders in ν= 1/3+ 1/3 quantum Hall bilayers. *Physical Review B*, 91(20):205139, 2015.

[73] Abolhassan Vaezi and Maissam Barkeshli. Fibonacci anyons from Abelian bilayer quantum Hall states. *Physical review letters*, 113(23):236804, 2014.

[74] Zhao Liu, Abolhassan Vaezi, Kyungmin Lee, and Eun-Ah Kim. Non-Abelian phases in two-component ν= 2/3 fractional quantum Hall states: Emergence of Fibonacci anyons. *Physical Review B*, 92(8):081102, 2015.

[75] S. L. Sondhi, A. Karlhede, S. A. Kivelson, and E. H. Rezayi. Skyrmions and the crossover from the integer to fractional quantum Hall effect at small Zeeman energies. *Phys. Rev. B*, 47:16419–16426, Jun 1993.

[76] H. A. Fertig, L. Brey, R. Côté, and A. H. MacDonald. Charged spin-texture excitations and the Hartree-Fock approximation in the quantum Hall effect. *Phys. Rev. B*, 50:11018–11021, Oct 1994.

[77] HA Fertig, Luis Brey, R Côté, AH MacDonald, A Karlhede, and SL Sondhi. Hartree-Fock theory of Skyrmions in quantum Hall ferromagnets. *Physical Review B*, 55(16):10671, 1997.

[78] K. Moon, H. Mori, Kun Yang, S. M. Girvin, A. H. MacDonald, L. Zheng, D. Yoshioka, and Shou-Cheng Zhang. Spontaneous interlayer coherence in double-layer quantum Hall systems: Charged vortices and Kosterlitz-Thouless phase transitions. *Phys. Rev. B*, 51:5138–5170, Feb 1995.

[79] SE Barrett, G Dabbagh, LN Pfeiffer, KW West, and R Tycko. Optically pumped NMR evidence for finite-size skyrmions in GaAs quantum wells near Landau level filling ν= 1. *Physical review letters*, 74(25):5112, 1995.

[80] A Schmeller, JP Eisenstein, LN Pfeiffer, and KW West. Evidence for skyrmions and single spin flips in the integer quantized Hall effect. *Physical review letters*, 75(23):4290, 1995.

[81] EH Aifer, BB Goldberg, and DA Broido. Evidence of skyrmion excitations about ν= 1 in n-modulation-doped single quantum wells by interband optical transmission. *Physical review letters*, 76(4):680, 1996.

[82] Tobias Graß, Michael Gullans, Przemyslaw Bienias, Guanyu Zhu, Areg Ghazaryan, Pouyan Ghaemi, and Mohammad Hafezi. Optical control over bulk excitations in fractional quantum Hall systems. *Physical Review B*, 98(15):155124, 2018.

[83] Areg Ghazaryan, Tobias Graß, Michael J Gullans, Pouyan Ghaemi, and Mohammad Hafezi. Light-induced fractional quantum Hall phases in graphene. *Physical review letters*, 119(24):247403, 2017.

[84] Takashi Oka and Hideo Aoki. Photovoltaic Hall effect in graphene. *Phys. Rev. B*, 79:081406, Feb 2009.

[85] Jérôme Cayssol, Balázs Dóra, Ferenc Simon, and Roderich Moessner. Floquet topological insulators. *physica status solidi (RRL)–Rapid Research Letters*, 7(1-2):101–108, 2013.

[86] F Duncan M Haldane. Fractional quantization of the Hall effect: a hierarchy of incompressible quantum fluid states. *Physical Review Letters*, 51(7):605, 1983.

[87] Ian P McCulloch. Infinite size density matrix renormalization group, revisited. *arXiv preprint arXiv:0804.2509*, 2008.

[88] Michael P Zaletel, Roger SK Mong, and Frank Pollmann. Topological characterization of fractional quantum Hall ground states from microscopic Hamiltonians. *Physical review letters*, 110(23):236801, 2013.

[89] Michael P Zaletel, Roger SK Mong, Frank Pollmann, and Edward H Rezayi. Infinite density matrix renormalization group for multicomponent quantum Hall systems. *Physical Review B*, 91(4):045115, 2015.

[90] M. O. Goerbig. Electronic properties of graphene in a strong magnetic field. *Rev. Mod. Phys.*, 83:1193–1243, Nov 2011.

[91] Michael J. Gullans, Jacob M. Taylor, Ata ç Imamoğlu, Pouyan Ghaemi, and Mohammad Hafezi. High-order multipole radiation from quantum Hall states in Dirac materials. *Phys. Rev. B*, 95:235439, Jun 2017.

[92] Hui Li and F. D. M. Haldane. Entanglement Spectrum as a Generalization of Entanglement Entropy: Identification of Topological Order in Non-Abelian Fractional Quantum Hall Effect States. *Phys. Rev. Lett.*, 101:010504, Jul 2008.

[93] Hiroyuki Fujita and Masahiro Sato. Encoding orbital angular momentum of light in magnets. *Phys. Rev. B*, 96:060407, Aug 2017.

[94] A. Elben, B. Vermersch, C. F. Roos, and P. Zoller. Statistical correlations between locally randomized measurements: A toolbox for probing entanglement in many-body quantum states. *Phys. Rev. A*, 99:052323, May 2019.

[95] B. Vermersch, A. Elben, M. Dalmonte, J. I. Cirac, and P. Zoller. Unitary n-designs via random quenches in atomic hubbard and spin models: Application to the measurement of rényi entropies. *Phys. Rev. A*, 97:023604, Feb 2018.

[96] Hsin-Yuan Huang, Richard Kueng, and John Preskill. Predicting many properties of a quantum system from very few measurements. *arXiv preprint arXiv:2002.08953*, 2020.

[97] Edward Witten. Quantum field theory and the jones polynomial. *Communications in Mathematical Physics*, 121(3):351–399, Sep 1989.

[98] John Preskill. Quantum computing in the nisq era and beyond. *Quantum*, 2:79, 2018.

[99] A. J. Daley, H. Pichler, J. Schachenmayer, and P. Zoller. Measuring entanglement growth in quench dynamics of bosons in an optical lattice. *Phys. Rev. Lett.*, 109:020505, Jul 2012.

[100] Dmitry A. Abanin and Eugene Demler. Measuring entanglement entropy of a generic many-body system with a quantum switch. *Phys. Rev. Lett.*, 109:020504, Jul 2012.

[101] Rajibul Islam, Ruichao Ma, Philipp M Preiss, M Eric Tai, Alexander Lukin, Matthew Rispoli, and Markus Greiner. Measuring entanglement entropy in a quantum many-body system. *Nature*, 528(7580):77–83, 2015.

[102] Adam M Kaufman, M Eric Tai, Alexander Lukin, Matthew Rispoli, Robert Schittko, Philipp M Preiss, and Markus Greiner. Quantum thermalization through entanglement in an isolated many-body system. *Science*, 353(6301):794–800, 2016.

[103] Benoît Collins and Piotr Śniady. Integration with respect to the haar measure on unitary, orthogonal and symplectic group. *Communications in Mathematical Physics*, 264(3):773–795, 2006.

[104] Zbigniew Puchała and Jarosław Adam Miszczak. Symbolic integration with respect to the haar measure on the unitary group. *arXiv preprint arXiv:1109.4244*, 2011.

[105] Mohammad Hafezi, Anders Søndberg Sørensen, Eugene Demler, and Mikhail D Lukin. Fractional quantum hall effect in optical lattices. *Physical Review A*, 76(2):023613, 2007.

[106] Johannes Motruk and Frank Pollmann. Phase transitions and adiabatic preparation of a fractional chern insulator in a boson cold-atom model. *Physical Review B*, 96(16):165107, 2017.

[107] Yin-Chen He, Fabian Grusdt, Adam Kaufman, Markus Greiner, and Ashvin Vishwanath. Realizing and adiabatically preparing bosonic integer and fractional quantum hall states in optical lattices. *Phys. Rev. B*, 96:201103, Nov 2017.

[108] Eliot Kapit, Mohammad Hafezi, and Steven H. Simon. Induced self-stabilization in fractional quantum hall states of light. *Phys. Rev. X*, 4:031039, Sep 2014.

[109] Frank Arute, Kunal Arya, Ryan Babbush, Dave Bacon, Joseph C Bardin, Rami Barends, Rupak Biswas, Sergio Boixo, Fernando GSL Brandao, David A Buell, et al. Quantum supremacy using a programmable superconducting processor. *Nature*, 574(7779):505–510, 2019.

[110] B. Vermersch, A. Elben, L. M. Sieberer, N. Y. Yao, and P. Zoller. Probing scrambling using statistical correlations between randomized measurements. *Phys. Rev. X*, 9:021061, Jun 2019.

[111] Guanyu Zhu, Mohammad Hafezi, and Maissam Barkeshli. Quantum Origami: Transversal Gates for Quantum Computation and Measurement of Topological Order. *arXiv:1711.05752*, November 2017.

[112] José Garre-Rubio and Sofyan Iblisdir. Local order parameters for symmetry fractionalization. *New Journal of Physics*, 21(11):113016, 2019.

[113] Xiao-Gang Wen. *Quantum Field Theory of Many-Body Systems*. Oxford Univ. Press, Oxford, 2004.

[114] Chetan Nayak, Steven H. Simon, Ady Stern, Michael Freedman, and Sankar Das Sarma. Non-abelian anyons and topological quantum computation. *Rev. Mod. Phys.*, 80:1083, 2008.

[115] T. Senthil. Symmetry-protected topological phases of quantum matter. *Annual Review of Condensed Matter Physics*, 6:299–324, 2015.

[116] Bei Zeng, Xie Chen, Duan-Lu Zhou, Xiao-Gang Wen, et al. *Quantum information meets quantum matter*. Springer, 2019.

[117] David Aasen, Parsa Bonderson, and Christina Knapp. Characterization and classification of fermionic symmetry enriched topological phases. *arXiv preprint arXiv:2109.10911*, 2021.

[118] K. J. Satzinger et al. Realizing topologically ordered states on a quantum processor. *Science*, 374(6572):1237–1241, 2021.

[119] G. Semeghini, H. Levine, A. Keesling, S. Ebadi, T. T. Wang, D. Bluvstein, R. Verresen, H. Pichler, M. Kalinowski, R. Samajdar, A. Omran, S. Sachdev, A. Vishwanath, M. Greiner, V. Vuletic, and M. D. Lukin. Probing topological spin liquids on a programmable quantum simulator. *Science*, 374(6572):1242–1247, 2021.

[120] Dolev Bluvstein, Harry Levine, Giulia Semeghini, Tout T Wang, Sepehr Ebadi, Marcin Kalinowski, Alexander Keesling, Nishad Maskara, Hannes Pichler, Markus Greiner, et al. A quantum processor based on coherent transport of entangled atom arrays. *arXiv preprint arXiv:2112.03923*, 2021.

[121] Ruihua Fan, Rahul Sahay, and Ashvin Vishwanath. Extracting the quantum hall conductance from a single bulk wavefunction. *arXiv preprint arXiv:2208.11710*, 2022.

[122] Jacob C. Bridgeman, Steven T. Flammia, and David Poulin. Detecting topological order with ribbon operators. *Physical Review B*, 94(20), Nov 2016.

[123] Thorsten B Wahl and Benjamin Béri. Local integrals of motion for topologically ordered many-body localized systems. *Physical Review Research*, 2(3):033099, 2020.

[124] Frank Verstraete, Valentin Murg, and J Ignacio Cirac. Matrix product states, projected entangled pair states, and variational renormalization group methods for quantum spin systems. *Advances in physics*, 57(2):143–224, 2008.

[125] Nick Bultinck, Michael Mariën, Dominic J Williamson, Mehmet B Şahinoğlu, Jutho Haegeman, and Frank Verstraete. Anyons and matrix product operator algebras. *Annals of physics*, 378:183–233, 2017.

[126] Diederik P Kingma and Jimmy Ba. Adam: A method for stochastic optimization. *arXiv preprint arXiv:1412.6980*, 2014.

[127] Román Orús and Guifré Vidal. Simulation of two-dimensional quantum systems on an infinite lattice revisited: Corner transfer matrix for tensor contraction. *Physical Review B*, 80(9):094403, 2009.

[128] Hai-Jun Liao, Jin-Guo Liu, Lei Wang, and Tao Xiang. Differentiable programming tensor networks. *Physical Review X*, 9(3):031041, 2019.

[129] SPG Crone and P Corboz. Detecting a z 2 topologically ordered phase from unbiased infinite projected entangled-pair state simulations. *Physical Review B*, 101(11):115143, 2020.

[130] Fengcheng Wu, Youjin Deng, and Nikolay Prokof'ev. Phase diagram of the toric code model in a parallel magnetic field. *Physical Review B*, 85(19):195104, 2012.

[131] Julien Vidal, Sébastien Dusuel, and Kai Phillip Schmidt. Low-energy effective theory of the toric code model in a parallel magnetic field. *Physical Review B*, 79(3):033109, 2009.

[132] IS Tupitsyn, Alexei Kitaev, NV Prokof Ev, and PCE Stamp. Topological multicritical point in the phase diagram of the toric code model and three-dimensional lattice gauge higgs model. *Physical Review B*, 82(8):085114, 2010.

[133] Gábor B Halász and Alioscia Hamma. Probing topological order with rényi entropy. *Physical Review A*, 86(6):062330, 2012.

[134] Anna Ritz-Zwilling, Jean-Noël Fuchs, and Julien Vidal. Wegner-wilson loops in string nets. *Physical Review B*, 103(7):075128, 2021.

[135] Philippe Corboz, Karlo Penc, Frédéric Mila, and Andreas M Läuchli. Simplex solids in su (n) heisenberg models on the kagome and checkerboard lattices. *Physical Review B*, 86(4):041106, 2012.

[136] Julien Dorier, Federico Becca, and Frédéric Mila. Quantum compass model on the square lattice. *Physical Review B*, 72(2):024448, 2005.

[137] Dave Bacon. Operator quantum error-correcting subsystems for self-correcting quantum memories. *Physical Review A*, 73(1):012340, 2006.

[138] Claudio Castelnovo and Claudio Chamon. Quantum topological phase transition at the microscopic level. *Physical Review B*, 77(5):054433, 2008.